Cell

DNA-guided transcription factor cooperativity shapes face and limb mesenchyme

Graphical abstract

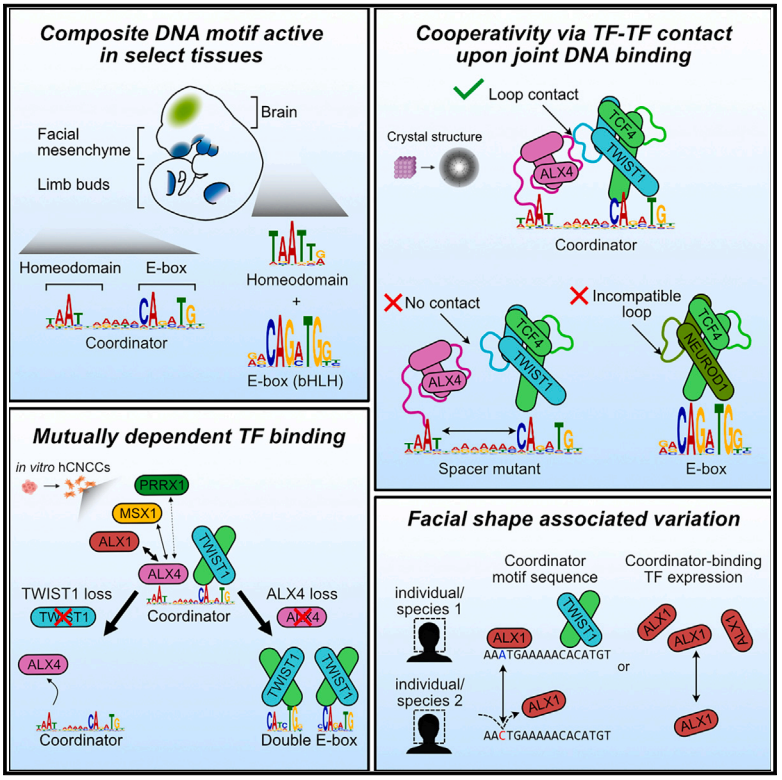

Highlights

- Mutually dependent binding of TWIST1 and homeodomain TFs in embryonic mesenchyme
- TF co-binding drives enhancer accessibility and shared transcriptional regulation
- Weak TF-TF contacts guided by DNA mediate the selectivity of cooperating partners
- TWIST1, partners, and bound targets enriched for face-shape-associated SNPs

Authors

Seungsoo Kim, Ekaterina Morgunova, Sahin Naqvi, ..., Peter Claes, Jussi Taipale, Joanna Wysocka

Correspondence

wysocka@stanford.edu

In brief

Epigenomic, biochemical, structural, and human phenotypic analyses of transcription factors that regulate a composite DNA motif in the embryonic face and limb mesenchyme reveal how DNA-guided cooperative binding gives rise to specificity among members of large TF families. This cooperativity promotes the integration of cellular and positional identity programs and contributes to the evolution and individual variation of human facial shape.

Kim et al., 2024, Cell *187*, 692–711
February 1, 2024
https://doi.org/10.1016/j.cell.2023.12.032

CellPress

CellPress
OPEN ACCESS

Cell

Article

DNA-guided transcription factor cooperativity shapes face and limb mesenchyme

Seungsoo Kim,[1,2,3,4] Ekaterina Morgunova,[5,13] Sahin Naqvi,[1,2,3,6,13] Seppe Goovaerts,[7,8] Maram Bader,[1,2,3] Mervenaz Koska,[2] Alexander Popov,[9] Christy Luong,[1] Angela Pogson,[2] Tomek Swigut,[1,2,3,4] Peter Claes,[7,8,10] Jussi Taipale,[5,11,12] and Joanna Wysocka[1,2,3,4,14,*]

[1]Department of Chemical and Systems Biology, Stanford University, Stanford, CA 94305, USA
[2]Department of Developmental Biology, Stanford University, Stanford, CA 94305, USA
[3]Institute for Stem Cell Biology and Regenerative Medicine, Stanford University, Stanford, CA 94305, USA
[4]Howard Hughes Medical Institute, Stanford, CA 94305, USA
[5]Department of Medical Biochemistry and Biophysics, Karolinska Institutet, Solna, Sweden
[6]Department of Genetics, Stanford University, Stanford, CA 94305, USA
[7]Medical Imaging Research Center, UZ Leuven, Leuven, Belgium
[8]Department of Human Genetics, KU Leuven, Leuven, Belgium
[9]European Synchrotron Radiation Facility, Grenoble, France
[10]Department of Electrical Engineering, ESAT/PSI, KU Leuven, Leuven, Belgium
[11]Department of Biochemistry, University of Cambridge, Cambridge, UK
[12]Applied Tumor Genomics Program, University of Helsinki, Helsinki, Finland
[13]These authors contributed equally
[14]Lead contact
*Correspondence: wysocka@stanford.edu
https://doi.org/10.1016/j.cell.2023.12.032

SUMMARY

Transcription factors (TFs) can define distinct cellular identities despite nearly identical DNA-binding specificities. One mechanism for achieving regulatory specificity is DNA-guided TF cooperativity. Although *in vitro* studies suggest that it may be common, examples of such cooperativity remain scarce in cellular contexts. Here, we demonstrate how "Coordinator," a long DNA motif composed of common motifs bound by many basic helix-loop-helix (bHLH) and homeodomain (HD) TFs, uniquely defines the regulatory regions of embryonic face and limb mesenchyme. Coordinator guides cooperative and selective binding between the bHLH family mesenchymal regulator TWIST1 and a collective of HD factors associated with regional identities in the face and limb. TWIST1 is required for HD binding and open chromatin at Coordinator sites, whereas HD factors stabilize TWIST1 occupancy at Coordinator and titrate it away from HD-independent sites. This cooperativity results in the shared regulation of genes involved in cell-type and positional identities and ultimately shapes facial morphology and evolution.

INTRODUCTION

Sequence-specific transcription factors (TFs) play key roles in controlling gene expression. TFs bind DNA sequence motifs and recruit cofactors to modulate transcription.[1,2] However, many TFs fall into large families with highly conserved DNA-binding domains that often bind very similar DNA motifs.[2,3] Among the largest TF families in humans are homeodomain (HD, >200 TFs) and basic helix-loop-helix (bHLH, >100 TFs) proteins, well-known for their roles in driving diverse positional identities (e.g., HOX genes[4]) and cell-type identities[5] (e.g., MyoD1 and NeuroD1), respectively. However, most bHLH factors recognize a subset of CANNTG sequences collectively called the "E-box,"[6] whereas the motif TAATT[A/G] is bound by roughly a third of all HD TFs in humans.[7,8]

Cooperative TF binding is a mechanism for achieving DNA-binding specificity among TFs of large families and for integrating multiple biological inputs at *cis*-regulatory elements. Diverse mechanisms underlying TF cooperativity have been described,[9] but "DNA-mediated" or "DNA-guided" cooperativity is less well understood. Certain TFs can cooperatively bind juxtaposed DNA sites arranged in specific orientations and distances without forming stable, direct protein-protein interactions in solution. However, direct contacts between cooperating TFs are favored upon binding at composite DNA sites, stabilizing the occupancy of both TFs. *In vitro* analysis of TF pairs using consecutive affinity-purification systematic evolution of ligands by exponential enrichment (CAP-SELEX) revealed that DNA-guided cooperativity may be common.[10] However, most cellular studies of this mechanism and its biological function have been limited to few

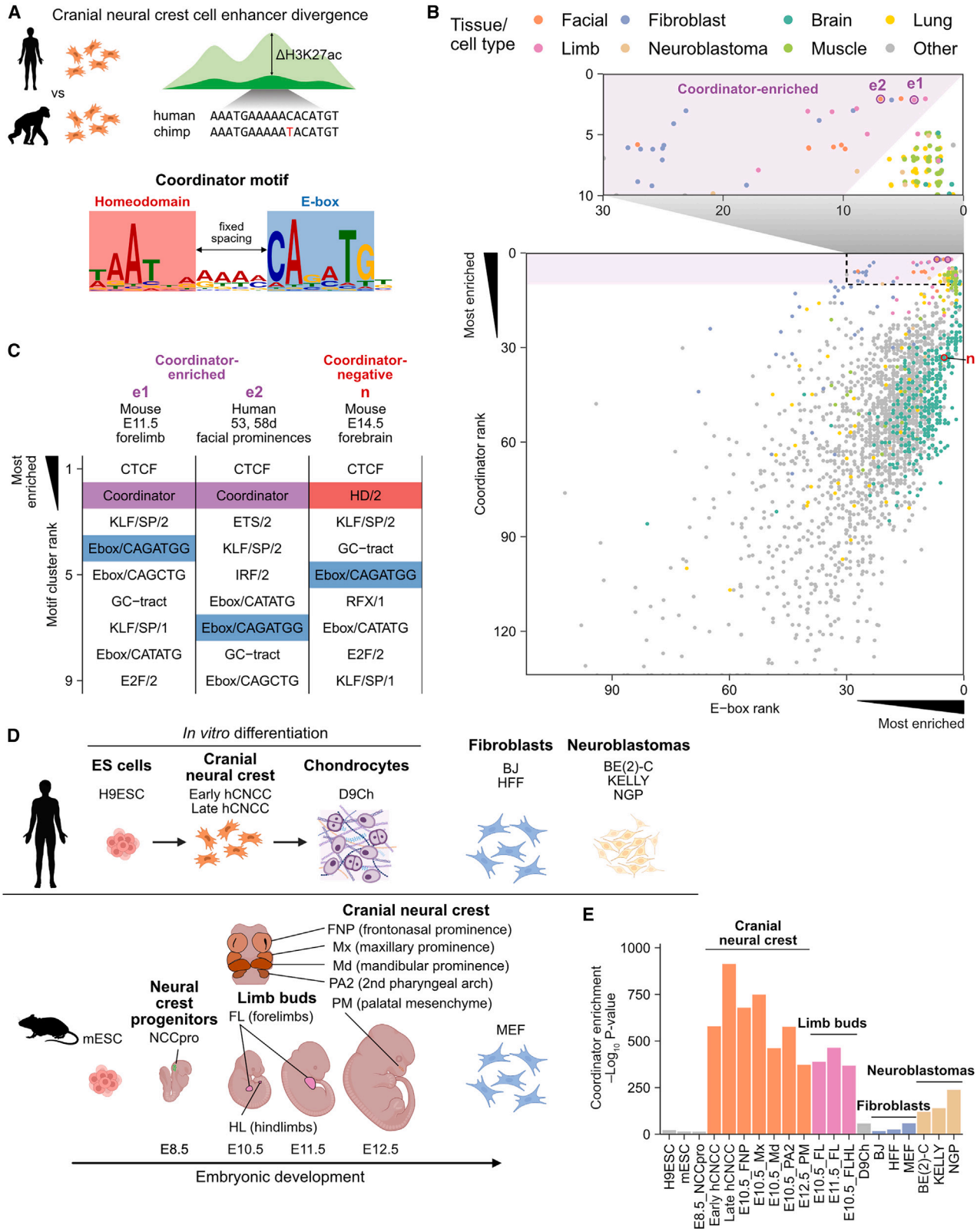

(legend on next page)

well-understood examples,[11–13] such as the pluripotency factors OCT4 and SOX2, which bind a composite motif combining their individual motifs[10] to facilitate chromatin opening.[14,15] In other cases, composite motifs have been observed in DNA sequence analyses of enhancers,[16–18] but their mechanisms of cooperativity and selectivity remain largely unexplored.

We previously serendipitously discovered a 17-bp DNA sequence motif with evidence of endogenous cellular function, which we termed Coordinator.[19] By comparing enhancer landscapes in human and chimpanzee facial progenitor cells called cranial neural crest cells (CNCCs) and analyzing the underlying DNA sequence changes, we uncovered motifs whose gains and losses correlated with changes in enhancer activity (Figure 1A). The Coordinator motif, discovered through *de novo* sequence analysis, was more predictive of species bias in enhancer activity than any known motif.[19] We, therefore, hypothesized that the *trans*-regulatory factor(s) that recognize the motif play an outsized role in coordinating enhancer activity in CNCCs and hence named the motif Coordinator. Although the motif was not annotated to a regulatory factor, it did not escape our attention that Coordinator contains the TAATT[A/G] motif bound by many HD factors and a version of the CANNTG E-box motif bound by most bHLH factors, separated by a fixed spacing (Figure 1A). Given the large number of bHLH and HD factors in humans,[2] the Coordinator motif represents an opportunity to gain insights into the mechanisms of specificity and functional implications of TF co-binding in a biologically relevant context. Thus, we sought to systematically identify TFs that bind the Coordinator motif, determine their molecular functions in an endogenous cellular context, and dissect the mechanisms underlying their cooperativity and selectivity.

RESULTS

The Coordinator motif is active specifically in embryonic face and limb mesenchyme

We wondered whether any cell types other than CNCCs also exhibit enrichment for the Coordinator motif in their active *cis*-regulatory regions. We defined a signature of Coordinator activity, based on the observation that in human CNCCs (hCNCCs), the Coordinator motif is most enriched in the top ~10,000 promoter-distal open chromatin peaks, as defined by the assay for transposase-accessible chromatin with sequencing (ATAC-seq) (Figure S1A). We searched for the enrichment of known motifs in each of the 549 ATAC-seq and 1,781 DNase-seq datasets from humans and mice in the Encyclopedia of DNA Elements (ENCODE),[20] collapsing similar motifs into motif clusters (STAR Methods). Finally, we identified samples with the following: (1) Coordinator among the top 10 motif clusters and (2) Coordinator ranked higher than either constituent motif cluster, E-box/CAGATGG or HD/2 (Figures 1B and 1C). An analogous approach recapitulates the specificity of the OCT:SOX motif active in pluripotent stem cells (Figure S1B).

As expected, embryonic facial prominences, largely composed of CNCCs, exhibit Coordinator motif activity (Figures 1B and 1C). However, many developing limb samples and a smaller subset of fibroblast and neuroblastoma samples also meet our definition of Coordinator activity. Notably, neuroblastoma is a cancer originating from neural-crest-derived lineages,[21] whereas fibroblasts are mesenchymal cells of either mesodermal or neural crest origin.[22] Importantly, other samples showing strong E-box and HD motif enrichment, such as those from the developing brain, lack Coordinator enrichment (Figure S1C). To corroborate this finding, we gathered additional published human and mouse ATAC-seq datasets from cell types related to those in which we initially detected Coordinator enrichment and relevant negative controls (Figure 1D).[23–34] *In-vitro*-derived mesenchymal hCNCCs and mouse embryonic facial prominences of CNCC origin have the strongest Coordinator motif enrichment, followed closely by limb bud samples, with much lower enrichment in neuroblastomas and fibroblasts (Figure 1E). Thus, the Coordinator motif is selectively enriched in the accessible *cis*-regulatory regions of the developing face and limb mesenchyme.

TWIST1 binds Coordinator across tissues with diverse HD TF expression

To systematically nominate candidate Coordinator-binding TFs, we searched for TFs with the following: (1) binding motifs consistent with the constituent E-box or HD halves of Coordinator and (2) high expression levels specifically in cell types with Coordinator enrichment in open chromatin. First, we aligned known TF motifs (derived from either chromatin immunoprecipitation sequencing [ChIP-seq] data or *in vitro* specificity measurements using SELEX or protein binding microarrays [PBMs]) against each half of the Coordinator motif. Of 54 TFs with motifs aligned to the E-box (Figures 2A and S2A), TWIST1 is the only TF with a motif spanning both the E-box and the HD motif. However, this motif is derived from ChIP-seq in neuroblastoma cells,[34] and as a bHLH factor, it directly binds only the E-box. In fact, previously published ChIP-seq for TWIST1 overexpressed in human mammary epithelial cells revealed binding to single or double E-box motifs.[35] Next, we examined the RNA levels of each candidate TF and their correlation with Coordinator motif enrichment across cell types. TWIST1 had the highest correlation ($r = 0.934$; Figures S2B and S2C). Indeed, we previously detected Coordinator motif enrichment at TWIST1 ChIP-seq peaks from hCNCCs.[23] To confirm that TWIST1 binds Coordinator *in vivo*,

Figure 1. The Coordinator motif is active specifically in embryonic face and limb mesenchyme

(A) Schematic of the Coordinator motif and its discovery.

(B) Rankings of Coordinator and its constituent E-box/CAGATGG motif in enrichment in the top 10,000 distal accessible regions in ENCODE. e1, e2, and n indicate examples detailed in (C). Points jittered to avoid overplotting.

(C) Top motif clusters for examples of Coordinator-enriched and Coordinator-negative samples, with relevant motifs highlighted.

(D) Schematic of cell types and tissues in (E).

(E) Coordinator motif enrichment across additional ATAC-seq datasets.

See also Figure S1.

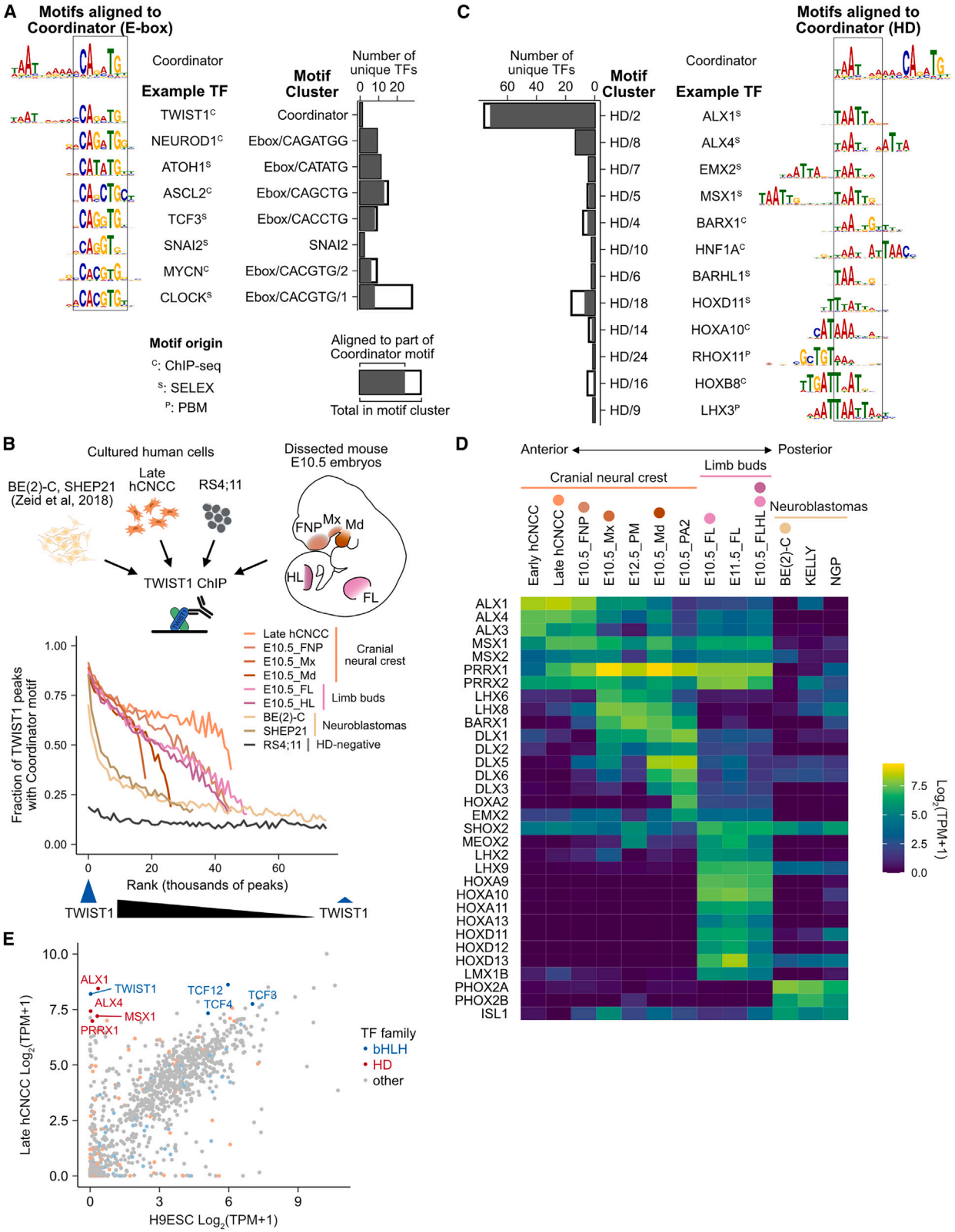

(legend on next page)

we performed Twist1 ChIP-seq in dissected E10.5 mouse embryos (Figure 2B), separately testing the frontonasal prominences (FNP), maxillary prominences (Mx), mandibular prominences (Md), forelimbs (FL), and hindlimbs (HL). We compared Twist1 binding specificities across these mouse tissues along with hCNCCs and previously published data from the neuroblastoma cell lines BE(2)-C and SHEP21.[34] Across these cellular contexts, the strongest TWIST1 peaks mostly contained the Coordinator motif, but weaker peaks were progressively less likely to do so. However, compared with hCNCCs, facial prominences, and limb buds, which sustained high Coordinator motif frequencies (>50%) for the top 20,000 peaks, neuroblastomas had such motif frequencies only in the top few thousand peaks (despite a greater total number of peaks). This rapid falloff is consistent with the weaker Coordinator enrichment in neuroblastoma open chromatin (Figure 1E).

Next, we focused on candidate factors binding the HD portion of Coordinator. Of 129 TFs with motifs aligned to the HD half of Coordinator, 32 are expressed moderately or highly in at least one cell type with Coordinator enrichment (Figures 2C, 2D, and S2D). However, no candidate was expressed in all Coordinator-positive cell types and could explain the quantitative variation in Coordinator activity. Instead, every cell type expresses multiple HD TFs robustly, with groups of HDs showing overlapping expression in distinct regions of the developing face and limbs, consistent with their previously described association with specific positional identities.[36–38]

To test whether these HDs collectively enable TWIST1 binding to Coordinator, we searched the Cancer Cell Line Encyclopedia[39] (CCLE) for cell lines with high RNA levels of TWIST1 but minimal levels of candidate Coordinator-binding HDs (Figure S2E). One of the best matches was RS4;11, an acute lymphoblastic leukemia cell line with a t(4;11) translocation. We performed TWIST1 ChIP-seq in RS4;11 cells and found that TWIST1 predominantly binds the single and double E-box motifs (Figure S2F), as in human mammary epithelial cells,[35] rather than Coordinator (Figure 2B). These results suggest that TWIST1 binds Coordinator only in cell types with HD proteins co-expressed.

Multiple HDs co-bind Coordinator motif with TWIST1

To study the mechanisms and functional role of TWIST1 cooperation with HD TFs at Coordinator, we turned to our *in vitro* model of human embryonic stem cell (hESC) differentiation to hCNCCs.[19,23,40,41] TWIST1 is the only bHLH TF selectively expressed in hCNCCs compared with hESCs, whereas the E-proteins TCF3, TCF4, and TCF12, known to heterodimerize with TWIST1,[35,42] are expressed in both cell types, consistent with their broad expression (Figure 2E). Among HD TFs, ALX1, ALX4, MSX1, and PRRX1 are the most highly and selectively expressed in our hCNCCs, in concordance with their closest resemblance to the anterior facial region CNCCs.[24]

Accordingly, we created hESC lines with each TF endogenously and homozygously tagged with the dTAG-inducible $FKBP12^{F36V}$ degron,[43,44] a V5 epitope tag, and, in one case, also the fluorophore mNeonGreen,[45] which we could then differentiate to hCNCCs *in vitro*[46] (Figure 3A). This approach allows the acute or long-term depletion of each TF (Figure 3B) and—through the common V5 tag—comparative studies of TF levels and DNA binding. We tagged TWIST1, ALX1, MSX1, and PRRX1 and confirmed near-complete depletion upon adding $dTAG^{V}$-1 to the media (Figures 3B and S3A). Tagging did not significantly decrease baseline TF levels (Figure S3B). Based on previous studies indicating that ALX1 and ALX4 have overlapping functions,[37,47] we generated multiple independent clonal lines with nonsense mutations in *ALX4* on top of the $ALX1^{FV}$ tag, as we were unable to degron tag ALX4 (Figures 3C and S3C).

We performed ChIP-seq and cleavage under targets and release using nuclease (CUT&RUN) to assess the DNA-binding profiles of these tagged TFs, as well as ALX4, TCF3 (a heterodimerization partner of TWIST1), and the positive control AP-2α (a key neural crest TF encoded by *TFAP2A*[40]), using endogenous antibodies. We first used binding sites for TWIST1 and AP-2α as reference points, grouping distal regulatory regions into those bound by TWIST1 or AP-2α only or those co-bound by both (Figure 3D). As expected, the binding of the TWIST1 heterodimerization partner TCF3 is correlated with that of TWIST1. For all four tested HD TFs, DNA binding at TWIST1 sites clearly exceeds that at AP-2α-only sites despite comparable accessibility. However, the strength of ChIP signal is reproducibly distinct between the tagged HD TFs, with the strongest signal for ALX1. This ranking is discordant with that of TF protein levels, as ALX1 has the lowest relative abundance but strongest binding (Figure 3B). ALX4 shows similar binding patterns, although we could not directly compare its chromatin occupancy with that of other HDs.

As an orthogonal approach, we called peaks for each TF and searched for enriched motifs (Figure 3E). The top motif cluster for TWIST1, TCF3, and all tested HD TFs is Coordinator, confirming that these HD TFs predominantly bind DNA with TWIST1. Together, these data indicate that TWIST1 can bind Coordinator sites with multiple HD TFs, including ALX4, ALX1, MSX1, and PRRX1, albeit at varying occupancies.

TWIST1 facilitates HD TF binding, chromatin opening, and enhancer activity

To investigate the mechanism and function of TF cooperation at Coordinator, we studied how the depletion of

Figure 2. TWIST1 binds Coordinator across tissues with diverse homeodomain TF expression

(A) Motif clusters and example motifs aligned to the E-box within Coordinator; bar plots show the number of aligned and total motifs per cluster (STAR Methods). Motif origin: C, ChIP; P, PBM; and S, SELEX.

(B) TWIST1 ChIP-seq in human cell types and dissected mouse embryo tissues. TWIST1 peaks ranked from the strongest to weakest in bins of 1,000 peaks.

(C) As in (A), but for the homeodomain (HD) portion.

(D) HD TF expression across cell/tissue types with Coordinator enrichment. Colored circles correspond to the schematic and data in (C).

(E) TF RNA expression in human cranial neural crest cells (hCNCCs) and H9 embryonic stem cells (H9ESCs). TPM, transcripts per million.

See also Figure S2.

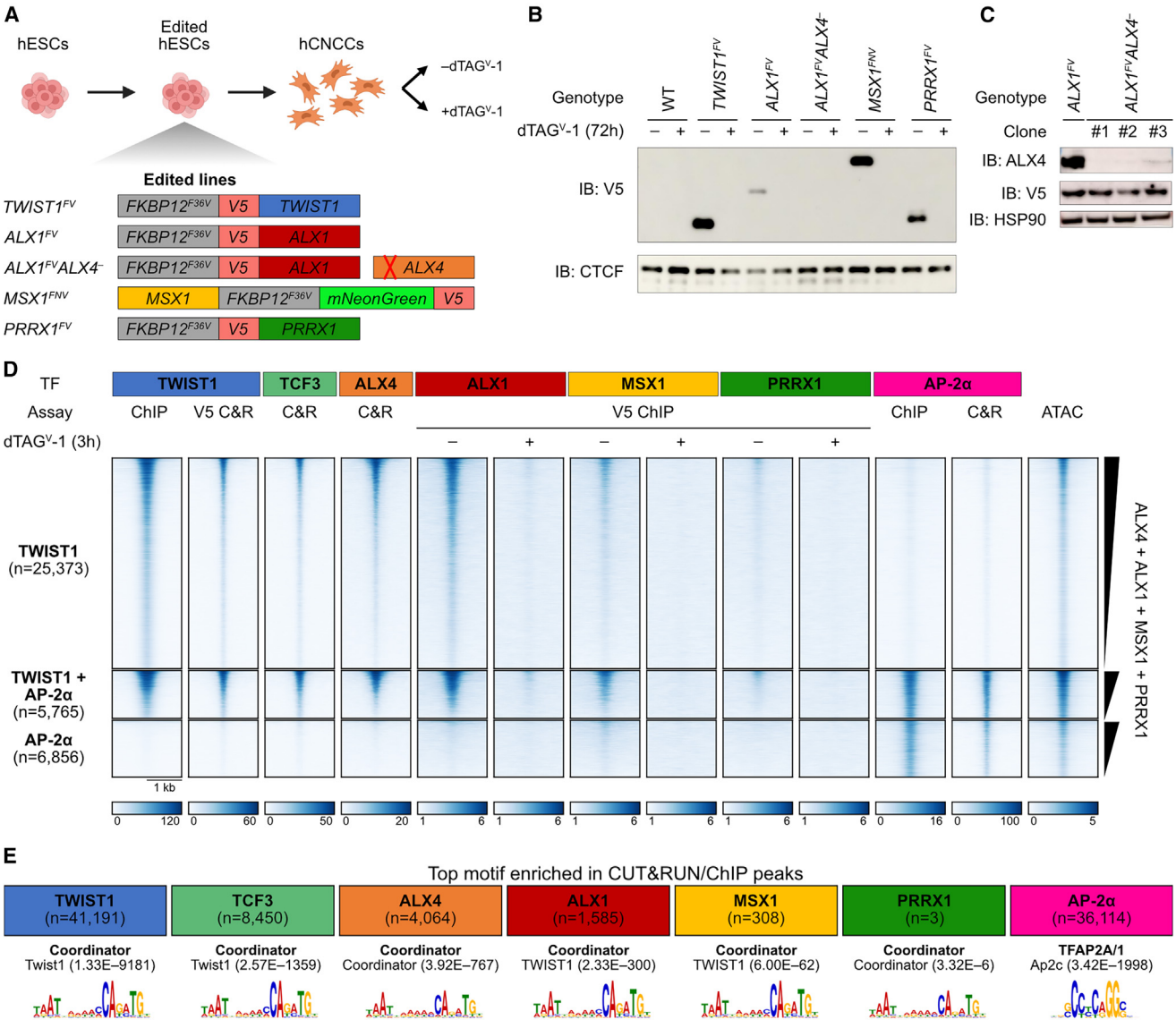

Figure 3. Multiple homeodomains co-bind Coordinator motif with TWIST1

(A) Schematic of endogenous TF tagging and knockout.

(B) Confirmation of TF tagging and depletion upon dTAG^V-1 addition by western blot. IB, immunoblot.

(C) Confirmation of ALX4 knockout in three independent clones by western blot.

(D) Heatmap of TF binding (ChIP and CUT&RUN) and chromatin accessibility (ATAC) at promoter-distal binding sites for TWIST1 and/or AP-2α. Units: reads per genome coverage, except for ATAC, which is in signal per million reads.

(E) The top enriched known motif for each TF, with p values.

See also Figure S3.

each Coordinator-binding TF impacts chromatin states and the binding of other TFs. We first focused on TWIST1, given its central role as the key bHLH-factor-binding Coordinator. We began with acute depletions ranging from 1 to 24 h in hCNCCs and performed ChIP-seq to measure TWIST1 binding, CUT&RUN for ALX4 binding, ATAC-seq to measure chromatin accessibility, and ChIP-seq for H3K27ac as a mark correlated with enhancer/promoter activity (Figure 4A).

TWIST1 depletion rapidly reshapes chromatin accessibility, with 36,290 regions losing accessibility and 17,054 regions gaining accessibility within 3 h (Figure S4A). The change in accessibility is mostly complete within 3 h (Figure S4B), so we combined the 3 and 24 h differentially accessible peaks to define a set of sites with the loss vs. gain of accessibility. Among candidate distal enhancers, 11,186 sites lose accessibility, 4,042 gain accessibility, and 4,732 do not significantly change (Figures 4B and 4C). Regions losing accessibility are

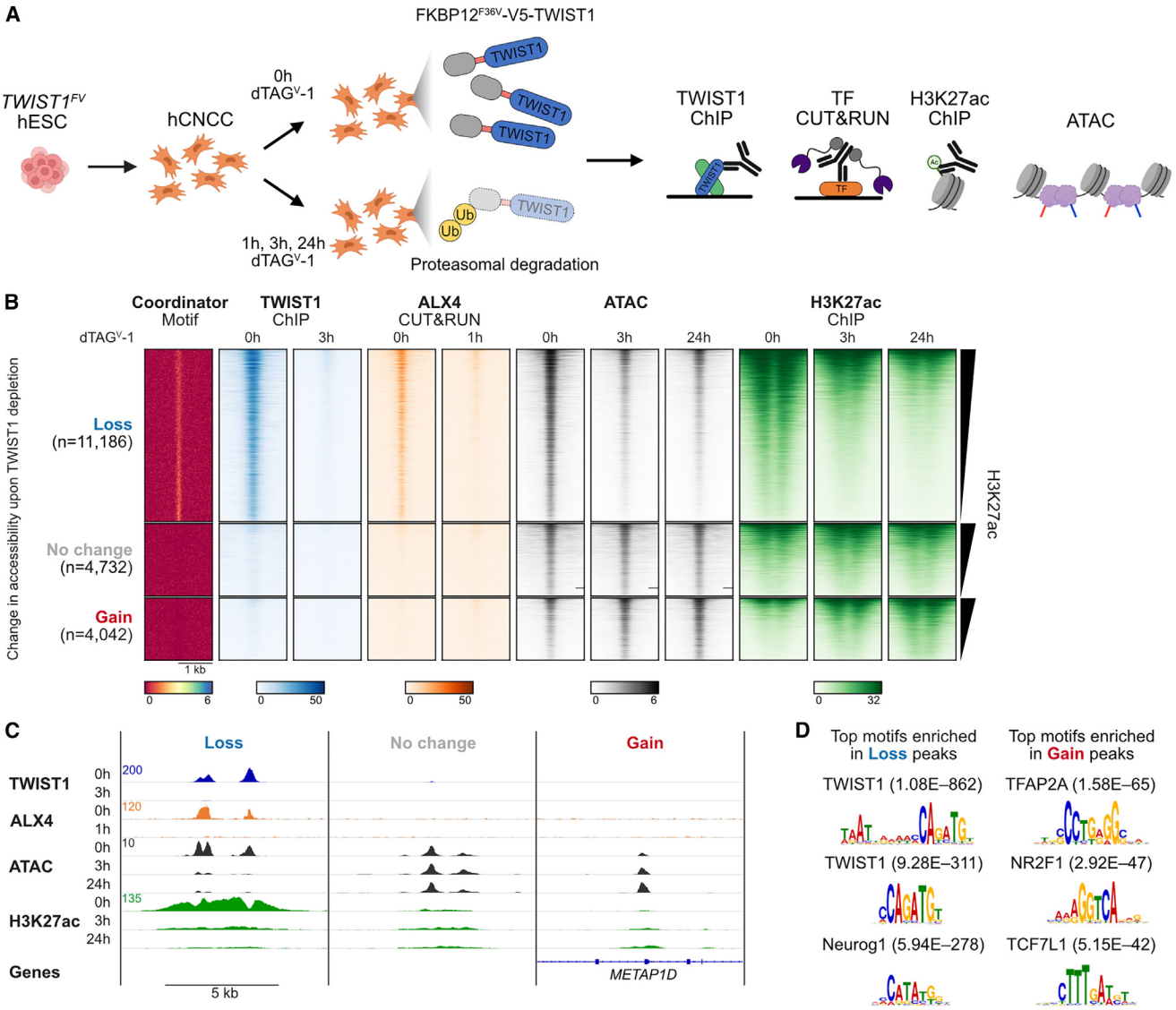

Figure 4. TWIST1 opens chromatin for homeodomain TFs and enhancer acetylation

(A) Schematic of acute depletion experiments.

(B) Heatmap of Coordinator motif enrichment, TF binding, chromatin accessibility (ATAC), and H3K27ac at distal enhancers grouped by their change in accessibility upon TWIST1 depletion. Units: reads per genome coverage, except for the Coordinator motif ($-\log_{10}$ p value) and ATAC (signal per million reads). One representative replicate of two independent differentiations.

(C) Example enhancers with the loss of, no change in, or the gain of accessibility upon TWIST1 depletion. Coordinates (hg38): loss, chr17:70,668,899–70,678,127; no change, chr11:44,958,683–44,968,011; and gain, chr2:172,058,768–172,068,096.

(D) Top enriched motif clusters in enhancers with the loss or gain of accessibility upon TWIST1 depletion compared with those with no change, with p values.

See also Figure S4.

highly enriched for the Coordinator motif and TWIST1 binding, whereas those gaining accessibility lack TWIST1 binding and are most enriched for AP-2α and NR2F1 motifs, suggesting that these effects are indirect (Figures 4B–4D). Changes in accessibility are correlated with changes in H3K27ac (Figures 4B and S4C, r = 0.834 for 3 h and 0.896 for 24 h). The loss of TWIST1 leads to the depletion of H3K27ac within hours, consistent with an activating role of TWIST1 (Figure S4D). Furthermore, TWIST1 depletion eliminates the enhancer reporter activity of a well-characterized *SOX9* enhancer dependent on the Coordinator motif[23] (Figure S4E). Importantly, TWIST1 depletion largely abrogates the DNA binding of ALX4 at Coordinator sites within 1 h (Figures 4B, 4C, and S4D). Therefore, both HD factor binding and open/active chromatin states of *cis*-regulatory elements depend on TWIST1, consistent with our original hypothesis that the *trans*-regulatory proteins recognizing Coordinator play a large role in enhancer activity in CNCCs.[19]

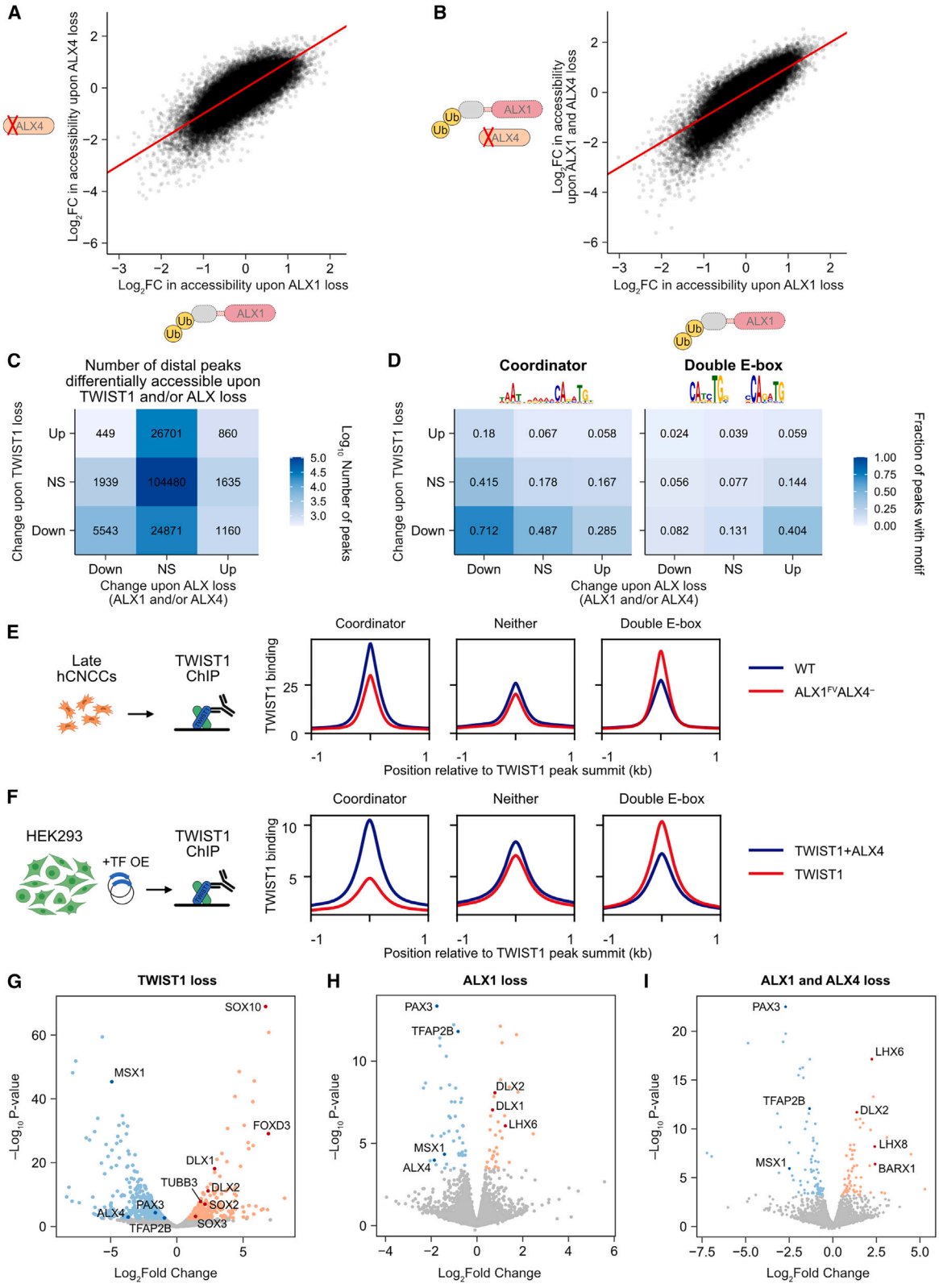

(legend on next page)

HD TFs cooperate with TWIST1 to open chromatin at Coordinator sites

We next asked how the depletion of HD TFs affects chromatin accessibility and TWIST1 binding at Coordinator. Since we only generated a constitutive knockout of ALX4, to obtain comparable data across all TF perturbations, we differentiated *ALX4*$^{-}$ hESCs along with ALX1, MSX1, PRRX1, and TWIST1 degron-tagged hESCs while treating cells with dTAG^{V}-1 from the beginning of differentiations to mimic a knockout. We harvested these cells at an early hCNCC stage to minimize indirect effects. Even in these long-term depletions, many of the observed effects are likely directly caused by HD dysfunction in mesenchymal CNCCs, as most of the aforementioned HD TFs are only expressed in CNCCs following their specification and delamination[37,48] (except MSX1, which is expressed in the neural plate border precursor to CNCCs[49]). Furthermore, accessibility effects of long-term TWIST1 depletion are well correlated with acute 24 h depletion ($r = 0.664$; Figure S5A).

Consistent with the range in the strength of DNA binding among HDs (Figure 3D), ALX1 depletion results in significant changes in accessibility at 6,195 peaks (false discovery rate [FDR] < 0.05), compared with 4,284 for ALX4; 1,410 for MSX1; and 0 for PRRX1, the weakest binder (Figure S5B). In general, HD TF depletions have much weaker effects than TWIST1 depletion, likely due to functional redundancy among them. Indeed, changes upon ALX1 and ALX4 losses are well correlated ($r = 0.651$) (Figure 5A). These are also correlated, albeit less well, with the effects of MSX1 loss ($r = 0.462$) (Figure S5C). Next, by comparing undepleted ALX1^{FV} samples (in which both ALX1 and ALX4 were present) with depleted ALX1^{FV} ALX4^{-} samples (in which both were lost), we inferred the effect of combined ALX1 and ALX4 loss on the ATAC-seq changes at the corresponding set of genomic targets. This comparison allowed the detection of differential accessibility at a greater number of peaks (8,577) (Figure 5B).

We next asked how similar the effects of ALX loss on chromatin accessibility are to those of TWIST1 loss on chromatin accessibility. Given the correlated effects of ALX1 and ALX4 losses (Figures 5A and 5B), we considered their combined effects, taking any ATAC-seq peak significantly affected by the loss of ALX1 or ALX4 or combined loss of both. As there are many more TWIST1-dependent peaks, most of these are not dependent on ALXs. However, of the distal peaks downregulated upon ALX loss, the vast majority (5,543/7,931; 70%) are concordant or also downregulated upon TWIST1 loss, whereas a few (449/7,931; 5.7%) are discordant or upregulated upon TWIST1 loss (Figure 5C). Peaks upregulated upon ALX loss lack this enrichment for concordance with TWIST1 effects, but these represent a minority (32%) of changes. The effects of MSX1 loss are also concordant with those of TWIST1 loss (Figure S5E). To find the DNA sequence features driving these concordant and discordant changes, we performed motif analyses on these classes of peaks. Coordinator is highly enriched in the TWIST1- and ALX-dependent peaks, underscoring that the main function of ALX1 and ALX4 in chromatin opening is indeed at Coordinator sites (Figure 5D). We also repeated the chromatin accessibility analysis upon the acute loss of each degron-tagged TF and observed minimal changes except for TWIST1 (Figure S5D).

Loss of HD TFs titrates TWIST1 away from Coordinator toward the canonical double E-box sites

In addition to Coordinator, other motifs provide insights into the mechanisms underlying TWIST1-HD cooperation (Figures 5D and S5F). The dominant feature of peaks that gain accessibility upon ALX loss but lose accessibility upon TWIST1 loss is the double E-box motif, which contains two E-box motifs at a 5 bp spacing. The double E-box motif has previously been proposed to bind two copies of TWIST1:TCF3 heterodimers,[35] and we found it highly enriched in the top TWIST1-binding sites in the HD-negative RS4;11 cells (Figures 5D and S2E). Thus, ALX loss appears to quantitatively redirect TWIST1 or its chromatin-opening capacity away from Coordinator sites and toward double E-box sites.

To substantiate this observation and determine whether the distribution of TWIST1 binding at Coordinator vs. double E-box sites is affected by ALX loss, we performed TWIST1 ChIP-seq in *ALX1*^{FV} *ALX4*$^{-}$ hCNCCs (without ALX1 depletion) and compared the binding with that of wild-type (WT) cells (Figure 5E). TWIST1-binding signal is reduced at sites with the Coordinator motif but increases at sites with the double E-box motif. These changes are quantitative, potentially due to the partially redundant functions of HD TFs. To confirm this finding in a cellular context without redundancy, we overexpressed TWIST1 with or without ALX4 in HEK293 cells (which lack an appreciable expression of TWIST1 or most HD TFs) and then performed TWIST1 ChIP-seq. As in hCNCCs but to a greater extent in this overexpression context, TWIST1 binding to Coordinator decreased in the absence of ALX4, whereas binding to the double E-box motif increased (Figure 5F).

Shared transcriptional functions of TWIST1 and ALX factors

To assess the transcriptional functions of TWIST1 and HD factors in our *in vitro* hCNCC differentiation model, we used

Figure 5. Homeodomain TFs stabilize TWIST1 binding at Coordinator sites.

(A) Correlation in $\log_2$ fold change (FC) in accessibility upon the loss of ALX1 (long-term dTAG^{V}-1 treatment) versus ALX4 (knockout). Red line, y = x.

(B) Change in accessibility upon the loss of both ALX1 and ALX4 vs. log sum of individual effects.

(C) Most chromatin accessibility effects of ALX loss (ALX1 and/or ALX4) are concordant with (but are a subset of) those of TWIST1 loss. NS, not significant.

(D) Top motif enrichments among peaks responsive to TWIST1 and ALX losses.

(E and F) TWIST1 binding by ChIP-seq quantitatively shifts from Coordinator to double E-box motif sites upon the loss of ALX4 (without ALX1 depletion) in hCNCCs (E) or the overexpression of TWIST1 alone rather than with ALX4 in HEK293 cells (F).

(G–I) Volcano plots of differential gene expression upon the loss of TWIST1 (G), ALX1 (H), or ALX1 and ALX4 (I). ALX4 is excluded in (I). Selected genes are highlighted in darker colors.

See also Figure S5.

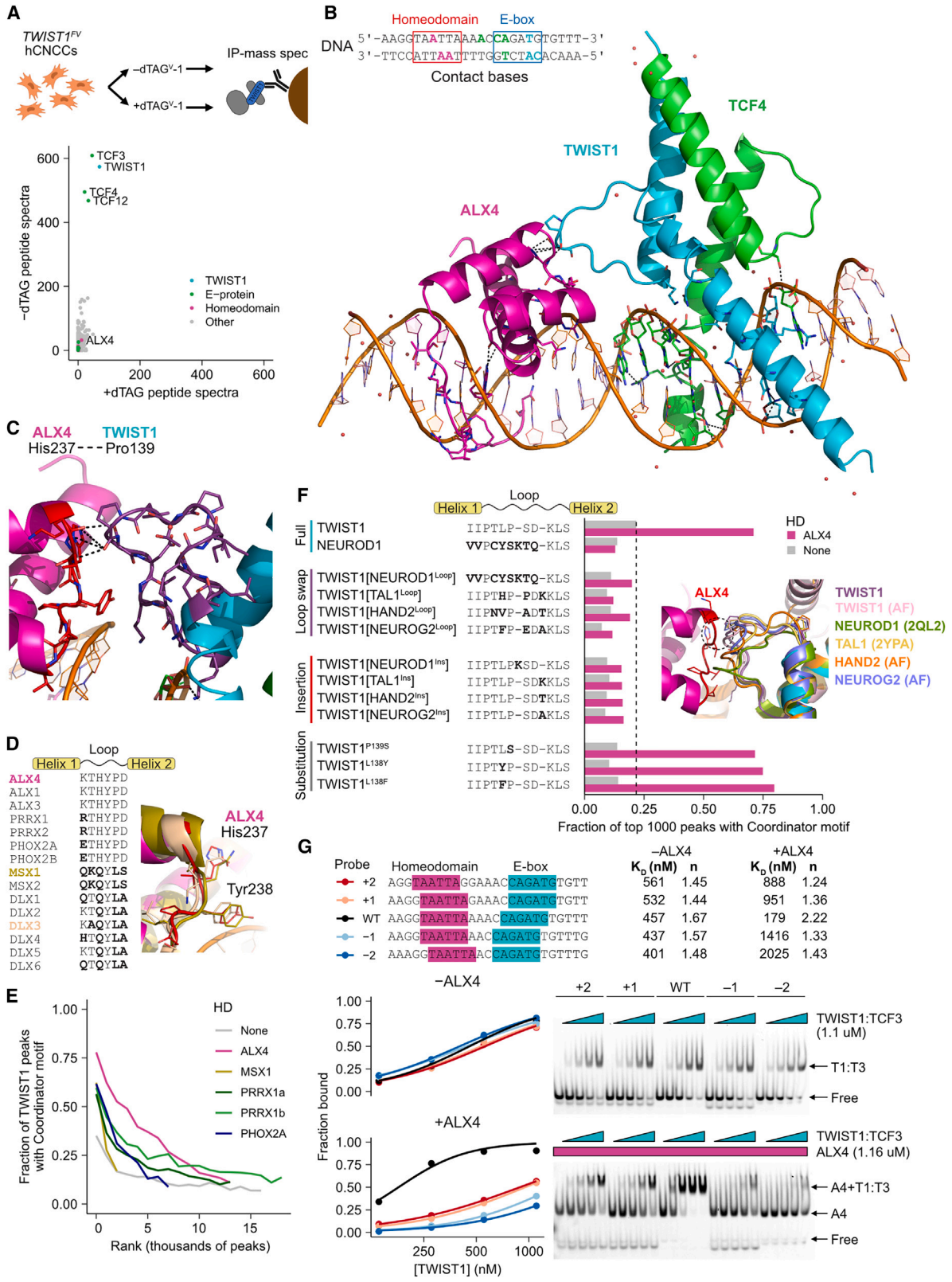

Probe	Homeodomain	E-box	−ALX4 K_D (nM)	−ALX4 n	+ALX4 K_D (nM)	+ALX4 n
+2	AGG	TAATTA	GGAAAC	CAGATG	TGTT	561	1.45	888	1.24
+1	AAG	TAATTA	GAAAC	CAGATG	TGTT	532	1.44	951	1.36
WT	AAG	TAATTA	AAAC	CAGATG	TGTTT	457	1.67	179	2.22
−1	AAG	TAATTA	AAC	CAGATG	TGTTTG	437	1.57	1416	1.33
−2	AAAG	TAATTA	AC	CAGATG	TGTTTG	401	1.48	2025	1.43

(legend on next page)

RNA sequencing (RNA-seq) to identify genes significantly affected by the perturbation of TWIST1, ALX1, or both ALX1/4 (Figures 5G–5I). Consistent with previous mouse studies,[50,51] the most significant effect of TWIST1 loss is an increase in the expression of *SOX10*, a marker of early neural crest and neuronal/glial derivatives (Figure 5G). This is accompanied by the gain of other early neural crest[52,53] (*FOXD3*), neural progenitor (*SOX2/3*), and neuronal (*TUBB3*) markers, suggesting a defect in mesenchymal specification. Meanwhile, the loss of ALXs (expressed primarily in the anterior CNCC) leads to the upregulation of TF genes normally expressed only in more posterior parts of the face (*DLX1*, *DLX2*, *LHX6*, *LHX8*, and *BARX1*) and downregulation of TF genes normally most abundant in the anterior regions of the face, such as *PAX3*, *TFAP2B*, and *ALX4* (the latter upon ALX1 depletion) (Figures 5H and 5I). This suggests that ALXs promote the expression of genes associated with this anterior identity, as seen in a recent Alx1-null mouse.[37]

Notably, there is substantial overlap between TWIST1- and ALX-responsive genes, with a subset of position-specific genes (*DLX1/2*, *PAX3*, and *TFAP2B*) regulated by TWIST1 and ALXs (Figures 5G–5I). Furthermore, *MSX1*, a gene encoding HD TF broadly expressed throughout the face and limb buds and associated with mesenchymal cell identity,[54] is downregulated upon the loss of ALXs and TWIST1. This overlap is representative of overall concordance between TWIST1 and ALX transcriptional changes: genes downregulated upon ALX loss are enriched for downregulation upon TWIST1 loss as well (Figure S5G). Note that MSX1 loss affects mesenchymal specification, with the upregulation of neural progenitor markers *SOX2* and *SOX3*, as seen with TWIST1 loss (Figure S5H), but generally has fewer effects than the loss of ALXs, so shared activation of *MSX1* cannot explain most of the overlap in ALX and TWIST1 functions. These results suggest that TWIST1 and HD TF co-binding at Coordinator sites drives shared transcriptional functions and may serve to integrate regulatory programs for lineage and regional identities during facial development.

The Coordinator motif guides contact and cooperativity between TWIST1 and HD TFs

We next investigated the biochemical and structural mechanisms underlying the cooperative co-binding of TWIST1 and HD factors at Coordinator sites. We first used immunoprecipitation-mass spectrometry (IP-MS) to identify proteins that interact with TWIST1 in hCNCCs, using a nuclear protein extraction protocol that minimizes the extraction of DNA (Figure 6A; Table S1). Consistent with published results, we found that TWIST1 forms stable heterodimers with its E-protein partners TCF3, TCF4, and TCF12.[35,42,55] However, TWIST1 lacks interactions with ALXs or other HD TFs, as confirmed by reciprocal IP-MS experiments pulling down the HD TFs (Table S1).

This suggested that cooperativity between TWIST1 and ALX proteins may be guided by the Coordinator motif DNA sequence. To explore this possibility, we solved an X-ray crystal structure of TWIST1, TCF4, and ALX4 DNA-binding domains co-bound to the consensus Coordinator motif at 2.9 Å resolution (Figure 6B). As expected, a TWIST1-TCF4 heterodimer binds the E-box and ALX4 binds the HD monomer motif within Coordinator. Within the bHLH dimer, TWIST1 binds the side of the E-box motif further from the HD motif, allowing its loop to contact ALX4 (Figure 6C). The contact primarily involves a hydrogen bond between the TWIST1 backbone at proline 139 and the ALX4 histidine 237 side chain, but other weaker hydrogen bonds (TWIST1 Ser140-ALX4 His237) and hydrophobic interactions (e.g., TWIST1 Lys142-ALX4 Tyr238) further stabilize the complex (Table S2). Our structure suggests that although interactions between TWIST1 and ALX4 are insufficient to form a stable complex in solution, these weak contacts are stabilized on DNA.

To validate the role of TWIST1-HD interactions in cooperativity, we explored the effects of amino acid sequence variation in both the bHLH and HD, using evolution as a guide. The amino acid residues, and more broadly the loops, involved in the TWIST1-HD contact are not invariant across paralogous TFs with highly similar DNA-binding motifs (Figures 6D and 6F). To assess whether these loops form distinct structures, we aligned our TWIST1-TCF4-ALX4-Coordinator structure to previously solved or AlphaFold-predicted (individual) HD and bHLH structures. Despite sequence differences at the contact residue position (i.e., His to Gln substitution), MSX1 (PDB: 1IG7) and DLX3 (PDB: 4XRS) both form structures highly similar to ALX4 (Figure 6D). Although the amino acid identity could impact contact affinity, this is consistent with our ChIP data, suggesting that MSX1 and PRRX1 can also bind DNA at many of the same sites as ALX1/4 in hCNCCs (Figure 3D). To further test whether these additional HD TFs can indeed direct TWIST1 binding toward Coordinator, we transfected plasmids encoding TWIST1 with one of ALX4, MSX1, PRRX1 (two splice isoforms), or PHOX2A

Figure 6. The Coordinator motif guides TWIST1-homeodomain contact and cooperativity

(A) Immunoprecipitation-mass spectrometry (IP-MS) for TWIST1 using the V5 tag in undepleted (−dTAG, y axis) versus depleted (+dTAG, x axis) hCNCC protein extracts. Plotted data are the sum of two biological replicates.

(B) 3D structure of TWIST1 (aa101–170), TCF4 (aa565–624), and ALX4 (aa210–277) DNA-binding domains bound to the Coordinator DNA sequence. DNA bases recognized by the TFs are highlighted: cyan for TWIST1, green for TCF4, and magenta for ALX4.

(C) Zoomed-in view of contact between ALX4 and TWIST1.

(D) Sequence alignment of selected homeodomain TF loop sequences with sequence differences from ALX4 in bold and structural alignment of ALX4 with MSX1 (PDB: 1IG7) and DLX3 (PDB: 4XRS).

(E) TWIST1 preference for Coordinator motif upon homeodomain overexpression (see Figure S6A for protein levels). TWIST1 peaks ranked from the strongest to weakest in bins of 1,000 peaks.

(F) Extent of Coordinator-motif-binding preference of V5-tagged TWIST1 and various loop mutants expressed in HEK293 cells (see Figure S6A for protein levels) with or without ALX4. Inset: structural alignment of TWIST1 in our structure with the AlphaFold-predicted (AF) or experimentally solved (PDB: 2QL2 and 2YPA) structures of tested bHLH loops.

(G) EMSA probe sequences and gels, with Hill curve fits and estimated K_D and Hill coefficients (n).

See also Figure S6.

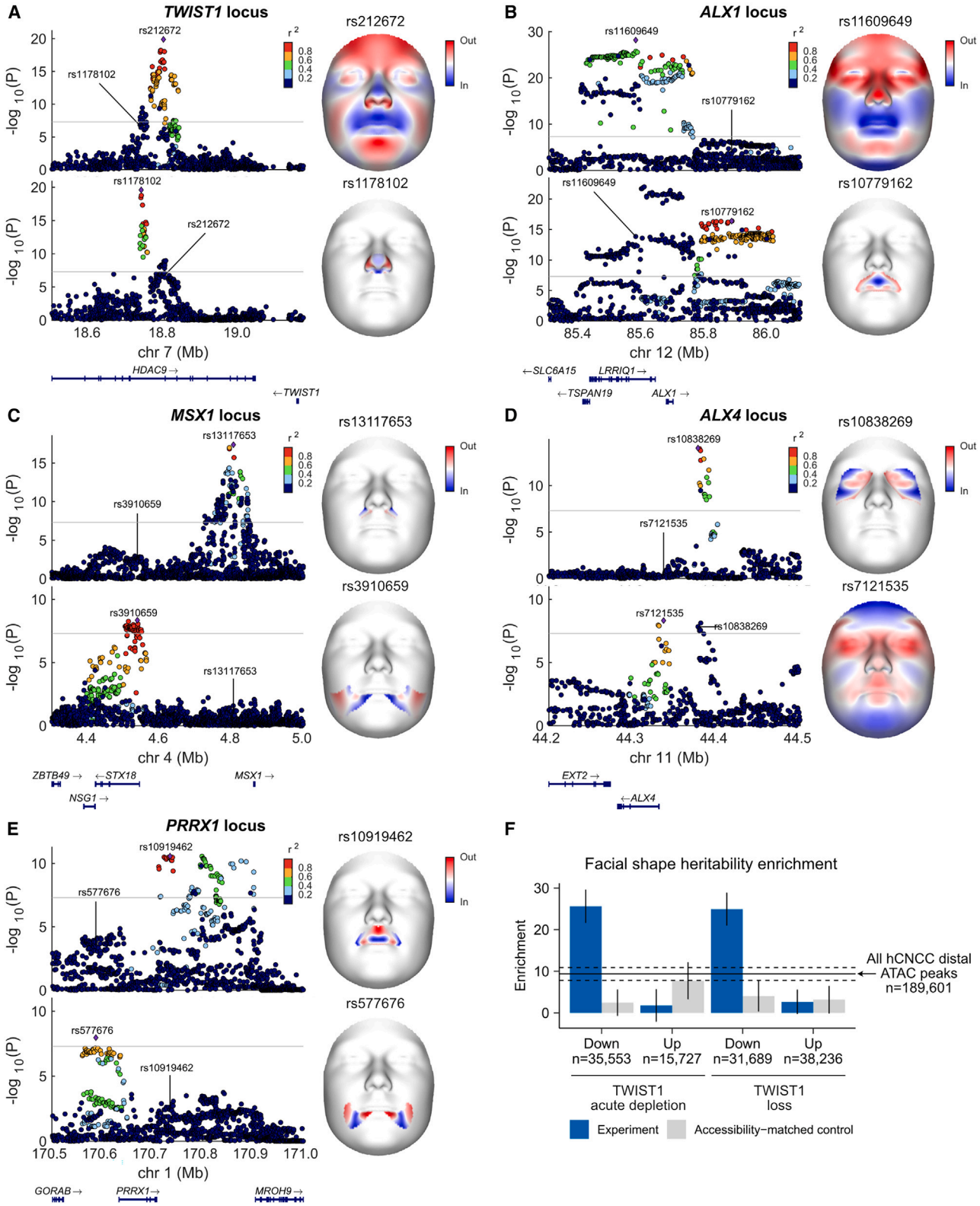

Figure 7. The roles of Coordinator-binding TFs and their targets in facial shape variation

(A–E) Facial shape effects associated with genetic variants at loci encoding Coordinator-binding TFs (A, *TWIST1*; B, *ALX1*; C, *MSX1*; D, *ALX4*; and E, *PRRX1*). LocusZoom plots (left) show SNPs plotted by p value of facial shape association and colored by linkage disequilibrium (r^2) to the lead SNP in each locus. Note that

(legend continued on next page)

into HEK293 cells and performed TWIST1 ChIP-seq. All tested HD TFs are capable of increasing TWIST1 binding to the Coordinator motif, but none as potently as ALX4 (Figure 6E), despite being expressed at comparable or higher protein levels (Figure S6A).

We next examined variation among bHLH TFs in loop sequence. In contrast to HDs, bHLH factors closely related to TWIST1, such as TAL1, HAND2, NEUROG2, and NEUROD1, adopt more distinct loop structures (Figure 6F) despite binding highly similar E-box motifs (Figure S2A). If the loop contact plays a key role in Coordinator-guided cooperativity between bHLH and HD, then replacing the bHLH loop of TWIST1 with that of the related bHLH TFs may prevent binding to Coordinator. To test this, we transfected HEK293 cells with plasmids encoding V5-tagged TWIST1 or a loop-swap mutant, each with or without ALX4, then performed ChIP-seq for the V5 tag. In addition, we tested full-length NEUROD1, which is the most divergent from TWIST1 of the examined bHLH TFs. All bHLH protein levels were comparable to or higher than that of WT TWIST1 (Figure S6A). Although WT TWIST1 binds the Coordinator motif robustly in the presence of ALX4, neither full-length NEUROD1 nor any of the loop-swap TWIST1 mutants do so (Figure 6F), instead binding to their known E-box motifs (Figure S6B). To pinpoint which amino acid changes drive this selective ALX4 cooperativity, we tested subsets (Figure S6C) and ultimately single amino acid substitutions and insertions (Figure 6F). Notably, all four single amino acid insertions strongly reduce cooperativity, regardless of the inserted residue or position. TWIST1's loop is among the shortest of all bHLH factors in humans; the longer loops of other bHLH TFs likely contribute to kinked structures incompatible with the ALX4 contact. In contrast to the critical role of loop length, none of the tested substitutions have a detectable effect on cooperativity, including the change of the ALX4-contacting proline residue (Figure 6F). This can be explained by the observation that the TWIST1 peptide backbone contacts ALX4, rather than a side chain. Collectively, these results illustrate how the cooperative binding of TWIST1 and HD TFs depends on the sequence and structure of the TWIST1 loop.

Importance of Coordinator DNA sequence features in TF cooperativity

If TWIST1-ALX4 cooperativity is mediated by weak protein interactions, it should also depend on the DNA sequence positioning the TFs at the right distance and angle. We tested this by repeating our original human-chimpanzee enhancer divergence analyses[19] with variant Coordinator motifs in which we extended or shortened the spacer between the HD and E-box motifs by up to 3 bases (Figure S6D; STAR Methods). Briefly, for each Coordinator motif variant, we calculated the correlation between the net change in motif p value and the change in H3K27ac signal in humans vs. chimps across all human-chimp divergent enhancers. This correlation ($r = 0.558$) was highly sensitive to spacer length, falling to $r < 0.16$ with even 1 bp changes.

To further test this idea *in vitro*, we performed electrophoretic mobility shift assays (EMSAs) with purified recombinant TWIST1, TCF3, and ALX4 DNA-binding domains and labeled DNA templates containing the consensus WT Coordinator motif or various DNA mutations (Figure S6E). We first confirmed that TWIST1:TCF3 dimer and ALX4 can independently bind the WT DNA at sufficiently high concentrations, but not templates in which their canonical motifs were abolished (Figures S6F and S6G). Upon titrating TWIST1:TCF3 in the presence of excess ALX4, TWIST1:TCF3-DNA binding occurs at ~2.5-fold lower concentrations and fits Hill equations with higher cooperativity coefficients (>2 vs. ~1.5) (Figures 6G and S6H). To test the role of DNA sequence in this cooperativity, we then assayed the effects of mutating the HD motif or changing the spacer length (from +2 to −2 bp). Strikingly, these mutations all eliminated TWIST1 cooperativity with ALX4, despite no effect on TWIST1:TCF3-DNA binding in the absence of ALX4 (Figure 6G).

Most native genomic instances of TWIST1-bound Coordinator motifs are imperfect. We, therefore, tested TWIST1 cooperativity with ALX4 at a partial E-box motif (CAGACG) (Figure S6I). Although independent TWIST1:TCF3 binding was reduced (~5- to 6-fold) as expected, cooperative binding with ALX4 was only mildly affected (<2-fold), indicating even greater cooperativity in this sequence context, with a net >10-fold decrease in K_D upon ALX4 addition. Finally, we tested whether the spacer sequence between the HD and E-box motifs affects TWIST1-ALX4 cooperativity by testing a DNA template with the As in the spacer replaced with Cs (Figure S6J). TWIST1:TCF3 binding is reduced (~2-fold) even in the absence of ALX4, consistent with protein-DNA contacts extending beyond the E-box in our structure and previous studies of bHLH recognition of DNA shape flanking the E-box motif.[56] This change in spacer sequence also affects cooperativity with ALX4; the estimated cooperativity coefficient is comparable to that of TWIST1:TCF3 in the absence of ALX4. Thus, the A-rich spacer preference may arise from both TWIST1:E-protein direct DNA recognition and the role of the spacer DNA shape in mediating TWIST1-ALX4 contact. Together, these results demonstrate how DNA sequence guides TWIST1-HD cooperativity by positioning the TFs next to each other.

The roles of Coordinator-binding TFs and their genomic targets in facial shape variation

We initially identified the Coordinator motif through an analysis of enhancer divergence between human and chimpanzee cranial neural crest (Figure 1A).[19] Having uncovered the *trans*-regulatory complex that binds Coordinator, we aimed to assess the potential impacts of the identified TFs and their genomic targets on human phenotypic variation. Our previous genome-wide association study (GWAS) identified over 200 loci associated with

p values are with respect to the trait of each lead SNP. Coordinates in hg19. Facial shape effect plots (right) show the normal displacement (displacement in the direction normal to the facial surface) for the facial region (Figure S7A) with the highest significance for each lead SNP.

(F) Facial shape heritability enrichment at TWIST1-dependent regulatory regions. Vertical line indicates enrichment in all hCNCC distal ATAC peaks; flanking dashed lines indicate error bars (SEM).

See also Figure S7.

normal-range variation in facial shape among individuals of European ancestry and revealed the enrichment of face-shape-associated genetic variants in CNCC enhancers.[57] To assess the contribution of Coordinator-binding TFs to human facial variation, we used two orthogonal approaches. In the first approach, we investigated the phenotypic impact of genetic variants at the loci encoding Coordinator-binding TFs. In the second approach, we focused on the enrichment of facial shape heritability at genomic targets regulated by Coordinator-binding TFs.

Examination of facial shape GWAS signals revealed that loci encoding each of the Coordinator-binding TFs analyzed in this study (i.e., *TWIST1*, *ALX1*, *ALX4*, *MSX1*, and *PRRX1*) have facial-shape-associated single-nucleotide polymorphisms (SNPs) in nearby non-coding regions, suggesting that quantitative changes in the expression of Coordinator-binding TFs may modulate the individual divergence of facial shape in humans (Figures 7A–7E). Given the complex and multifactorial nature of the human face, we previously used a multivariate approach to model the aspects of shape variation associated with a single SNP (STAR Methods; Figure S7A). Each of the five TF genes had two independent SNPs that reached genome-wide significance ($p < 5\times10^{-8}$), tens to hundreds of kilobases apart, with each having distinct effects on facial shape. For example, the SNP rs212672 near *TWIST1* has the most significant effects on the entire face, including shape changes in the forehead and chin, whereas rs1178102 ~60 kb upstream instead has the most significant effect on the shape of the nostrils (Figure 7A). These variants (with others in tight linkage) likely impact different context-specific *cis*-regulatory elements and thereby modulate TF expression in distinct spatiotemporal manners.

As further validation of the role of Coordinator-binding TFs in human facial shape, we examined another completely independent GWAS dataset relevant to the face. We previously conducted a GWAS for brain shape inferred from MRI scans,[58] which uncovered an unexpectedly large number of genes associated with variation in both brain and face shape. Although some of the shared brain-face loci are associated with genes known to play pleiotropic roles in both brain and facial development, others are near genes that are not expressed in the developing brain but instead are primarily expressed in CNCCs and the developing face. Among the top shared brain-face-shape-associated genes lacking expression in the brain (excluding mesenchyme in and around the brain) are *TWIST1*, *ALX1*, and *ALX4*. *TWIST1* has three independent genome-wide significant peaks in this brain shape GWAS, whereas *ALX1* and *ALX4* each have one (Figures S7B–S7D). Since these genes are not robustly expressed in the brain, the association with brain shape is, therefore, likely driven by the developing face, for example, through the control of regulatory programs modulating the ability of the facial mesenchyme to respond to and accommodate brain growth. Consistent with this possibility, the genetic effects of the *TWIST1*, *ALX1*, and *ALX4* on brain shape are enriched in the forebrain (Figures S7B–S7D), which develops in proximity to the face. Together, these observations indicate that all loci encoding TF components of the Coordinator *trans*-regulatory complex are implicated in human phenotypic variation.

Finally, we examined whether genomic targets regulated by Coordinator-binding TFs are disproportionately enriched for facial shape heritability. To assess the contributions of specific sets of genomic regions responsive to TF losses, we used stratified linkage disequilibrium score regression (S-LDSC) to determine the heritability enrichment of each set of regions compared with the following: (1) an accessibility-matched control set of hCNCC distal ATAC peaks (control) or (2) the entire set of hCNCC distal ATAC peaks (all peaks, including all putative CNCC enhancers that we have previously shown are enriched for facial shape heritability[57,59]) (Figure 7F). We first tested the set of distal regions differentially accessible within 3 h of acute TWIST1 depletion, separately assessing the upregulated and downregulated peaks. Notably, the downregulated, but not the upregulated, TWIST1-dependent peaks are highly enriched for the Coordinator motif. The downregulated peaks are also highly enriched for facial shape heritability (25.6-fold enrichment over the genome, in contrast to 2.44-fold enrichment in the control peaks [$p = 2.47 \times 10^{-6}$, downregulated vs. matched control peaks, t test] and 9.35-fold enrichment across all peaks [$p = 6.63 \times 10^{-5}$, downregulated vs. all peaks, t test]). In contrast, the upregulated peaks have a lower enrichment than either the matched or full control sets (Figure 7F). We observed similar results for the peaks differentially accessible upon long-term TWIST1 loss (Figure 7F).

When we repeated this analysis using the brain shape GWAS statistics, we again found a significant enrichment of the brain shape heritability at TWIST1-dependent, Coordinator-containing regulatory regions compared with various controls, although this enrichment was smaller than that for face shape heritability (as expected, given that most of the brain shape GWAS signals are relevant to brain development and not to facial development) (Figure S7E). Specifically, the distal ATAC-seq peaks that decrease in accessibility upon acute TWIST1 depletion were 13.7-fold enriched for brain shape heritability, compared with the 5.3-fold enrichment of accessibility-matched non-responsive ATAC-seq peaks ($p = 0.014$, t test) and 6.4-fold enrichment of all CNCC distal ATAC-seq peaks ($p = 0.0077$, t test). By contrast, ATAC-seq peaks that increase in accessibility upon TWIST1 depletion were instead depleted of brain shape GWAS heritability compared with the full set of CNCC distal ATAC-seq peaks. As a negative control, we analyzed the same genomic regions for the enrichment of an unrelated trait, height. Height does not show the same pattern of enrichment in downregulated peaks, although height GWAS signal is enriched in hCNCC distal ATAC peaks overall, likely due to shared programs for skeletal development being involved in both traits (Figure S7F). These results indicate that genetic variation in the Coordinator-containing, TWIST1-dependent regulatory regions ultimately modulates human facial shape. Together, these observations link Coordinator-binding TFs and their genomic targets to human phenotypic variation.

DISCUSSION

Although we first discovered the Coordinator motif through comparisons of human and chimpanzee CNCCs,[19] Coordinator is not restricted to primates or the developing face. Instead, Coordinator is selectively enriched at *cis*-regulatory regions of undifferentiated mesenchymal cells from both face and limb buds,

which have distinct embryonic origins (neural crest vs. mesoderm, respectively) but share the expression of many key TFs. Across species, we detected Coordinator enrichment in mouse and chick limb bud mesenchyme (Figure S1D).[60] However, although *Drosophila* have homologs of TWIST1 and its HD partners, with well-conserved DNA-binding domains, they have not been reported to bind Coordinator or similar composite motifs; this is in line with the emergence of neural crest and facial ectomesenchyme in vertebrates. Thus, evolutionarily ancient TFs can be repurposed for novel functions during the emergence of new cell types.

The TFs binding Coordinator have well-documented roles in face and limb development, as shown both in mouse models and by human genetics. For example, mouse knockouts of *Twist1*,[50,61] *Alx1*,[37] and *Alx4* (in combination with mutations of *Alx1* or *Alx3*)[37,62] all have strong craniofacial phenotypes that most profoundly manifest in the anterior facial regions. Similarly, Twist1,[63] Alx,[64] Msx,[54,65] and Prrx[66,67] factors are involved in limb development in mice. In humans, mutations in *TWIST1* are associated with the Saethre-Chotzen and Sweeney-Cox syndromes, characterized by facial dysmorphisms, craniosynostosis, and limb malformations[68,69]; mutations in genes encoding ALX TFs cause frontonasal dysplasias[70–73]; and mutations in *PRRX1* are associated with agnathia-otocephaly complex (the absence of mandible).[74] Our observations further suggest that *cis*-regulatory mutations that affect the Coordinator motif or the expression of its associated TFs play an important role in mediating inter- and intra-species phenotypic divergence in face shape. This role in phenotypic variation is likely not restricted to humans or primates: genetic variants in the *ALX1* locus are associated with beak shape in Darwin's finches,[75] whereas a *PRRX1* enhancer contributed to elongated forelimbs in bats.[76]

Embryonic development requires the placement of the right cell types in the right places. Coordinator-guided cooperativity between TWIST1, a well-known regulator of mesenchymal lineage, and HDs, many of which have been implicated in establishing or maintaining positional identity (e.g., along anterior-posterior or proximal-distal axes), may serve to coordinate cell type and positional information in the embryonic mesenchyme. TWIST1 is broadly expressed across the undifferentiated mesenchyme of the face and limb buds, where it has been shown to promote mesenchymal identity.[50,51,61] Beyond the face and limbs, TWIST1 functions in other processes associated with mesenchymal identity, such as during epithelial-to-mesenchymal transition in cancer cells[77] and mesoderm development in *Drosophila*,[78,79] but in these contexts, TWIST1 binds canonical solo and double E-box motifs.[35,80] Thus, TWIST1 performs distinct cellular and organismal functions, with Coordinator-guided cooperativity with HD TFs potentially enabling functions specific to face and limb development.

In contrast to the broad expression of TWIST1 across the developing mesenchyme, the expression of HD TFs is more regionally restricted (Figure 2D). ALXs and DLXs are expressed in, and involved in development of, the anterior and posterior facial structures, respectively,[38,81] whereas MSX and PRRX TFs are more broadly transcribed throughout the developing face.[81] The observation that Coordinator enrichment and TWIST1 binding at Coordinator sites are detectable in the regulatory regions of Md (Figures 1D and 2D), combined with the structural similarity of the DLX3 and ALX4 HDs (Figure 6D), suggests that in the developing jaw mesenchyme, TWIST1 likely also cooperates with the DLXs. However, the strength of Coordinator binding may contribute to the incipient divergence of facial regions, as the anterior-most FNP exhibits the highest Coordinator motif enrichment among TWIST1-binding sites (Figure 2B). Together with our observation that ALXs have the strongest cooperation with TWIST1 (Figure 6E), this may explain the prior observation that a conditional knockout of TWIST1 in the neural crest leads to the most dramatic phenotype (a near-complete loss) in the upper face derived from the FNP and Mx, whereas the mandible is less affected.[50]

Cooperation at Coordinator is remarkably selective among cell types and TFs, akin to the OCT4-SOX2 motif defining pluripotent stem cells. Even TFs with highly similar individual TF motifs that are co-expressed with some of the same candidate partner TFs are unable to cooperate: NEUROD1 cannot cooperate with ALX4 (Figure 6F), and in the developing forebrain, the abundant DLX factors do not bind Coordinator despite nearby enrichment of neurogenic bHLH TF motifs (Table S3).[82] Nevertheless, *in vitro*, other bHLH-HD TF pairs can co-bind composite motifs by CAP-SELEX,[10] so although Coordinator itself has not been seen in other cellular contexts, other TF pairs may be capable of co-binding distinct composite motifs. Furthermore, whether a given pair of TFs will preferentially bind at composite sites *in vivo* may depend not only on the strength of co-binding between the two partners but also on the milieu of other TFs capable of interactions with the cooperating TFs such as E-proteins and three amino acid loop extension (TALE)-type HD TFs[83] for bHLH and HD factors, respectively.

Limitations of the study

Most of the study was done in the *in-vitro*-derived hCNCCs that model anterior CNCCs. More work is needed to decipher which HD TFs cooperate with TWIST1 in other biological contexts where Coordinator is active, such as the more posterior CNCCs of the upper and lower jaw and limb bud mesenchyme. The crystal structure and EMSAs were performed with DNA-binding domains recombinantly expressed in *E. coli* and lack post-translational modifications and the disordered regions present in cells that may further regulate TF cooperativity. Facial and brain shape GWAS data were analyzed only for individuals of European ancestry in the US and UK; further work will be needed in other populations.

STAR★METHODS

Detailed methods are provided in the online version of this paper and include the following:

- KEY RESOURCES TABLE
- RESOURCE AVAILABILITY
  - Lead contact
  - Materials availability
  - Data and code availability
- EXPERIMENTAL MODEL AND STUDY PARTICIPANT DETAILS

SUPPLEMENTAL INFORMATION

Supplemental information can be found online at https://doi.org/10.1016/j.cell.2023.12.032.

ACKNOWLEDGMENTS

We thank Katherine Xue, Raquel Fueyo, Christina Jensen, Tiffany Chern, and Liang-Fu Chen for critical feedback and Hannah Long for generating the pGL3-noSV40-humanEC1.45_min1-2_4xE-boxMutant plasmid. Mass spectrometry data were collected by the Vincent Coates Foundation Mass Spectrometry Laboratory, Stanford University Mass Spectrometry (RRID: SCR_017801). This work was supported in part by NIH P30 CA124435 utilizing the Stanford Cancer Institute Proteomics/Mass Spectrometry Shared Resource. Protein production was performed by the Protein Sciences Facility in the Karolinska Institutet Department of Medical Biochemistry and Biophysics.

pAAV-GFP was a gift from John Gray (Addgene plasmid #32395), pDGM6 was a gift from David Russell (Addgene plasmid #110660), PB-iNEUROD1_P2A_GFP_Puro was a gift from Prashant Mali (Addgene plasmid #168803), and pCAG-NLS-HA-Bxb1 was a gift from Pawel Pelczar (Addgene plasmid #51271).

This work was supported by an HHMI-Damon Runyon Cancer Research Foundation fellowship (DRG-2420-21), a Stanford School of Medicine Dean's Postdoctoral Fellowship, and the NIH training grant 2T32AR007422-36A1 to S.K.; a Helen Hay Whitney Fellowship and NIH grant 1K99DE032729 to S.N.; BOF C1 KU Leuven C14/20/081 and NIH grant R01-DE027023 to P.C.; a Distinguished Professor Award from the Swedish Research Council to J.T.; and the NIH grant R35 GM131757, the Nomis Foundation, funding from the Howard Hughes Medical Institute, a Lorry Lokey endowed professorship, and a Stinehart Reed award to J.W.

AUTHOR CONTRIBUTIONS

Conceptualization, S.K., J.T., and J.W.; methodology, S.K., E.M., S.N., and M.K.; formal analysis, S.K., E.M., S.N., and S.G.; investigation, S.K., E.M., S.N., S.G., M.B., M.K., A. Popov, C.L., A. Pogson., T.S., P.C., J.T., and J.W.; writing – original draft, S.K. and J.W.; writing – review & editing, S.K., E.M., S.N., S.G., P.C, J.T., and J.W.; visualization, S.K., E.M., and S.G.; project administration, J.W.; supervision, J.W., J.T., and P.C.; funding acquisition, J.W., J.T., P.C., S.K., and S.N.

DECLARATION OF INTERESTS

J.W. is a paid scientific advisory board member at Camp4 and Paratus Sciences. J.T. has a consultancy agreement with DeepMind Technologies. J.W. is an advisory board member at Cell Press journals, including *Cell*, *Molecular Cell*, and *Developmental Cell*.

Received: April 20, 2023
Revised: October 23, 2023
Accepted: December 27, 2023
Published: January 22, 2024

REFERENCES

1. Kim, S., and Wysocka, J. (2023). Deciphering the multi-scale, quantitative cis-regulatory code. Mol. Cell *83*, 373–392.
2. Lambert, S.A., Jolma, A., Campitelli, L.F., Das, P.K., Yin, Y., Albu, M., Chen, X., Taipale, J., Hughes, T.R., and Weirauch, M.T. (2018). The Human Transcription Factors. Cell *172*, 650–665.
3. Lee, Q.Y., Mall, M., Chanda, S., Zhou, B., Sharma, K.S., Schaukowitch, K., Adrian-Segarra, J.M., Grieder, S.D., Kareta, M.S., Wapinski, O.L., et al. (2020). Pro-neuronal activity of Myod1 due to promiscuous binding to neuronal genes. Nat. Cell Biol. *22*, 401–411.
4. Lewis, E.B. (1978). A gene complex controlling segmentation in Drosophila. Nature *276*, 565–570.
5. Dennis, D.J., Han, S., and Schuurmans, C. (2019). bHLH transcription factors in neural development, disease, and reprogramming. Brain Res. *1705*, 48–65.
6. Murre, C. (2019). Helix–loop–helix proteins and the advent of cellular diversity: 30 years of discovery. Genes Dev. *33*, 6–25.
7. Berger, M.F., Badis, G., Gehrke, A.R., Talukder, S., Philippakis, A.A., Peña-Castillo, L., Alleyne, T.M., Mnaimneh, S., Botvinnik, O.B., Chan, E.T., et al. (2008). Variation in Homeodomain DNA Binding Revealed by High-Resolution Analysis of Sequence Preferences. Cell *133*, 1266–1276.
8. Jolma, A., Yan, J., Whitington, T., Toivonen, J., Nitta, K.R., Rastas, P., Morgunova, E., Enge, M., Taipale, M., Wei, G., et al. (2013). DNA-Binding Specificities of Human Transcription Factors. Cell *152*, 327–339.
9. Morgunova, E., and Taipale, J. (2017). Structural perspective of cooperative transcription factor binding. Curr. Opin. Struct. Biol. *47*, 1–8.
10. Jolma, A., Yin, Y., Nitta, K.R., Dave, K., Popov, A., Taipale, M., Enge, M., Kivioja, T., Morgunova, E., and Taipale, J. (2015). DNA-dependent formation of transcription factor pairs alters their binding specificity. Nature *527*, 384–388.
11. Li, P., Spolski, R., Liao, W., Wang, L., Murphy, T.L., Murphy, K.M., and Leonard, W.J. (2012). BATF-JUN is critical for IRF4-mediated transcription in T cells. Nature *490*, 543–546.

12. Luna-Zurita, L., Stirnimann, C.U., Glatt, S., Kaynak, B.L., Thomas, S., Baudin, F., Samee, M.A.H., He, D., Small, E.M., Mileikovsky, M., et al. (2016). Complex Interdependence Regulates Heterotypic Transcription Factor Distribution and Coordinates Cardiogenesis. Cell *164*, 999–1014.

13. Monahan, K., Schieren, I., Cheung, J., Mumbey-Wafula, A., Monuki, E.S., and Lomvardas, S. (2017). Cooperative interactions enable singular olfactory receptor expression in mouse olfactory neurons. eLife *6*, e28620.

14. Soufi, A., Garcia, M.F., Jaroszewicz, A., Osman, N., Pellegrini, M., and Zaret, K.S. (2015). Pioneer Transcription Factors Target Partial DNA Motifs on Nucleosomes to Initiate Reprogramming. Cell *161*, 555–568.

15. Michael, A.K., Grand, R.S., Isbel, L., Cavadini, S., Kozicka, Z., Kempf, G., Bunker, R.D., Schenk, A.D., Graff-Meyer, A., Pathare, G.R., et al. (2020). Mechanisms of OCT4-SOX2 motif readout on nucleosomes. Science *368*, 1460–1465.

16. Farley, E.K., Olson, K.M., Zhang, W., Brandt, A.J., Rokhsar, D.S., and Levine, M.S. (2015). Suboptimization of developmental enhancers. Science *350*, 325–328.

17. Sahu, B., Hartonen, T., Pihlajamaa, P., Wei, B., Dave, K., Zhu, F., Kaasinen, E., Lidschreiber, K., Lidschreiber, M., Daub, C.O., et al. (2022). Sequence determinants of human gene regulatory elements. Nat. Genet. *54*, 283–294.

18. De Val, S., Chi, N.C., Meadows, S.M., Minovitsky, S., Anderson, J.P., Harris, I.S., Ehlers, M.L., Agarwal, P., Visel, A., Xu, S.M., et al. (2008). Combinatorial regulation of endothelial gene expression by ets and forkhead transcription factors. Cell *135*, 1053–1064.

19. Prescott, S.L., Srinivasan, R., Marchetto, M.C., Grishina, I., Narvaiza, I., Selleri, L., Gage, F.H., Swigut, T., and Wysocka, J. (2015). Enhancer Divergence and cis-Regulatory Evolution in the Human and Chimp Neural Crest. Cell *163*, 68–83.

20. ENCODE Project Consortium, Moore, J.E., Purcaro, M.J., Pratt, H.E., Epstein, C.B., Shoresh, N., Adrian, J., Kawli, T., Davis, C.A., Dobin, A., et al. (2020). Expanded encyclopaedias of DNA elements in the human and mouse genomes. Nature *583*, 699–710.

21. Dong, R., Yang, R., Zhan, Y., Lai, H.D., Ye, C.J., Yao, X.Y., Luo, W.Q., Cheng, X.M., Miao, J.J., Wang, J.F., et al. (2020). Single-Cell Characterization of Malignant Phenotypes and Developmental Trajectories of Adrenal Neuroblastoma. Cancer Cell *38*, 716–733.e6.

22. Plikus, M.V., Wang, X., Sinha, S., Forte, E., Thompson, S.M., Herzog, E.L., Driskell, R.R., Rosenthal, N., Biernaskie, J., and Horsley, V. (2021). Fibroblasts: origins, definitions, and functions in health and disease. Cell *184*, 3852–3872.

23. Long, H.K., Osterwalder, M., Welsh, I.C., Hansen, K., Davies, J.O.J., Liu, Y.E., Koska, M., Adams, A.T., Aho, R., Arora, N., et al. (2020). Loss of Extreme Long-Range Enhancers in Human Neural Crest Drives a Craniofacial Disorder. Cell Stem Cell *27*, 765–783.e14.

24. Minoux, M., Holwerda, S., Vitobello, A., Kitazawa, T., Kohler, H., Stadler, M.B., and Rijli, F.M. (2017). Gene bivalency at Polycomb domains regulates cranial neural crest positional identity. Science *355*, eaal2913.

25. Harenza, J.L., Diamond, M.A., Adams, R.N., Song, M.M., Davidson, H.L., Hart, L.S., Dent, M.H., Fortina, P., Reynolds, C.P., and Maris, J.M. (2017). Transcriptomic profiling of 39 commonly-used neuroblastoma cell lines. Sci. Data *4*, 170033.

26. Paliou, C., Guckelberger, P., Schöpflin, R., Heinrich, V., Esposito, A., Chiariello, A.M., Bianco, S., Annunziatella, C., Helmuth, J., Haas, S., et al. (2019). Preformed chromatin topology assists transcriptional robustness of Shh during limb development. Proc. Natl. Acad. Sci. USA *116*, 12390–12399.

27. Andrey, G., Schöpflin, R., Jerković, I., Heinrich, V., Ibrahim, D.M., Paliou, C., Hochradel, M., Timmermann, B., Haas, S., Vingron, M., et al. (2017). Characterization of hundreds of regulatory landscapes in developing limbs reveals two regimes of chromatin folding. Genome Res. *27*, 223–233.

28. Di Giammartino, D.C., Kloetgen, A., Polyzos, A., Liu, Y., Kim, D., Murphy, D., Abuhashem, A., Cavaliere, P., Aronson, B., Shah, V., et al. (2019). KLF4 is involved in the organization and regulation of pluripotency-associated three-dimensional enhancer networks. Nat. Cell Biol. *21*, 1179–1190.

29. Marthandan, S., Baumgart, M., Priebe, S., Groth, M., Schaer, J., Kaether, C., Guthke, R., Cellerino, A., Platzer, M., Diekmann, S., et al. (2016). Conserved Senescence Associated Genes and Pathways in Primary Human Fibroblasts Detected by RNA-Seq. PLoS One *11*, e0154531.

30. Wang, L., Tang, Q., Xu, J., Li, H., Yang, T., Li, L., Machon, O., Hu, T., and Chen, Y. (2020). The transcriptional regulator MEIS2 sets up the ground state for palatal osteogenesis in mice. J. Biol. Chem. *295*, 5449–5460.

31. Tissières, V., Geier, F., Kessler, B., Wolf, E., Zeller, R., and Lopez-Rios, J. (2020). Gene Regulatory and Expression Differences between Mouse and Pig Limb Buds Provide Insights into the Evolutionary Emergence of Artiodactyl Traits. Cell Rep. *31*, 107490.

32. Oomen, M.E., Hansen, A.S., Liu, Y., Darzacq, X., and Dekker, J. (2019). CTCF sites display cell cycle-dependent dynamics in factor binding and nucleosome positioning. Genome Res. *29*, 236–249.

33. Risca, V.I., Denny, S.K., Straight, A.F., and Greenleaf, W.J. (2017). Variable chromatin structure revealed by in situ spatially correlated DNA cleavage mapping. Nature *541*, 237–241.

34. Zeid, R., Lawlor, M.A., Poon, E., Reyes, J.M., Fulciniti, M., Lopez, M.A., Scott, T.G., Nabet, B., Erb, M.A., Winter, G.E., et al. (2018). Enhancer invasion shapes MYCN-dependent transcriptional amplification in neuroblastoma. Nat. Genet. *50*, 515–523.

35. Chang, A.T., Liu, Y., Ayyanathan, K., Benner, C., Jiang, Y., Prokop, J.W., Paz, H., Wang, D., Li, H.R., Fu, X.D., et al. (2015). An evolutionarily conserved DNA architecture determines target specificity of the TWIST family bHLH transcription factors. Genes Dev. *29*, 603–616.

36. Desanlis, I., Kherdjemil, Y., Mayran, A., Bouklouch, Y., Gentile, C., Sheth, R., Zeller, R., Drouin, J., and Kmita, M. (2020). HOX13-dependent chromatin accessibility underlies the transition towards the digit development program. Nat. Commun. *11*, 2491.

37. Iyyanar, P.P.R., Wu, Z., Lan, Y., Hu, Y.C., and Jiang, R. (2022). Alx1 Deficient Mice Recapitulate Craniofacial Phenotype and Reveal Developmental Basis of ALX1-Related Frontonasal Dysplasia. Front. Cell Dev. Biol. *10*, 777887.

38. Minoux, M., and Rijli, F.M. (2010). Molecular mechanisms of cranial neural crest cell migration and patterning in craniofacial development. Development *137*, 2605–2621.

39. Barretina, J., Caponigro, G., Stransky, N., Venkatesan, K., Margolin, A.A., Kim, S., Wilson, C.J., Lehár, J., Kryukov, G.V., Sonkin, D., et al. (2012). The Cancer Cell Line Encyclopedia enables predictive modelling of anticancer drug sensitivity. Nature *483*, 603–607.

40. Rada-Iglesias, A., Bajpai, R., Prescott, S., Brugmann, S.A., Swigut, T., and Wysocka, J. (2012). Epigenomic Annotation of Enhancers Predicts Transcriptional Regulators of Human Neural Crest. Cell Stem Cell *11*, 633–648.

41. Bajpai, R., Chen, D.A., Rada-Iglesias, A., Zhang, J., Xiong, Y., Helms, J., Chang, C.P., Zhao, Y., Swigut, T., and Wysocka, J. (2010). CHD7 cooperates with PBAF to control multipotent neural crest formation. Nature *463*, 958–962.

42. Fan, X., Waardenberg, A.J., Demuth, M., Osteil, P., Sun, J.Q.J., Loebel, D.A.F., Graham, M., Tam, P.P.L., and Fossat, N. (2020). TWIST1 Homodimers and Heterodimers Orchestrate Lineage-Specific Differentiation. Mol. Cell. Biol. *40*, e00663-19.

43. Nabet, B., Roberts, J.M., Buckley, D.L., Paulk, J., Dastjerdi, S., Yang, A., Leggett, A.L., Erb, M.A., Lawlor, M.A., Souza, A., et al. (2018). The dTAG system for immediate and target-specific protein degradation. Nat. Chem. Biol. *14*, 431–441.

44. Nabet, B., Ferguson, F.M., Seong, B.K.A., Kuljanin, M., Leggett, A.L., Mohardt, M.L., Robichaud, A., Conway, A.S., Buckley, D.L., Mancias,

J.D., et al. (2020). Rapid and direct control of target protein levels with VHL-recruiting dTAG molecules. Nat. Commun. *11*, 4687.

45. Shaner, N.C., Lambert, G.G., Chammas, A., Ni, Y., Cranfill, P.J., Baird, M.A., Sell, B.R., Allen, J.R., Day, R.N., Israelsson, M., et al. (2013). A bright monomeric green fluorescent protein derived from Branchiostoma lanceolatum. Nat. Methods *10*, 407–409.
46. Naqvi, S., Kim, S., Hoskens, H., Matthews, H.S., Spritz, R.A., Klein, O.D., Hallgrímsson, B., Swigut, T., Claes, P., Pritchard, J.K., et al. (2023). Precise modulation of transcription factor levels identifies features underlying dosage sensitivity. Nat. Genet. *55*, 841–851.
47. Qu, S., Tucker, S.C., Zhao, Q., deCrombrugghe, B., and Wisdom, R. (1999). Physical and genetic interactions between Alx4 and Cart1. Development *126*, 359–369.
48. Zalc, A., Sinha, R., Gulati, G.S., Wesche, D.J., Daszczuk, P., Swigut, T., Weissman, I.L., and Wysocka, J. (2021). Reactivation of the pluripotency program precedes formation of the cranial neural crest. Science *371*, eabb4776.
49. Simões-Costa, M., and Bronner, M.E. (2015). Establishing neural crest identity: a gene regulatory recipe. Development *142*, 242–257.
50. Bildsoe, H., Loebel, D.A.F., Jones, V.J., Chen, Y.T., Behringer, R.R., and Tam, P.P.L. (2009). Requirement for Twist1 in frontonasal and skull vault development in the mouse embryo. Dev. Biol. *331*, 176–188.
51. Vincentz, J.W., Firulli, B.A., Lin, A., Spicer, D.B., Howard, M.J., and Firulli, A.B. (2013). Twist1 Controls a Cell-Specification Switch Governing Cell Fate Decisions within the Cardiac Neural Crest. PLoS Genet. *9*, e1003405.
52. Kos, R., Reedy, M.V., Johnson, R.L., and Erickson, C.A. (2001). The winged-helix transcription factor FoxD3 is important for establishing the neural crest lineage and repressing melanogenesis in avian embryos. Development *128*, 1467–1479.
53. Teng, L., Mundell, N.A., Frist, A.Y., Wang, Q., and Labosky, P.A. (2008). Requirement for Foxd3 in the maintenance of neural crest progenitors. Development *135*, 1615–1624.
54. Markman, S., Zada, M., David, E., Giladi, A., Amit, I., and Zelzer, E. (2023). A single-cell census of mouse limb development identifies complex spatiotemporal dynamics of skeleton formation. Dev. Cell *58*, 565–581.e4.
55. Connerney, J., Andreeva, V., Leshem, Y., Muentener, C., Mercado, M.A., and Spicer, D.B. (2006). Twist1 dimer selection regulates cranial suture patterning and fusion. Dev. Dyn. *235*, 1345–1357.
56. Gordân, R., Shen, N., Dror, I., Zhou, T., Horton, J., Rohs, R., and Bulyk, M.L. (2013). Genomic Regions Flanking E-Box Binding Sites Influence DNA Binding Specificity of bHLH Transcription Factors through DNA Shape. Cell Rep. *3*, 1093–1104.
57. White, J.D., Indencleef, K., Naqvi, S., Eller, R.J., Hoskens, H., Roosenboom, J., Lee, M.K., Li, J., Mohammed, J., Richmond, S., et al. (2021). Insights into the genetic architecture of the human face. Nat. Genet. *53*, 45–53.
58. Naqvi, S., Sleyp, Y., Hoskens, H., Indencleef, K., Spence, J.P., Bruffaerts, R., Radwan, A., Eller, R.J., Richmond, S., Shriver, M.D., et al. (2021). Shared heritability of human face and brain shape. Nat. Genet. *53*, 830–839.
59. Claes, P., Roosenboom, J., White, J.D., Swigut, T., Sero, D., Li, J., Lee, M.K., Zaidi, A., Mattern, B.C., Liebowitz, C., et al. (2018). Genome-wide mapping of global-to-local genetic effects on human facial shape. Nat. Genet. *50*, 414–423.
60. Ringel, A.R., Szabo, Q., Chiariello, A.M., Chudzik, K., Schöpflin, R., Rothe, P., Mattei, A.L., Zehnder, T., Harnett, D., Laupert, V., et al. (2022). Repression and 3D-restructuring resolves regulatory conflicts in evolutionarily rearranged genomes. Cell *185*, 3689–3704.e21.
61. Chen, Z.F., and Behringer, R.R. (1995). twist is required in head mesenchyme for cranial neural tube morphogenesis. Genes Dev. *9*, 686–699.
62. Beverdam, A., Brouwer, A., Reijnen, M., Korving, J., and Meijlink, F. (2001). Severe nasal clefting and abnormal embryonic apoptosis in Alx3/Alx4 double mutant mice. Development *128*, 3975–3986.
63. Krawchuk, D., Weiner, S.J., Chen, Y.T., Lu, B.C., Costantini, F., Behringer, R.R., and Laufer, E. (2010). Twist1 activity thresholds define multiple functions in limb development. Dev. Biol. *347*, 133–146.
64. Qu, S., Tucker, S.C., Ehrlich, J.S., Levorse, J.M., Flaherty, L.A., Wisdom, R., and Vogt, T.F. (1998). Mutations in mouse Aristaless-like4 cause Strong's luxoid polydactyly. Development *125*, 2711–2721.
65. Bensoussan-Trigano, V., Lallemand, Y., Saint Cloment, C., and Robert, B. (2011). Msx1 and Msx2 in limb mesenchyme modulate digit number and identity. Dev. Dyn. *240*, 1190–1202.
66. ten Berge, D., Brouwer, A., Korving, J., Martin, J.F., and Meijlink, F. (1998). Prx1 and Prx2 in skeletogenesis: roles in the craniofacial region, inner ear and limbs. Development *125*, 3831–3842.
67. Martin, J.F., Bradley, A., and Olson, E.N. (1995). The paired-like homeo box gene MHox is required for early events of skeletogenesis in multiple lineages. Genes Dev. *9*, 1237–1249.
68. Howard, T.D., Paznekas, W.A., Green, E.D., Chiang, L.C., Ma, N., Ortiz de Luna, R.I., Garcia Delgado, C., Gonzalez-Ramos, M., Kline, A.D., and Jabs, E.W. (1997). Mutations in TWIST, a basic helix–loop–helix transcription factor, in Saethre-Chotzen syndrome. Nat. Genet. *15*, 36–41.
69. Kim, S., Twigg, S.R.F., Scanlon, V.A., Chandra, A., Hansen, T.J., Alsubait, A., Fenwick, A.L., McGowan, S.J., Lord, H., Lester, T., et al. (2017). Localized TWIST1 and TWIST2 basic domain substitutions cause four distinct human diseases that can be modeled in Caenorhabditis elegans. Hum. Mol. Genet. *26*, 2118–2132.
70. Uz, E., Alanay, Y., Aktas, D., Vargel, I., Gucer, S., Tuncbilek, G., Eggeling, F. von, Yilmaz, E., Deren, O., Posorski, N., et al. (2010). Disruption of ALX1 Causes Extreme Microphthalmia and Severe Facial Clefting: Expanding the Spectrum of Autosomal-Recessive ALX-Related Frontonasal Dysplasia. Am. J. Hum. Genet. *86*, 789–796.
71. Kayserili, H., Uz, E., Niessen, C., Vargel, I., Alanay, Y., Tuncbilek, G., Yigit, G., Uyguner, O., Candan, S., Okur, H., et al. (2009). ALX4 dysfunction disrupts craniofacial and epidermal development. Hum. Mol. Genet. *18*, 4357–4366.
72. Twigg, S.R.F., Versnel, S.L., Nürnberg, G., Lees, M.M., Bhat, M., Hammond, P., Hennekam, R.C.M., Hoogeboom, A.J.M., Hurst, J.A., Johnson, D., et al. (2009). Frontorhiny, a Distinctive Presentation of Frontonasal Dysplasia Caused by Recessive Mutations in the ALX3 Homeobox Gene. Am. J. Hum. Genet. *84*, 698–705.
73. Mavrogiannis, L.A., Antonopoulou, I., Baxová, A., Kutílek, S., Kim, C.A., Sugayama, S.M., Salamanca, A., Wall, S.A., Morriss-Kay, G.M., and Wilkie, A.O. (2001). Haploinsufficiency of the human homeobox gene ALX4 causes skull ossification defects. Nat. Genet. *27*, 17–18.
74. Sergi, C., and Kamnasaran, D. (2011). PRRX1 is mutated in a fetus with agnathia-otocephaly. Clin. Genet. *79*, 293–295.
75. Lamichhaney, S., Berglund, J., Almén, M.S., Maqbool, K., Grabherr, M., Martinez-Barrio, A., Promerová, M., Rubin, C.J., Wang, C., Zamani, N., et al. (2015). Evolution of Darwin's finches and their beaks revealed by genome sequencing. Nature *518*, 371–375.
76. Cretekos, C.J., Wang, Y., Green, E.D., Martin, J.F., Rasweiler, J.J., and Behringer, R.R. (2008). Regulatory divergence modifies limb length between mammals. Genes Dev. *22*, 141–151.
77. Yang, J., Mani, S.A., Donaher, J.L., Ramaswamy, S., Itzykson, R.A., Come, C., Savagner, P., Gitelman, I., Richardson, A., and Weinberg, R.A. (2004). Twist, a Master Regulator of Morphogenesis, Plays an Essential Role in Tumor Metastasis. Cell *117*, 927–939.
78. Castanon, I., Von Stetina, S., Kass, J., and Baylies, M.K. (2001). Dimerization partners determine the activity of the Twist bHLH protein during Drosophila mesoderm development. Development *128*, 3145–3159.
79. Leptin, M. (1991). twist and snail as positive and negative regulators during Drosophila mesoderm development. Genes Dev. *5*, 1568–1576.

80. Zeitlinger, J., Zinzen, R.P., Stark, A., Kellis, M., Zhang, H., Young, R.A., and Levine, M. (2007). Whole-genome ChIP–chip analysis of Dorsal, Twist, and Snail suggests integration of diverse patterning processes in the Drosophila embryo. Genes Dev. *21*, 385–390.

81. Square, T., Jandzik, D., Romášek, M., Cerny, R., and Medeiros, D.M. (2017). The origin and diversification of the developmental mechanisms that pattern the vertebrate head skeleton. Dev. Biol. *427*, 219–229.

82. Lindtner, S., Catta-Preta, R., Tian, H., Su-Feher, L., Price, J.D., Dickel, D.E., Greiner, V., Silberberg, S.N., McKinsey, G.L., et al. (2019). Genomic Resolution of DLX-Orchestrated Transcriptional Circuits Driving Development of Forebrain GABAergic Neurons. Cell Rep. *28*, 2048–2063.e8.

83. Slattery, M., Riley, T., Liu, P., Abe, N., Gomez-Alcala, P., Dror, I., Zhou, T., Rohs, R., Honig, B., Bussemaker, H.J., et al. (2011). Cofactor Binding Evokes Latent Differences in DNA Binding Specificity between Hox Proteins. Cell *147*, 1270–1282.

84. Gray, J.T., and Zolotukhin, S. (2011). Design and construction of functional AAV vectors. Methods Mol. Biol. *807*, 25–46.

85. Hermann, M., Stillhard, P., Wildner, H., Seruggia, D., Kapp, V., Sánchez-Iranzo, H., Mercader, N., Montoliu, L., Zeilhofer, H.U., and Pelczar, P. (2014). Binary recombinase systems for high-resolution conditional mutagenesis. Nucleic Acids Res. *42*, 3894–3907.

86. Dailamy, A., Parekh, U., Katrekar, D., Kumar, A., McDonald, D., Moreno, A., Bagheri, P., Ng, T.N., and Mali, P. (2021). Programmatic introduction of parenchymal cell types into blood vessel organoids. Stem Cell Rep. *16*, 2432–2441.

87. Gregorevic, P., Blankinship, M.J., Allen, J.M., Crawford, R.W., Meuse, L., Miller, D.G., Russell, D.W., and Chamberlain, J.S. (2004). Systemic delivery of genes to striated muscles using adeno-associated viral vectors. Nat. Med. *10*, 828–834.

88. Melnikov, I., Svensson, O., Bourenkov, G., Leonard, G., and Popov, A. (2018). The complex analysis of X-ray mesh scans for macromolecular crystallography. Acta Crystallogr. D. Struct. Biol. *74*, 355–365.

89. Bourenkov, G.P., and Popov, A.N. (2010). Optimization of data collection taking radiation damage into account. Acta Crystallogr. D Biol. Crystallogr. *66*, 409–419.

90. Kabsch, W. (2010). XDS. Acta Crystallogr. D Biol. Crystallogr. *66*, 125–132.

91. Jiang, H., Lei, R., Ding, S.W., and Zhu, S. (2014). Skewer: a fast and accurate adapter trimmer for next-generation sequencing paired-end reads. BMC Bioinformatics *15*, 182.

92. Langmead, B., and Salzberg, S.L. (2012). Fast gapped-read alignment with Bowtie 2. Nat. Methods *9*, 357–359.

93. Danecek, P., Bonfield, J.K., Liddle, J., Marshall, J., Ohan, V., Pollard, M.O., Whitwham, A., Keane, T., McCarthy, S.A., Davies, R.M., et al. (2021). Twelve years of SAMtools and BCFtools. GigaScience *10*, giab008.

94. Zhang, Y., Liu, T., Meyer, C.A., Eeckhoute, J., Johnson, D.S., Bernstein, B.E., Nusbaum, C., Myers, R.M., Brown, M., Li, W., et al. (2008). Model-based Analysis of ChIP-Seq (MACS). Genome Biol. *9*, R137.

95. Quinlan, A.R., and Hall, I.M. (2010). BEDTools: a flexible suite of utilities for comparing genomic features. Bioinformatics *26*, 841–842.

96. Love, M.I., Huber, W., and Anders, S. (2014). Moderated estimation of fold change and dispersion for RNA-seq data with DESeq2. Genome Biol. *15*, 550.

97. Robinson, J.T., Thorvaldsdóttir, H., Winckler, W., Guttman, M., Lander, E.S., Getz, G., and Mesirov, J.P. (2011). Integrative Genomics Viewer. Nat. Biotechnol. *29*, 24–26.

98. Ramírez, F., Ryan, D.P., Grüning, B., Bhardwaj, V., Kilpert, F., Richter, A.S., Heyne, S., Dündar, F., and Manke, T. (2016). deepTools2: a next generation web server for deep-sequencing data analysis. Nucleic Acids Res. *44*, W160–W165.

99. Soneson, C., Love, M.I., and Robinson, M.D. (2016). Differential analyses for RNA-seq: transcript-level estimates improve gene-level inferences. F1000Res. *4*, 1521.

100. Neumann, T., Herzog, V.A., Muhar, M., von Haeseler, A., Zuber, J., Ameres, S.L., and Rescheneder, P. (2019). Quantification of experimentally induced nucleotide conversions in high-throughput sequencing datasets. BMC Bioinformatics *20*, 258.

101. Gupta, S., Stamatoyannopoulos, J.A., Bailey, T.L., and Noble, W.S. (2007). Quantifying similarity between motifs. Genome Biol. *8*, R24.

102. McLeay, R.C., and Bailey, T.L. (2010). Motif Enrichment Analysis: a unified framework and an evaluation on ChIP data. BMC Bioinformatics *11*, 165.

103. Grant, C.E., Bailey, T.L., and Noble, W.S. (2011). FIMO: scanning for occurrences of a given motif. Bioinformatics *27*, 1017–1018.

104. Ambrosini, G., Groux, R., and Bucher, P. (2018). PWMScan: a fast tool for scanning entire genomes with a position-specific weight matrix. Bioinformatics *34*, 2483–2484.

105. Bailey, T.L. (2021). STREME: accurate and versatile sequence motif discovery. Bioinformatics *37*, 2834–2840.

106. McCoy, A.J., Grosse-Kunstleve, R.W., Adams, P.D., Winn, M.D., Storoni, L.C., and Read, R.J. (2007). Phaser crystallographic software. J. Appl. Crystallogr. *40*, 658–674.

107. Adams, P.D., Afonine, P.V., Bunkóczi, G., Chen, V.B., Davis, I.W., Echols, N., Headd, J.J., Hung, L.W., Kapral, G.J., Grosse-Kunstleve, R.W., et al. (2010). PHENIX: a comprehensive Python-based system for macromolecular structure solution. Acta Crystallogr. D Biol. Crystallogr. *66*, 213–221.

108. Winn, M.D., Ballard, C.C., Cowtan, K.D., Dodson, E.J., Emsley, P., Evans, P.R., Keegan, R.M., Krissinel, E.B., Leslie, A.G.W., McCoy, A., et al. (2011). Overview of the CCP4 suite and current developments. Acta Crystallogr. D Biol. Crystallogr. *67*, 235–242.

109. Murshudov, G.N., Vagin, A.A., and Dodson, E.J. (1997). Refinement of macromolecular structures by the maximum-likelihood method. Acta Crystallogr. D Biol. Crystallogr. *53*, 240–255.

110. Emsley, P., Lohkamp, B., Scott, W.G., and Cowtan, K. (2010). Features and development of Coot. Acta Crystallogr. D Biol. Crystallogr. *66*, 486–501.

111. Schrödinger, LLC (2015). The PyMOL Molecular Graphics System, Version 1.8. https://pymol.org/sites/default/files/pymol_0.xml.

112. Schindelin, J., Arganda-Carreras, I., Frise, E., Kaynig, V., Longair, M., Pietzsch, T., Preibisch, S., Rueden, C., Saalfeld, S., Schmid, B., et al. (2012). Fiji: an open-source platform for biological-image analysis. Nat. Methods *9*, 676–682.

113. Finucane, H.K., Bulik-Sullivan, B., Gusev, A., Trynka, G., Reshef, Y., Loh, P.R., Anttila, V., Xu, H., Zang, C., Farh, K., et al. (2015). Partitioning heritability by functional annotation using genome-wide association summary statistics. Nat. Genet. *47*, 1228–1235.

114. Sekhon, J.S. (2011). Multivariate and Propensity Score Matching Software with Automated Balance Optimization: The Matching package for R. J. Stat. Softw. *42*, 1–52.

115. Kent, W.J., Sugnet, C.W., Furey, T.S., Roskin, K.M., Pringle, T.H., Zahler, A.M., and Haussler, D. (2002). The Human Genome Browser at UCSC. Genome Res. *12*, 996–1006.

116. Corces, M.R., Trevino, A.E., Hamilton, E.G., Greenside, P.G., Sinnott-Armstrong, N.A., Vesuna, S., Satpathy, A.T., Rubin, A.J., Montine, K.S., Wu, B., et al. (2017). An improved ATAC-seq protocol reduces background and enables interrogation of frozen tissues. Nat. Methods *14*, 959–962.

117. Meers, M.P., Bryson, T.D., Henikoff, J.G., and Henikoff, S. (2019). Improved CUT&RUN chromatin profiling tools. eLife *8*, e46314.

118. Liu, N., Hargreaves, V.V., Zhu, Q., Kurland, J.V., Hong, J., Kim, W., Sher, F., Macias-Trevino, C., Rogers, J.M., Kurita, R., et al. (2018). Direct

Promoter Repression by BCL11A Controls the Fetal to Adult Hemoglobin Switch. Cell *173*, 430–442.e17.

119. Herzog, V.A., Reichholf, B., Neumann, T., Rescheneder, P., Bhat, P., Burkard, T.R., Wlotzka, W., von Haeseler, A., Zuber, J., and Ameres, S.L. (2017). Thiol-linked alkylation of RNA to assess expression dynamics. Nat. Methods *14*, 1198–1204.
120. Savitsky, P., Bray, J., Cooper, C.D.O., Marsden, B.D., Mahajan, P., Burgess-Brown, N.A., and Gileadi, O. (2010). High-throughput production of human proteins for crystallization: the SGC experience. J. Struct. Biol. *172*, 3–13.
121. Morgunova, E., Yin, Y., Jolma, A., Dave, K., Schmierer, B., Popov, A., Eremina, N., Nilsson, L., and Taipale, J. (2015). Structural insights into the DNA-binding specificity of E2F family transcription factors. Nat. Commun. *6*, 10050.
122. Yin, Y., Morgunova, E., Jolma, A., Kaasinen, E., Sahu, B., Khund-Sayeed, S., Das, P.K., Kivioja, T., Dave, K., Zhong, F., et al. (2017). Impact of cytosine methylation on DNA binding specificities of human transcription factors. Science *356*, eaaj2239.
123. Zander, U., Bourenkov, G., Popov, A.N., de Sanctis, D., Svensson, O., McCarthy, A.A., Round, E., Gordeliy, V., Mueller-Dieckmann, C., and Leonard, G.A. (2015). MeshAndCollect: an automated multi-crystal data-collection workflow for synchrotron macromolecular crystallography beamlines. Acta Crystallogr. D Biol. Crystallogr. *71*, 2328–2343.
124. Patro, R., Duggal, G., Love, M.I., Irizarry, R.A., and Kingsford, C. (2017). Salmon provides fast and bias-aware quantification of transcript expression. Nat. Methods *14*, 417–419.
125. Khan, A., Fornes, O., Stigliani, A., Gheorghe, M., Castro-Mondragon, J.A., van der Lee, R., Bessy, A., Chèneby, J., Kulkarni, S.R., Tan, G., et al. (2018). JASPAR 2018: update of the open-access database of transcription factor binding profiles and its web framework. Nucleic Acids Res. *46*, D260–D266.
126. Kulakovskiy, I.V., Vorontsov, I.E., Yevshin, I.S., Sharipov, R.N., Fedorova, A.D., Rumynskiy, E.I., Medvedeva, Y.A., Magana-Mora, A., Bajic, V.B., Papatsenko, D.A., et al. (2018). HOCOMOCO: towards a complete collection of transcription factor binding models for human and mouse via large-scale ChIP-Seq analysis. Nucleic Acids Res. *46*, D252–D259.
127. Vierstra, J., Lazar, J., Sandstrom, R., Halow, J., Lee, K., Bates, D., Diegel, M., Dunn, D., Neri, F., Haugen, E., et al. (2020). Global reference mapping of human transcription factor footprints. Nature *583*, 729–736.
128. Elias, J.E., and Gygi, S.P. (2007). Target-decoy search strategy for increased confidence in large-scale protein identifications by mass spectrometry. Nat. Methods *4*, 207–214.
129. Purcell, S., Neale, B., Todd-Brown, K., Thomas, L., Ferreira, M.A.R., Bender, D., Maller, J., Sklar, P., Bakker, P.I.W. de, Daly, M.J., et al. (2007). PLINK: A Tool Set for Whole-Genome Association and Population-Based Linkage Analyses. Am. J. Hum. Genet. *81*, 559–575.
130. Tashman, K.C., Cui, R., O'Connor, L.J., Neale, B.M., and Finucane, H.K. (2021). Significance testing for small annotations in stratified LD-Score regression. Preprint at medRxiv.

STAR★METHODS

KEY RESOURCES TABLE

REAGENT or RESOURCE	SOURCE	IDENTIFIER
Antibodies		
Mouse monoclonal TWIST1 (WT, ChIP, CUT&RUN)	Abcam	Cat# ab50887; RRID:AB_883294
Mouse monoclonal ALX4 (WB, CUT&RUN)	Novus Bio	Cat# NBP2-45490; RRID:AB_3073561
Rabbit polyclonal ALX1 (WB) – discontinued	Novus Bio	Cat# NBP1-88189
Rabbit polyclonal MSX1 (WB) – discontinued	Origene	Cat# TA590129
Mouse monoclonal PRRX1 (WB)	Santa Cruz Biotechnology	Cat# sc-293386; RRID:AB_3073562
Rabbit polyclonal CTCF (WB, CUT&RUN)	Cell Signaling	Cat# 2899; RRID:AB_2086794
Rabbit monoclonal HSP90 (WB)	Cell Signaling	Cat# 4877; RRID:AB_2233307
Rabbit monoclonal V5 tag (WB, IP)	Abcam	Cat# ab206566; RRID:AB_2819156
Mouse monoclonal Flag tag (WB)	Sigma	Cat# F1804; RRID:AB_262044
Donkey polyclonal anti-rabbit IgG (H+L) HRP (WB)	Jackson Immunoresearch	Cat# 711-035-152; RRID:AB_10015282
Goat polyclonal anti-mouse IgG (H+L) HRP (WB)	Jackson Immunoresearch	Cat# 115-005-003; RRID:AB_2338447
Rabbit polyclonal V5 tag (ChIP)	Abcam	Cat# ab15828; RRID:AB_443253
Rabbit polyclonal H3K27ac (ChIP)	Active Motif	Cat# 39133; RRID:AB_2561016
Rabbit monoclonal AP-2α (ChIP, CUT&RUN)	Cell Signaling	Cat# 3215; RRID:AB_2227429
Mouse monoclonal AP-2α (ChIP)	Novus Bio	Cat# NB100-74359; RRID:AB_1048155
Mouse monoclonal TCF3 (E2A) (CUT&RUN)	Santa Cruz Biotechnology	Cat# sc-133074; RRID:AB_2199147
Rabbit polyclonal anti-mouse IgG (H+L) (CUT&RUN)	Abcam	Cat# ab46540; RRID:AB_2614925
Chemicals, peptides, and recombinant proteins		
mTeSR 1	Stem Cell Technologies	Cat# 85850
Matrigel Growth Factor Reduced (GFR) Basement Membrane Matrix	Corning	Cat# 356231
ReLeSR	Stem Cell Technologies	Cat# 05872
mTeSR Plus	Stem Cell Technologies	Cat# 100-0276
RPMI-1640	Gibco	Cat# 11875093
Antibiotic-antimycotic	Sigma-Aldrich	Cat# A5955
DMEM High glucose with L-glutamine, sodium pyruvate	Cytiva	Cat# SH30243.01
GlutaMAX	Gibco	Cat# 35050061
Non-essential amino acids	Gibco	Cat# 1114-0050
Complete ES Cell Medium with 15% FBS	Millipore	Cat# ES-101-B
mLIF	Millipore	Cat# ESG1107
SpeI-HF	NEB	Cat# R3133S
XbaI	NEB	Cat# R0145S
Gibson assembly master mix	NEB	Cat# E2611S
SalI-HF	NEB	Cat# R3138S
BclI	NEB	Cat# R0160S
Polyethylenimine	Sigma	Cat# 408719
Opti-MEM	Gibco	Cat# 31985070

(*Continued on next page*)

Continued

REAGENT or RESOURCE	SOURCE	IDENTIFIER
Benzonase	Millipore	Cat# 71205-3
OptiPrep Density Gradient medium	Sigma-Aldrich	Cat# D1556-250ML
Pluronic F-68	Gibco	Cat# 240 4-0032
Turbo DNase	Invitrogen	Cat# AM2238
Collagenase IV	Gibco	Cat# 17104019
KnockOut DMEM	Gibco	Cat# 10829018
DMEM/F12 1:1 medium, with L-glutamine; without HEPES	Cytiva	Cat# SH30271.FS
Neurobasal Medium	Gibco	Cat# 21103049
N2 NeuroPlex	Gemini Bio	Cat# 400-163
Gem21 NeuroPlex	Gemini Bio	Cat# 400-160
EGF	Peprotech	Cat# AF-100-15
bFGF	Peprotech	Cat# 100-18B
Bovine insulin	Gemini Bio	Cat# 700-112P
Accutase	Sigma-Aldrich	Cat# A6964-100ML
Human fibronectin	Millipore	Cat# FC010-10MG
BSA	Gemini Bio	Cat# 700-104P
BMP2	Peprotech	Cat# 120-02
CHIR-99021	Selleckchem	Cat# S2924
$dTAG^V$-1	Tocris	Cat# 6914/5
Y-27632 RHO/ROCK pathway inhibitor	Stem Cell Technologies	Cat# 72304
Alt-R *S.p.* HiFi Cas9 nuclease V3	Integrated DNA Technologies	Cat# 1081059
QuickExtract DNA Extraction Solution	Lucigen	Cat# QE9050
Lipofectamine 2000	Invitrogen	Cat# 11668019
FuGENE 6	Promega	Cat# E2691
cOmplete EDTA-free protease inhibitor cocktail	Roche	Cat# 11873580001
NuPAGE LDS Sample Buffer	Invitrogen	Cat# NP0007
4-12% Novex Tris-glycine gels	Invitrogen	Cat# XV04125PK20
4-20% Novex Tris-glycine gels	Invitrogen	Cat# XV04205PK20
Nitrocellulose membrane	GE Healthcare	Cat# 10600003
Amersham enhanced chemiluminescence (ECL) Prime reagent	Cytiva	Cat# RPN2232
DNase I	Worthington	Cat# LS006331
Ampure XP beads	Beckman Coulter	Cat# A63881
Methanol-free 16% formaldehyde solution	Pierce	Cat# 28908
RNase A	Thermo	Cat# EN0531
Proteinase K	Thermo	Cat# EO0491
Dynabeads Protein A	Invitrogen	Cat# 10002D
Dynabeads Protein G	Invitrogen	Cat# 10004D
Concanavalin A beads	Epicypher	Cat# 21-1401
pAG-MNase	Epicypher	Cat# 15-1016
E. coli spike-in DNA	Epicypher	Cat# 18-1401
TRIzol	Invitrogen	Cat# 15596018
4-thiouridine	Carbosynth	Cat# NT06186
Iodoacetamide	G Biosciences	Cat# 786-078
0.05% Trypsin-EDTA	Gibco	Cat# 25300054
phosSTOP	Roche	Cat# 4906845001

(*Continued on next page*)

Continued

REAGENT or RESOURCE	SOURCE	IDENTIFIER
Trypsin/LysC	Promega	Cat# V5071
0.02% ProteaseMax	Promega	Cat# V2071
NEBuffer 2	NEB	Cat# B7002S
LightShift Poly (dI-dC)	Thermo	Cat# 20148E
Critical commercial assays		
OptiSeal tubes	Beckman Coulter	Cat# 362183
Amicon Ultra-15 100K filter	Millipore	Cat# UFC910008
LightCycler 480 Probes Master	Roche	Cat# 04707494001
P3 Primary Cell 4D-Nucleofector X Kit L	Lonza	Cat# V4XP-3034
Quick-DNA mini prep kit	Zymo	Cat# D3024
Dual-Luciferase Reporter assay kit	Promega	Cat# E1960
BCA Protein Assay	Thermo	Cat# 23225
TD enzyme	Illumina	Cat# 20034197
DNA Clean & Concentrator-5	Zymo	Cat# D4013
NEBNext Ultra II Q5 master mix	NEB	Cat# M0544
Qubit dsDNA high sensitivity	Invitrogen	Cat# Q33231
TPX 1.5 ml tubes	Diagenode	Cat# c30010010-50
ChIP DNA Clean & Concentrator-5	Zymo	Cat# D5205
NEBNext Ultra II DNA	NEB	Cat# E7645S
RNA Clean & Concentrator-5	Zymo	Cat# R1013
Qubit RNA broad range assay	Invitrogen	Cat# Q10210
QuantSeq 3' mRNA-Seq Library Prep FWD	Lexogen	Cat# 113.96
Direct-zol RNA miniprep	Zymo	Cat# R2052
Dynabeads Antibody Coupling kit	Invitrogen	Cat# 14311D
JCSG crystallization kit	Molecular Dimensions	Cat# MD1-37
Deposited data		
ChIP-seq, ATAC-seq, CUT&RUN, RNA-seq	This paper	GEO: GSE230319
Crystal structure of TWIST1, TCF4, ALX4 bound to DNA	This paper	PDB: 8OSB
Experimental models: Cell lines		
Human: Female H9 human embryonic stem cells (hESCs)	WiCell	WA09; RRID:CVCL_9773
Human: Female RS4;11 cells	ATCC	CRL-1873; RRID:CVCL_0093
Human: Female HEK293 cells	ATCC	CRL-1573; RRID:CVCL_0045
Human: Female 293FT cells	Invitrogen	R70007; RRID:CVCL_6911
Mouse: O9-1 cells	Millipore	SCC049; RRID:CVCL_GS42
Experimental models: Organisms/strains		
Mouse: CD-1	Charles River Laboratories	RRID:MGI:5649524
Oligonucleotides		
Primers for cloning and genotyping, see Table S5		N/A
HDR oligos and gRNAs for CRISPR/Cas9 editing, see Table S5		N/A
Recombinant DNA		
pAAV-GFP	Gray and Zolotukhin[84]	Addgene 32395
pCAG-NLS-HA-Bxb1	Hermann et al.[85]	Addgene 51271
PB-iNEUROD1_P2A_GFP_Puro	Dailamy et al.[86]	Addgene 168803
pAAV-hSOX9-dTAG-mNeonGreen-V5	Naqvi et al.[46]	Addgene 194971

(*Continued on next page*)

Continued

REAGENT or RESOURCE	SOURCE	IDENTIFIER
pDGM6	Gregorevic et al.[87]	Addgene 110660
pRL	Promega	N/A
pGL3-SV40_control	Promega	N/A
pUC19	NEB	Cat# N3041S
pGL3-noSV40	Long et al.[23]	N/A
pGL3-noSV40humanEC1.45_min1-2	Long et al.[23]	Addgene 173952
pcDNA3.1_MSX1-Flag	Genscript	OHu18516D
pcDNA3.1_PRRX1a-Flag	Genscript	OHu23742D
pcDNA3.1_PRRX1b-Flag	Genscript	OHu15551D
pcDNA3.1_PHOX2A-Flag	Genscript	OHu18020D
pAAV_FKBP-V5-TWIST1	This paper	N/A
pAAV_FKBP-V5-ALX1	This paper	N/A
pAAV_FKBP-V5-PRRX1	This paper	N/A
pAAV_MSX1-FKBP-mNeonGreen-V5	This paper	N/A
pGL3-noSV40-humanEC1.45_min1-2_4XEboxMutant	This paper	N/A
pCAG_TWIST1	This paper	N/A
pCAG_ALX4-Flag-HA	This paper	N/A
pcDNA3.1_ALX4-Flag	This paper	N/A
pcDNA3.1_V5-TWIST1	This paper	N/A
pcDNA3.1_V5-NEUROD1	This paper	N/A
pcDNA3.1_V5-TWIST1_NEUROD1loop	This paper	N/A
pcDNA3.1_V5-TWIST1_NEUROG2loop	This paper	N/A
pcDNA3.1_V5-TWIST1_HAND2loop	This paper	N/A
pcDNA3.1_V5-TWIST1_TAL1loop	This paper	N/A
pcDNA3.1_V5-TWIST1_NEUROD1ins	This paper	N/A
pcDNA3.1_V5-TWIST1_NEUROG2ins	This paper	N/A
pcDNA3.1_V5-TWIST1_HAND2ins	This paper	N/A
pcDNA3.1_V5-TWIST1_TAL1ins	This paper	N/A
pcDNA3.1_V5-TWIST1_P139S	This paper	N/A
pcDNA3.1_V5-TWIST1_L138Y	This paper	N/A
pcDNA3.1_V5-TWIST1_L138F	This paper	N/A
pcDNA3.1_V5-TWIST1_NEUROD1L	This paper	N/A
pcDNA3.1_V5-TWIST1_NEUROD1R	This paper	N/A
pcDNA3.1_V5-TWIST1_NEUROD1M	This paper	N/A
Software and algorithms		
Dozor-MeshBest	Melnikov et al.[88]	N/A
BEST	Bourenkov and Popov[89]	https://www.embl-hamburg.de/BEST/
XDS	Kabsch[90]	https://xds.mr.mpg.de/
skewer v0.2.2	Jiang et al.[91]	https://github.com/relipmoc/skewer
bowtie2 v2.4.1	Langmead and Salzberg[92]	https://bowtie-bio.sourceforge.net/bowtie2/index.shtml
samtools v1.10	Danecek et al.[93]	https://samtools.sourceforge.net/
MACS2 v2.2.7.1	Zhang et al.[94]	https://github.com/macs3-project/MACS
Bedtools	Quinlan and Hall[95]	https://github.com/arq5x/bedtools2
DESeq2	Love et al.[96]	https://bioconductor.org/packages/release/bioc/html/DESeq2.html
IGV v2.7.2	Robinson et al.[97]	https://igv.org/

(*Continued on next page*)

Continued

REAGENT or RESOURCE	SOURCE	IDENTIFIER
Deeptools	Ramirez et al.[98]	https://deeptools.readthedocs.io/en/develop/index.html
Tximport	Soneson et al.[99]	https://bioconductor.org/packages/release/bioc/html/tximport.html
slamdunk v0.4.3	Neumann et al.[100]	https://t-neumann.github.io/slamdunk/
MEME Suite v5.1.1 TOMTOM	Gupta et al.[101]	https://meme-suite.org/meme/doc/download.html
MEME Suite v5.1.1 AME	McLeay and Bailey[102]	https://meme-suite.org/meme/doc/download.html
MEME Suite v5.1.1 FIMO	Grant et al.[103]	https://meme-suite.org/meme/doc/download.html
PWMScan	Ambrosini et al.[104]	https://epd.expasy.org/pwmtools/pwmtools/
MEME Suite v5.1.1 STREME	Bailey et al.[105]	https://meme-suite.org/meme/doc/download.html
MEME Suite v4.12.0 ceqlogo	Timothy Bailey lab	https://meme-suite.org/meme/doc/download.html
Preview	Protein Metrics	https://proteinmetrics.com/resources/preview-a-program-for-surveying-shotgun-proteomics-tandem-mass-spectrometry-data/
Byonic	Protein Metrics	https://proteinmetrics.com/byonic/
Phaser	McCoy et al.[106]	https://www.phaser.cimr.cam.ac.uk/index.php/Phaser_Crystallographic_Software
Phenix	Adams et al.[107]	https://phenix-online.org/
CCP4	Winn et al.[108]	https://www.ccp4.ac.uk/
REFMAC5	Murshudov et al.[109]	https://www.ccp4.ac.uk/
Coot	Emsley et al.[110]	https://www2.mrc-lmb.cam.ac.uk/personal/pemsley/coot/
PyMOL	Schrödinger, LLC[111]	https://www.pymol.org/2
Fiji	Schindelin et al.[112]	https://fiji.sc/
LD score regression v1.0.1	Finucane et al.[113]	https://github.com/bulik/ldsc
Matching package for R v4.10-8	Sekhon[114]	https://cran.r-project.org/web/packages/Matching/index.html
UCSC Kent tools	Kent et al.[115]	https://genome.ucsc.edu/
Original code	This paper	https://zenodo.org/doi/10.5281/zenodo.7847852
Other		
Beckman VTi 50 rotor	Beckman Coulter	N/A
Bioruptor Plus	Diagenode	N/A
Amersham ImageQuant 800	Cytiva	N/A
Countess II	Invitrogen	N/A
NovaSeq X Plus	Illumina	N/A
NovaSeq 6000	Illumina	N/A
HiSeq X Ten	Illumina	N/A
Acquity M-Class UPLC	Waters	N/A
Orbitrap Q Exactive HF-X	Thermo	RRID:SCR_018703
Orbitrap Exploris 480	Thermo	RRID:SCR_022215
LightCycler 480	Roche	N/A
Lonza 4D-Nucleofector	Lonza	N/A

RESOURCE AVAILABILITY

Lead contact

Further information and requests for resources and reagents should be directed to and will be fulfilled by the Lead Contact, Joanna Wysocka (wysocka@stanford.edu).

Materials availability

Plasmids generated in this study will be deposited in Addgene upon publication. All other reagents are available upon request.

Data and code availability

- All sequencing datasets have been deposited in NCBI GEO and are publicly available at accession GEO: GSE230319. Accession numbers of reanalyzed publicly available datasets are listed in Table S4. ENCODE datasets were downloaded from https://www.encodeproject.org/. CCLE data were downloaded from https://depmap.org/portal/download/all/, Release 22Q1 "CCLE_expression.csv" and "sample_info.csv". Mass spectrometry peptide spectrum match counts are provided in Table S1. The TWIST1-TCF4-ALX4 crystal structure atomic coordinates and diffraction data have been deposited to Protein Data Bank under accession PDB: 8OSB.
- All original code have been deposited to Zenodo and is publicly available as of the date of publication. DOI is listed in the key resources table.
- Any additional information required to reanalyze the data reported in this paper is available from the lead contact upon request.

EXPERIMENTAL MODEL AND STUDY PARTICIPANT DETAILS

Cell culture

Female H9 cells (WiCell, WA09, RRID:CVCL_9773) were cultured in feeder-free conditions, in mTeSR1 medium (Stem Cell Technologies, 85850) on Matrigel Growth Factor Reduced (GFR) Basement Membrane Matrix (Corning, 356231) and passaged using ReLeSR (Stem Cell Technologies, 05872) every 4-6 days. Cells were switched to mTeSR Plus medium (Stem Cell Technologies, 100-0276) prior to and during genome editing and clonal expansion, but switched back to mTeSR1 before differentiation to CNCC.

Female RS4;11 cells (ATCC, CRL-1873, RRID:CVCL_0093) were cultured in RPMI-1640 medium (Gibco, 11875093) supplemented with 10% v/v FBS and 1x antibiotic/antimycotic.

Female HEK293 cells (ATCC, CRL-1573, RRID:CVCL_0045) and female 293FT cells (Invitrogen, R70007, RRID:CVCL_6911) were cultured in DMEM high glucose medium with sodium pyruvate and L-glutamine, supplemented with 10% v/v FBS and 1x GlutaMAX, non-essential amino acids, and antibiotic/antimycotic.

Mixed male and female O9-1 cells (Millipore, SCC049, RRID:CVCL_GS42) used for spike-in controls for ChIPs of TWIST1 depletions were cultured in Complete ES Cell Medium with 15% FBS (Millipore, ES-101-B), 25 ng/ml bFGF, and mLIF (Millipore, ESG1107).

Animal procedures

CD-1 mice (RRID:MGI:5649524) were obtained from Charles River Laboratories and housed in RAFII facility at Stanford University. Animal care and all procedures were conducted in accordance with the Stanford University Administrative Panel on Laboratory Animal Care (under pre-approved protocol APLAC-30364). For timed pregnancies, an 8-week old female CD-1 mouse was introduced to a cage with a single >10-week old CD-1 male and monitored for plugs. The noon of the day that a vaginal plug was detected was considered E0.5. Pregnant mice were sacrificed at E10.5 for dissections of facial prominences and limb buds from mixed male and female embryos.

METHOD DETAILS

Oligonucleotides

Primers used in this study are listed in Table S5.

Plasmids and cloning

AAV donor templates were cloned into the pAAV-GFP (Addgene plasmid # 32395) backbone by digesting pAAV-GFP with SpeI-HF (NEB, R3133S) and XbaI (NEB, R0145S) and performing Gibson assembly (NEB, E2611S) with PCR products of the ~1 kb homology arms and tags. Flexible linkers (glycine-serine or glycine-alanine) of 5-11 aa were added in between the degron and epitope tags and the TF of interest.

Plasmids in the pCAG backbone used to overexpress TWIST1 and ALX4 in HEK293 cells were cloned by digesting the pCAG-NLS-HA-Bxb1 plasmid (Addgene plasmid # 51271) prepared from dam-/dcm- *E. coli* (NEB, C2925H) with SalI-HF (NEB, R3138S) and BclI (NEB, R0160S) followed by Gibson assembly with PCR products of desired inserts.

Plasmids in the pcDNA3.1 backbone used to overexpress V5-tagged TWIST1/NEUROD1 and ALX4 in HEK293 cells were cloned by PCR of the pcDNA3.1 backbone and desired inserts followed by Gibson assembly.

Coding sequences of MSX1 (NM_002448.3, OHu18516D), PRRX1a (NM_006902.5, OHu23742D), PRRX1b (NM_022716.4, OHu15551D), PHOX2A (NM_005169.4, OHu18020D) were ordered from Genscript. TWIST1 was amplified from H9 gDNA, with tags added following the second ATG at the beginning of the coding sequence. NEUROD1 was amplified from PB-iNEUROD1_P2A_GFP_Puro (Addgene plasmid # 168803). FKBP12^{F36V}-V5 (for N-terminal tagging) was synthesized by Integrated DNA Technologies. FKBP12^{F36V}-mNeonGreen-V5 (for C-terminal tagging) was amplified from pAAV-hSOX9-dTAG-mNeonGreen-V5 (Addgene plasmid #194971).

The pGL3-noSV40-humanEC1.45_min1-2_4xEboxMutant plasmid was generated by mutating all four E-box motifs within Coordinator motifs *in silico* at the positions with greatest information content in the PWM. The sequence containing mutant EC1.45 E-box motifs was ordered from Twist Bioscience and cloned into the pGL3 luciferase reporter vector.

AAV preparation

AAV production was performed by transfecting 293FT cells with 22 ug of pDGM6 helper plasmid (Addgene plasmid # 110660), 6 ug of donor template plasmid, and 120 ug polyethylenimine (Sigma-Aldrich, 408719) diluted in Opti-MEM (Gibco, 31985070) in 1 ml total volume per 15-cm plate (4 plates were used per construct). Twenty-four hours after transfection, media was changed to media with 2% FBS. Three days after transfection, cells were harvested by scraping, triturated by pipetting up and down, centrifuged at 1000g for 20 min at 4°C, resuspended in 1.5 ml AAV lysis buffer (2 mM $MgCl_2$, 10 mM NaCl) per 2x15 cm plates, and then flash frozen for storage. Samples were passaged through a 23-gauge needle and then freeze-thawed three additional cycles to lyse cells. Lysates were then treated with Benzonase (Millipore, 71205-3) for 1 h at 37°C with intermittent mixing, centrifuged at 2000g for 20 min at 4°C, and then the supernatant was flash frozen for storage at -80°C. OptiSeal tubes (Beckman Coulter, 362183) were filled from the bottom (with a blunt 18-gauge needle attached to a syringe), in order, with layers of 9.7 ml of 25% OptiPrep Density Gradient medium (Sigma-Aldrich, D1556-250ML) in 100 mM Tris pH 7.6, 1.5 M NaCl, 100 mM $MgCl_2$; 6.4 ml of 41.7% OptiPrep in 100 mM Tris pH 7.6, 0.5 M NaCl, 100 mM $MgCl_2$, and 12 ug/ml Phenol Red; 5.4 ml of 66.7% in 100 mM Tris pH 7.6, 0.5 M NaCl, 100 mM $MgCl_2$, and 5.4 ml of 96.7% OptiPrep Density Gradient medium (Sigma-Aldrich, D1556-250ML) in 33.3 mM Tris pH 7.6, 167 mM NaCl, 33 mM $MgCl_2$ with 0.012 mg/ml Phenol Red. Lysate was gently added on top, the tubes were filled with AAV lysis buffer, and centrifuged at 48,000 rpm at 18°C in a Beckman Vti 50 rotor for 70 min with max acceleration and braking at a setting of 9. The viral fraction above the 66.7%-96.7% OptiPrep interface was collected using an 18-gauge needle and syringe and then washed with cold PBS using an Amicon Ultra-15 100K filter (Millipore, UFC910008). Pluronic F-68 (Gibco, 240 4-0032) was added to 0.001% v/v final and then purified AAV was then flash frozen in aliquots for storage at -80°C. To calculate AAV titers, an aliquot was digested with Turbo DNase (Invitrogen, AM2238) per manufacturer's instructions, inactivated with 1 mM EDTA final concentration and incubation at 75°C for 10 min, and then digested with proteinase K in 1 M NaCl and 1% w/v N-lauroylsarcosine at 50°C for 2h. Samples were then boiled for 10 min, and diluted in H_2O to 1:20,000 and 1:200,000. DNA standards comprising 10^{10} – 10^3 molecules were prepared using AAV6 backbone plasmids containing inverted terminal repeats. Quantitative PCR was carried out on standards and test samples using the LightCycler 480 Probes Master kit (Roche, 04707494001) with inverted terminal repeat probe and primer sequences indicated in Table S5.

Differentiation of hESC to hCNCCs

hESCs were differentiated to hCNCCs as previously described.[19,23] Briefly, hESC colonies were partially detached from the plate with collagenase IV (Gibco, 17104019) in Knockout DMEM medium (Gibco, 10829018) for 30-60 min and scraped to break up large colonies, and then cultured in Neural Crest Differentiation Medium (50%-50% v/v mixture of DMEM/F12 1:1 medium with L-glutamine, without HEPES (Cytiva, SH30271.FS) and Neurobasal medium (Gibco, 21103049) with 0.5x N2 NeuroPlex (Gemini Bio, 400-163) and Gem21 NeuroPlex (Gemini Bio, 400-160) supplements and GlutaMAX (Gibco, 35050061), and 1x antibiotic/antimycotic, and 20 ng/ml EGF (Peprotech, AF-100-15), 20 ng/ml bFGF (Peprotech, 100-18B), and 5 ug/ml bovine insulin (Gemini Bio, 700-112P)) for 11 days in bacterial-grade petri dishes, changing the plate to prevent attachment for 4 days and then leaving the cells unfed for two days to allow attachment, and then fed as needed at least every other day. At day 11, cells (now called 'early hCNCC') were harvested by treatment with Accutase (Sigma-Aldrich, A6964-100ML), strained to remove residual neuroectodermal spheres, and plated onto plates coated with 7.5 ug/ml human fibronectin (Millipore, FC010-10MG) and cultured in Neural Crest Maintenance Medium (Neural Crest Differentiation Medium with bovine insulin replaced by 1 mg/ml BSA (Gemini Bio, 700-104P)). These hCNCC were then passaged every 2-3 days upon reaching confluency, with cells in the third or subsequent passages defined as 'late hCNCC' and cultured with added 50 pg/ml BMP2 (Peprotech, 120-02) and 3 uM CHIR-99021 (Selleckchem, S2924).

dTAG treatment

dTAG^V-1 (Tocris, 6914/5) was dissolved in DMSO at 5 mM and then diluted to 250 uM in 60% DMSO/40% water (v/v) before dilution to 500 nM for acute depletions (up to 1 day) or diluted directly from the 5 mM stock for long-term depletions. For acute depletion time courses, an equivalent amount of DMSO (0.12% v/v final) was added to all samples starting 24 h before harvest, and cells for all time points were harvested simultaneously.

Genome editing

H9 cells were treated with 10 uM Y-27632 (Stem Cell Technologies, 72304) for at least 2 h prior to nucleofection, and then harvested as single cells with Accutase. For each editing experiment, 800,000 cells were nucleofected with 1.7 ul (17 ug) Alt-R S.p. HiFi Cas9 nuclease V3 (Integrated DNA Technologies) and 3.3 ul of 100 uM annealed crRNA XT and tracrRNA (pre-incubated for 15 min at room temperature to form RNPs) and for generating ALX4 knockout, 2 ul of 100 uM ssDNA homology-directed repair (HDR) template, using the P3 Primary Cell 4D-Nucleofector X Kit L (Lonza, V4XP-3034) and the CA-137 program. When AAV was used to deliver HDR template, the AAV was diluted to 25,000 viral genomes per cell in medium and added to the plate before adding the nucleofected cells. Media was changed 4 h after nucleofection, and then cells were cultured until nearing confluency, at which point cells were diluted to single cells and plated at low densities (~500 cells per well of a 6-well plate). Resulting colonies were picked and a portion of the cells lysed by QuickExtract (Lucigen, QE9050) and used to genotype by PCR with primers on either side of the insertion site (in most cases with one primer outside the homology arms; see Table S5 for primer sequences) and gel electrophoresis or Sanger sequencing. Putatively edited colonies were confirmed by genomic DNA extraction using the Quick-DNA mini prep kit (Zymo, D3024) and Sanger sequencing. All gRNA and primer sequences are listed in Table S5.

Transfection

HEK293 cells were transfected with Lipofectamine 2000 (Invitrogen, 11668019) at a ratio of 2.8 ul lipofectamine per ug of DNA, diluted in Opti-MEM. Cells were transfected with 2.5 ug DNA per well of a 6-well plate or 15 ug DNA per 10-cm plate 1-2 days after seeding, when they reached 70-90% confluency. Media was replaced 4-6h after transfection, and then cells were harvested for Western blot or chromatin immunoprecipitation at 24 h after transfection. For the initial TWIST1/ALX4 transfections, equal amounts of pCAG_TWIST1, pCAG_ALX4-Flag-HA, and pUC19 were transfected. For transfections with V5-tagged TWIST1/NEUROD1, to normalize plasmid amounts, the following amounts of plasmids were transfected per well of a 6-well plate (and six-fold more for a 10-cm plate, and the remaining amount filled with pUC19 as carrier): 200 ng pcDNA3.1_ALX4-Flag, 2000 ng pcDNA3.1_MSX1-Flag, 200 ng pcDNA3.1_PRRX1a-Flag, 200 ng pcDNA3.1_PRRX1b-Flag, 200 ng pcDNA3.1_PHOX2A-Flag, 200 ng pcDNA3.1_V5-TWIST1, 1200 ng pcDNA3.1_V5-NEUROD1, 300 ng pcDNA3.1_V5-TWIST1_P139S, and 200 ng for all other TWIST1 mutants.

hCNCCs were transfected with FuGENE 6 (Promega, E2691) immediately after passaging, using 1 ul of FuGENE 6 per 3 ug of DNA and 100 ng DNA diluted in 50 ul Opti-MEM per well of a 24-well plate.

Luciferase assay

hCNCCs were transfected with 0.5 ng pRL renilla control plasmid, 10 ng modified pGL3 reporter plasmid, and 89.5 ng carrier plasmid (pUC19) per well of a 24-well plate, in triplicate. Cells were lysed 24 h after transfection and assayed with the Dual-Luciferase Reporter assay kit (Promega, E1960).

Western blot

Cells were washed with cold PBS, lysed by incubation for 10 min on ice in RIPA buffer (50 mM Tris pH 7.6, 150 mM NaCl, 1% Igepal CA-630, 0.5% sodium deoxycholate, 0.1% SDS) with 1x cOmplete EDTA-free protease inhibitor cocktail (Roche, 11873580001), and sonicated for 6 cycles of 30s ON/30s OFF on high power using the Bioruptor Plus (Diagenode). Insoluble material was removed by centrifugation at >16,000g for 10 min at 4°C. The supernatant was quantified by BCA protein assay (Thermo, 23225) and then denatured by addition of 1x NuPAGE LDS Sample Buffer (Invitrogen, NP0007) and 100 mM DTT and heating to 95°C for 7 min. Samples were normalized by BCA quantifications and then loaded in 4-12% or 4-20% Novex Tris-glycine gels (Invitrogen) and run at 165V for ~1 h in Tris-glycine buffer (25 mM Tris and 192 mM glycine) with 0.1% SDS. Gels were transferred onto nitrocellulose membranes (GE Healthcare) for 1 h at 400 mA in Tris-glycine buffer with 20% methanol, stained with 0.1% Ponceau S in 3% trichloroacetic acid, then blocked with 5% milk and 1% BSA in PBS with 0.1% Tween-20 (PBST) for 15 min at room temperature, and then incubated with primary antibody overnight at 4°C followed by horseradish peroxidase (HRP)-conjugated secondary antibody incubation for 1 h at room temperature, with 4 washes of PBST after each antibody incubation. Antibodies used include TWIST1 (Abcam, ab50887, RRID:AB_883294, 1:500), ALX4 (Novus Bio, NBP2-45490, 1:1000), ALX1 (Novus Bio, NBP1-88189, 1:1000), MSX1 (Origene, TA590129, 1:5000), PRRX1 (Santa Cruz Biotechnology, sc-293386, 1:500), CTCF (Cell Signaling, 2899, 1:2000), HSP90 (Cell Signaling, 4877, 1:2000), V5 (Abcam, ab206566, RRID:AB_2819156, 1:2000), Flag (Sigma, F1804, 1:2000), HA (Abcam, ab9110, 1:2000), Donkey anti-Rabbit IgG (H+L) HRP (Jackson Immunoresearch, 711-035-152, RRID:AB_10015282, 1:3000), Goat anti-Mouse IgG (H+L) HRP (Jackson Immunoresearch, 115-005-003, RRID:AB_2338447, 1:3000). Chemiluminescence was performed with Amersham enhanced chemiluminescence (ECL) Prime reagent (Cytiva, RPN2232) and imaged with an Amersham ImageQuant 800 (Amersham).

ATAC-seq

Omni-ATAC was performed essentially as published,[116] with 30 min treatment with 200 U/ml Dnase I (Worthington, LS006331) at 37°C prior to harvesting cells, using Ampure XP (Beckman Coulter, A63881) beads to clean up the DNA. Briefly, treated cells were harvested by Accutase, counted using the Countess II (Invitrogen), and 50,000 cells were collected by centrifugation at 500g for 5 min at 4°C. Cells were resuspended in lysis buffer (resuspension buffer (RSB), or 10 mM Tris-HCl pH 7.4, 10 mM NaCl, and 3 mM $MgCl_2$, with 0.1% Igepal CA-630, 0.1% Tween-20, and 0.01% digitonin) for 3 min, then quenched by dilution with RSB

with 0.1% Tween-20. Lysate was centrifuged for 10 min at 500g at 4°C and then resuspended in transposition buffer (25 ul TD buffer and 2.5 ul TD enzyme (Illumina, 20034197), 16.5 ul PBS, 0.01% digitonin, 0.1% Tween-20, and water up to 50 ul). Transposition reactions were performed for 30 min at 37°C, and then cleaned up with the DNA Clean & Concentrator-5 kit (Zymo, D4013) and eluted in 21 ul 10 mM Tris-HCl pH 8. DNA was then pre-amplified 5 cycles with NEBNext Ultra II Q5 master mix (NEB, M0544) with a cycling protocol of 72°C for 5 min, 98°C for 30s, and 5 cycles of 98°C for 10s, 63°C for 30s, 72°C for 1 min. Then 5 ul of the 50 ul reaction was used to run a qPCR reaction (with the same cycling protocol except the initial 72°C incubation) to determine the optimal number of PCR cycles for each sample. The remaining portion of the reaction was then amplified the appropriate number of cycles, and then subjected to two rounds of double-sided Ampure XP bead cleanup, with 0.5x/1.3x and 0.5x/1.0x bead ratios (numbers indicate bead ratios added in first and second steps). Libraries were quantified by Qubit dsDNA high sensitivity assay (Invitrogen, Q33231), run on a 5% polyacrylamide TBE gel to check the size distribution, and then pooled for sequencing.

Chromatin immunoprecipitation

Cells (about 1 confluent 10-cm plate or ~10-20 million cells) were crosslinked with 1% methanol-free formaldehyde (Pierce, 28908) in PBS for 10 min at room temperature and then quenched by adding 2.5 M glycine to 125 mM final concentration and incubating for 10 min. Cells were washed in PBS with 0.001% v/v Triton X-100, harvested by scraping, and collected by centrifugation for 5 min at 4°C. Cells were washed with PBS and flash frozen for storage at -80°C. Cell pellets were later thawed on ice for 30 min, and then sequentially resuspended in lysis buffer 1 (50 mM HEPES-KOH pH 7.5, 140 mM NaCl, 1 mM EDTA, 10% glycerol, 0.5% Igepal CA-630, 0.25% Triton X-100, 1x cOmplete EDTA-free protease inhibitor cocktail (PIC), 1 mM PMSF), lysis buffer 2 (10 mM Tris-HCl pH 8, 200 mM NaCl, 1 mM EDTA, 0.5 mM EGTA, 1x cOmplete EDTA-free protease inhibitor cocktail, 1 mM PMSF), and lysis buffer 3 (10 mM Tris-HCl pH 8, 100 mM NaCl, 1 mM EDTA, 0.5 mM EGTA, 0.1% sodium deoxycholate, 0.5% N-lauroylsarcosine, 1x PIC, 1 mM PMSF), with 10 min incubations in each buffer, with rotation. Lysates were sonicated for 10-15 cycles of 30s ON/30s OFF on high power using the Bioruptor Plus (Diagenode), then diluted in additional lysis buffer 3 and clarified by centrifugation for 10 min at max speed at 4°C. Triton X-100 was added to 1%, and a small aliquot was used to extract DNA to check chromatin yield and size distribution, by dilution in elution buffer (1% w/v SDS and 100 mM $NaHCO_3$) and incubation with 200 mM NaCl and Rnase A (Thermo, EN0531) at 65°C for 1 h, then proteinase K (Thermo, EO0491) at 65°C for 1 h, and clean up with the ChIP DNA Clean & Concentrator-5 kit (Zymo, D5205). DNA was quantified by Qubit dsDNA high sensitivity kit, and the remaining chromatin was then normalized for immunoprecipitations. For TWIST1 acute depletions, chromatin from O9-1 mouse CNCCs were added prior to ChIP at ~10% of the total chromatin as a spike-in control. Antibodies used include TWIST1 (Abcam, ab50887), V5 (Abcam, ab15828), H3K27ac (Active Motif, 39133), Flag (Sigma-Aldrich, F1804), AP-2α (Cell Signaling, 3215), AP-2α (Novus Bio, NB100-74359). For H3K27ac, 5 ug of antibody was used per ChIP; for TFs, 9 ug of antibody was used per ChIP, except for dissected mouse embryos where 4.5 ug was used in half of the total ChIP volume. ChIPs were incubated overnight, then incubated for 4-6h with 100 ul Dynabeads Protein A (Invitrogen, 10002D) or Protein G (Invitrogen, 10004D) prewashed with 0.1% w/v BSA in PBS, then washed 5x with RIPA wash buffer (50 mM HEPES-KOH pH 7.5, 500 mM LiCl, 1 mM EDTA, 1% Igepal CA-630, 0.7% w/v sodium deoxycholate), once with 50 mM Tris-HCl pH 8, 10 mM EDTA, 50 mM NaCl, and eluted in elution buffer at 65°C for 30 min. Eluate was then reverse crosslinked and treated with RNase A and proteinase K, and then DNA was extracted with the ChIP DNA Clean & Concentrator-5 kit. ChIP-seq libraries were prepared using the NEBNext Ultra II DNA kit (NEB, E7645S) using up to 50 ng of input or ChIP DNA, with ~4-8 cycles of amplification, with no pre-PCR size selection but a post-PCR double-sided 0.5x/0.9x Ampure XP bead clean-up.

CUT&RUN

The CUTANA CUT&RUN (Epicypher) protocol and reagents (concanavalin A beads, 21-1401 and pAG-MNase, 15-1016) were used with minor modifications based on the protocol from ref Meers et al.[117]: digestion was performed for 30 min on ice, and digestion supernatant was treated with 0.1% w/v SDS and 0.25 mg/ml proteinase K at 50°C for 1 h and then phenol-chloroform extraction was performed to extract DNA. Primary antibody incubations were performed overnight, and secondary antibody was used for mouse antibodies (TWIST1, ALX4, TCF3). Antibodies used include TWIST1 (Abcam, ab50887, 1:25), ALX4 (Novus Bio, NBP2-45490), TCF3 (Santa Cruz Biotechnology, sc-133074, 1:50), AP-2α (Cell Signaling, 3215, 1:25), CTCF (Cell Signaling, 2899, 1:25), V5 (Abcam, ab206566, 1:100), Rabbit anti-mouse IgG (H+L) (Abcam, ab46540, 1:100). *E. coli* spike-in DNA (Epicypher, 18-1401) was added at 0.01 ng per reaction. Library prep was performed with modifications to the NEBNext Ultra II DNA kit as in https://doi.org/10.17504/protocols.io.bagaibse.[118]

SLAM-seq and RNA-seq

Cells were harvested by TRIzol (Invitrogen, 15596018) and stored at -80°C until processing. Chloroform was added to TRIzol lysate and separated into aqueous and organic phases by centrifugation per manufacturer instructions, and then the aqueous fraction was extracted using the RNA Clean & Concentrator-5 (Zymo, R1013) with on-column Dnase I digestion. RNA was checked for purity by Nanodrop and was quantified by Qubit RNA broad range assay (Invitrogen, Q10210). RNA-seq libraries were prepared using the QuantSeq 3' mRNA-Seq Library Prep FWD kit (Lexogen, 113.96) using 500 ng of input RNA and ~15 cycles of amplification, with unique dual indices.

For acute depletions, SLAM-seq[119] was performed as described with minor modifications, with 4-thiouridine (100 uM) labeling of nascent transcription for the last 2 h prior to harvest. Briefly, RNA was extracted using the Direct-zol RNA miniprep kit (Zymo, R2052),

modified to include 0.1 mM DTT in wash buffers and 1 mM DTT to the water for elution, with protection from light. Four ug of RNA was then alkylated with 10 mM iodoacetamide (G Biosciences, 786-078) dissolved in ethanol at 100 mM, in 50% v/v DMSO, 50 mM $NaPO_4$ pH 8 for 15 min at 50°C. Alkylation was quenched by addition of 1 ul of 1 M DTT, and alkylated RNA was extracted by RNA Clean & Concentrator-5 kit.

Sequencing

Illumina sequencing libraries were sequenced using 150 bp paired-end reads on the NovaSeq X Plus, NovaSeq 6000, HiSeq X Ten platforms.

Embryo dissection

Frontonasal prominences (FNP), maxillary prominences (Mx), mandibular prominences (Md), forelimb buds (FL), and hindlimb buds (HL) of E10.5 mouse embryos were microdissected in cold PBS, and then washed twice with cold PBS, and treated with 0.05% trypsin-EDTA (Gibco, 25300054) at 37°C for 30 min, shaking at 750 rpm. Trypsin was quenched by addition of FBS, then cells were dissociated to single cells by pipetting with a P1000 pipette, chilled on ice, washed twice in PBS, and filtered through a 35-um strainer. An aliquot was taken to count cells using a Countess II, and the remainder was crosslinked and processed for ChIP as described above. One litter of embryos was used per experiment, yielding ~1.8-3.6 million cells per region.

Immunoprecipitation-mass spectrometry

hCNCCs were grown in 6x10-cm plates per condition and replicate, optionally treated with 500 nM $dTAG^V$-1 for 30 min. Media was replaced with ice-cold PBS with 0.5 mM PMSF, cells were collected by scraping, and centrifuged at 300g for 5 min at 4°C. After aspirating supernatant, cell pellet was flash frozen and stored at -80°C. The day prior to performing IPs, 30 ug of V5 antibody (Abcam, ab206566, RRID:AB_2819156) and 6 mg magnetic beads (per sample) were conjugated overnight using the Dynabeads Antibody Coupling Kit (Invitrogen, 14311D). The next day, Dignam nuclear extraction was performed (all steps at 4°C or on ice). Briefly, cells were thawed in 5x volume buffer A (10 mM HEPES, 1.5 mM $MgCl_2$, 10 mM KCl, 1x PIC and phosSTOP (Roche, 4906845001) freshly added), rotated for 5 min, centrifuged at 600g for 5 min, and resuspended in 2x buffer A. Cells were lysed by 15 strokes in a Dounce homogenizer with a tight pestle, and then centrifuged at 1000g for 5 min. The pellet was washed in 5x volume buffer A, then resuspended in 2x volume buffer C (20 mM HEPES, 25% v/v glycerol, 420 mM KCl, 1.5 mM $MgCl_2$, 1x PIC and phosSTOP freshly added) and rotated for 30 min. After centrifuging at max speed for 15 min, the supernatant was slowly diluted in an equal volume of buffer D (20 mM HEPES, 25% v/v glycerol, 0.2% v/v Igepal CA-630, 1x PIC and phosSTOP freshly added) and then again diluted two-fold with buffer E (20 mM HEPES, 25% v/v glycerol, 150 mM KCl, 0.1% v/v Igepal CA-630, 1x PIC and phosSTOP freshly added). Precipitate was cleared by centrifugation at max speed for 10 min, and the supernatant (nuclear extract) was quantified by BCA assay and used for IPs. Nuclear extract was added to antibody-coupled beads pre-washed in PBS with 0.1% w/v BSA, rotated for 2h, washed four times with buffer F (20 mM HEPES, 25% v/v glycerol, 150 mM KCl, 1x PIC and phosSTOP freshly added) and two times with PBS.

In a typical mass spectrometry experiment, beads were resuspended in TEAB prior to reduction in 10 mM DTT. Reduced proteins on beads then alkylated using 30 mM acrylamide to cap cysteine residues. Digestion was performed using Trypsin/LysC (Promega) in the presence of 0.02% ProteaseMax (Promega) overnight. Following digestion and quench, eluted peptides were desalted, dried, and reconstituted in 2% aqueous acetonitrile prior to analysis.

Mass spectrometry (MS) experiments were performed using liquid chromatography (LC) using an Acquity M-Class UPLC (Waters), connect to either an Orbitrap Q Exactive HF-X (RRID:SCR_018703 Thermo Scientific) or an Orbitrap Exploris 480 (RRID:SCR_022215 Thermo Scientific). For LC separations, a flow rate of 300 nL/min was used, where mobile phase A was 0.2% (v/v) formic acid in water and mobile phase B was 0.2% (v/v) formic acid in acetonitrile. Analytical columns were prepared in-house by pulling and packing fused silica with an internal diameter of 100 microns. Columns were packed with NanoLCMS Solutions 1.9 um C18 stationary phase to a length of approximately 25 cm. Peptides were directly injected into the analytical column using a gradient (2% to 45% B, followed by a high-B wash) of 90 min. Both MS instruments were operated in a data-dependent fashion using Higher Energy Collison Dissociation (HCD).

Protein purification, crystallization, and data collection

Expression and purification of the DNA-binding domain fragments of human TWIST1 (residues Gln101-Ser170), TCF4 (residues Arg565-Arg624), and ALX4 (residues Asn210-Gln277) were performed as described in refs Savitsky et al.,[120] Morgunova et al.,[121] and Yin et al.[122]. The DNA fragments used in crystallization were obtained as single strand oligos (Eurofins), and annealed in 20 mM HEPES (pH 7.5) containing 300 mM NaCl and 0.5 mM Tris (2-carboxyethyl) phosphine (TCEP) and 10% glycerol. The purified and concentrated proteins were mixed with a solution of annealed DNA duplex at a molar ratio 1:1:1:1.2 at room temperature, and after one hour subjected to the crystallization trials. The crystallization conditions were optimized using several conditions from JCSG crystallization kit (Molecular Dimensions, MD1-37). Complex was crystallized in sitting drops by vapor diffusion technique from solution containing 50 mM sodium cacodylate buffer (pH 7.5), 100 mM magnesium acetate, 18% glycerol, 20% 2-Methyl-2,4-pentanediol and 6-7% PEG (MW 8000). The X-ray data set was collected at European Synchrotron Radiation Facility (ESRF) (Grenoble, France) from a single crystal on beam-line ID23-1 at 100 K using the reservoir solution as cryo-protectant. Prior to data collection, crystals mounted on the goniometer were located and characterized using X-ray mesh scans analyzed by Dozor-

MeshBest.[88,123] The experimental parameters for optimal data collection were designed using the program BEST.[89] Data were integrated with the program XDS[90] and scaled with program AIMLESS as implemented in CCP4.[108] Statistics of data collection are presented in Table S6.

Electrophoretic mobility shift assays (EMSAs)

DNA-binding domain fragments of human TWIST1 and ALX4 were expressed and purified as for crystallization, and TCF3 (residues Arg547-Arg606, E47 isoform) was used instead of TCF4. The forward strand of DNA was ordered with a 5' conjugated Cy3 fluorophore (Integrated DNA Technologies) and annealed with an unlabeled reverse strand in NEBuffer 2 (NEB, B7002S) at 5 uM final concentration, and diluted to 1 uM final concentration in 10 mM Tris-HCl pH 8, 100 mM NaCl, 1 mM EDTA. TWIST1 and TCF3 were pre-mixed at an equimolar ratio and incubated for 30 min at room temperature to form heterodimers. Proteins were diluted in 20 mM HEPES, 300 mM NaCl, 10% glycerol, and 2 mM TCEP. Binding reactions were set up by diluting 0.5 ul LightShift Poly (dI-dC) (Thermo 20148E, 1 ug/ul) in 17 ul total binding buffer (20 mM HEPES, 100 mM NaCl, 10% glycerol, 1 mM DTT, 0.05 mg/ml BSA), adding 1 ul of annealed DNA probe, and finally 1 ul of diluted TWIST1:TCF3 and 1 ul of diluted ALX4 (or equal volume protein dilution buffer). After 30 minutes of incubation at room temperature, 13 ul of each reaction was loaded on a pre-equilibrated 5% native polyacrylamide gel (45 mM Tris-Borate, 1 mM EDTA, 1% glycerol, using 29:1 acrylamide:bis solution) and run for 1 h at 130 V. Gels were imaged using an Amersham ImageQuant 800 with the Cy3 fluorescence setting and a 10 s exposure.

QUANTIFICATION AND STATISTICAL ANALYSIS

ATAC-seq analysis

Reads were trimmed of Nextera adapter sequences and low-quality bases (-Q 10) using skewer v0.2.2[91] and then mapped to the hg38 analysis set (human), mm39 (mouse), or galGal6 (chick) reference genome using Bowtie2 v2.4.1[92] with the options –very-sensitive -X 2000. Reads were deduplicated with samtools v1.10[93] markdup and uniquely mapped reads (-q 20) mapped to the main chromosomes (excluding mitochondria and unplaced contigs) were retained using samtools view. Read ends were shifted inward 5 bp (+5 bp on + strand, -5bp on – strand) for each fragment, and then MACS2[94] was used to call peaks from shifted read ends using–shift -100 –extsize 200 -f BED –nomodel –keep-dup all –call-summits –SPMR with -g hs for human, -g mm for mouse, and -g 1055580959 for chick data. Peaks from all hCNCC experiments were merged into a unified peak set by concatenating all significant summits, clustering peaks within 150 bp with bedtools[95] cluster, keeping only the most significant summit (in any sample) per cluster with a p-value < 1E-20, extending by an additional 100 bp in both directions, and then merging any overlapping peaks with bedtools merge, resulting in 213,151 total peaks. The most significant summit within each merged peak was used as the overall summit, which was used to generate heatmaps and perform motif analyses.

Counts of reads in each sample overlapping the merged peak set were generated using bedtools, and differentially accessible peaks were called using DESeq2[96] using only samples pertinent to each comparison, and using CNCC differentiation replicate as a covariate, excluding peaks with fewer than an average of 10 reads per dataset in the comparison. Genome browser tracks were generated by MACS2 v2.2.7.1[94] and plotted using IGV v2.7.2.[97] Peaks with a summit within 500 bp of a TSS (from refGene GFF files from UCSC for hg38 and mm39, and ncbiRefSeq for galGal6) were considered promoter-proximal, and the remaining peaks were considered distal.

For published data with multiple replicates, all summit files were concatenated and then summits within 100 bp were clustered with bedtools cluster, and the most significant summit in each cluster was retained.

For ENCODE data, bed narrowPeak files and metadata were downloaded on 1-18-2023 for all GRCh38 and mm10 non-control ATAC-seq (n=549) and DNase-seq (n=1781) experiments. All replicates were processed separately. Samples were annotated into tissue/cell types as follows: facial, limb, or lung if the annotation included that corresponding term; fibroblast if it included "fibroblast" or "HFF-Myc", "BJ", "AG09319", "AG09309", "AG10803", "GM03348", "GM04504", or"NIH3T3"; muscle if it included "muscle" or "gastroc"; neuroblastoma if it included "SK-N" or "BE2C"; and brain if it included "brain", "cereb", "front", "nucleus", "hippo", "occipital", "gyrus", or "ceph". Samples were annotated as pluripotent stem cells if the annotation included "iPS", "WTC11", "ES-", "R1", "H1", "H7", "H9", "ZHBTc4", "WW6", "L1-S8R", "NT2/D1", or "GM23338" but not "NCI-H929" or "CH12.LX".

ChIP-seq and CUT&RUN analysis

Reads were trimmed, mapped, and deduplicated as described above for ATAC-seq analysis (but trimming Truseq adapter sequences), and then peaks were called with MACS2 (but with -f BAMPE –nomodel –keep-dup all –call-summits –SPMR) and browser tracks were generated with deeptools v3.5.0[98] bamCoverage -bs 10 –normalizeUsing RPGC –samFlagInclude 64 –samFlagExclude 8 –extendReads and plotted using IGV. For TWIST1 acute depletion samples, which included O9-1 mouse cranial neural crest cell spike-in chromatin, reads were mapped to a combined hg38 analysis set + mm39 reference genome. The fraction of reads mapping to the mouse genome was similar across all samples, so unnormalized tracks are shown for consistency.

For published single-end read data, reads were not deduplicated, and peaks were called with MACS2 with -f BAM and without –nomodel).

For defining TWIST1/AP-2α-bound distal regions used as reference points for heatmap generation, merged ATAC peaks were defined as bound by TWIST1 or AP-2α if the ATAC summit was within 200 bp of the ChIP summit, where the ChIP summits from multiple replicates were merged using bedtools cluster if they were within 150 bp. ATAC peaks were considered distal if they were at least 1000 bp from a TSS.

For comparisons of quantitative TWIST1 binding strength in hCNCC and HEK293 with and without ALX4, TWIST1 ChIP peaks ($p < 10^{-10}$ for hCNCC, $p < 10^{-5}$ for HEK293) from both conditions (+/- ALX4) from the same cell type were merged by removing peaks with a stronger peak within 100 bp, with bedtools cluster.

Putative enhancers (promoter-distal ATAC peaks with robust H3K27ac signal) were defined as ATAC peaks with a maximum of at least 10 RPGC in at least one TWIST1^{FV} or WT H3K27ac ChIP. For assessing $\log_2$ fold changes in H3K27ac signal, reads were counted over merged ATAC peaks using deeptools multiBamSummary -e –outRawCounts and used as counts for DESeq2.

CUT&RUN reads were mapped to a combined human (hg38 analysis set) and *E. coli* (K-12 substr. MG1655) reference genome using Bowtie2. CUT&RUN tracks of depleted (i.e. dTAG^{V}-1 treated) samples were normalized to the control samples using the *E. coli* spike-in control, by multiplying by a scaling factor of $(E_{control}/H_{control})/(E_{depleted}/H_{depleted})$, where E_x = fraction of reads mapped to E. coli in sample x, and H_x = fraction of reads mapped to human.

SLAM-seq and RNA-seq analysis

Newly generated sequencing data (read 1 only) were trimmed of adapters and low-quality bases then poly A strings using skewer[91] and processed using slamdunk v0.4.3[119] with map options -n 100 -5 0 -q -ss, using the hg38 analysis set reference genome. Differentially expressed genes were called using DESeq2[96] using only samples pertinent to each comparison, and using CNCC differentiation replicate as a covariate, excluding genes with fewer than 30 reads across datasets in the comparison.

Publicly available RNA-seq data were trimmed of adapters and low-quality bases using skewer[91] and mapped using salmon[124] quant –seqBias -l A to hg38_cdna and mm10_cdna pre-built indices (http://refgenomes.databio.org/). Salmon abundance files were summarized to the gene level and imported into R with the tximport[99] package v1.20.0 with countsFromAbundance = 'lengthScaledTPM'. When multiple replicates were available, the mean TPM of all replicates was used.

Human-mouse orthologs were downloaded from https://www.informatics.jax.org/downloads/reports/index.html#homology and only one-to-one orthologs were kept for analyses of RNA levels across cell types. The list of human TFs and their family definitions were downloaded from http://humantfs.ccbr.utoronto.ca/download.php (Full Database).

CCLE processed TPM values were downloaded, and these values for TWIST1 were plotted against the average for all homeodomain TFs with known motifs aligned to the HD portion of Coordinator.

Motif analysis

Motifs from JASPAR 2018,[125] HOCOMOCO v11 human and mouse core binding models,[126] and HT-SELEX,[8] plus the Coordinator motif[19] were used for scans of known motifs with meme suite v5.1.1 AME.[102] Motifs clusters from https://www.vierstra.org/resources/motif_clustering[127] were used, with one manually added cluster for the Coordinator motif, into which the TWIST1 motifs from HOCOMOCO were moved.

Motif alignments to Coordinator were performed with meme suite v5.1.1 TOMTOM[101] using a cutoff of q-value < 0.4. Motifs from the same TF (counting orthologous human and mouse TFs as the same) and in the same cluster were collapsed, keeping the one with the best alignment.

Motif matches in the genome were calculated using meme suite v5.1.1 FIMO[103] (for analyses of Coordinator, double E-box, and single E-box motifs in hg38 and mm39) using options –max-stored-scores 5000000 and PWMScan[104] (for annotating other motifs on hg38) using a p-value threshold of 0.001 and a background frequency of 0.25 for all bases. A p-value threshold of 10^{-4} was used to define motif presence for Coordinator, double E-box, single E-box, NEUROD1 (NDF1_HUMAN.H11MO.0.A) motifs, while a threshold of 10^{-3} was used for the HD dimer (ALX1_HUMAN.H11MO.0.B) and HD monomer motif (PRRX2_HUMAN.H11MO.0.C). For the HD monomer motif, instances overlapping Coordinator or HD dimer motifs were excluded.

ATAC-seq and ChIP-seq peaks were ranked by summit p-values as reported by MACS2 and summits ± 100 bp were used for AME and analyses of TF depletion-responsive ATAC peaks.

The double E-box motif was generated by using STREME[105] *de novo* motif discovery to compare TWIST1 ChIP peaks (summits ± 100 bp) with significantly stronger vs weaker binding in *ALX1*^{FV} *ALX4*$^{-}$ cells compared to WT hCNCCs.

For comparisons of quantitative TWIST1 binding strength in hCNCC and HEK293 with and without ALX4, merged TWIST1 summits were classified as Coordinator-containing if they had a Coordinator motif with $p < 10^{-4}$ within 100 bp of the summit and the strongest Coordinator motif had a more significant p-value than the strongest double E-box motif; as double E-box-containing if they had a double E-box motif with $p < 10^{-4}$ within 100 bp of the summit and the strongest double E-box motif had a more significant p-value than the strongest Coordinator motif; or otherwise as neither.

Motif logo plots were generated with meme suite v4.12.0 ceqlogo.

IP-MS analysis

For data analysis, the.RAW data files were checked using Preview (Protein Metrics) to verify calibration and quality metrics. Data were processed using Byonic (Protein Metrics) to identify peptides and infer proteins. Proteins were held to a false discovery rate of 1%,

using standard approaches described previously[128]. Known contaminants and any proteins with peptides detected in a control IP with the same V5 antibody on untagged hCNCC protein extracts were excluded.

Structure determination and refinement

The structure was solved by molecular replacement using program Phaser[106] as implemented in Phenix[107] and CCP4[108] with the structure of TCF4 (PDB: 6OD3) as a search model for TCF4 and TWIST1, and NMR structure of ALX4 (PDB: 2M0C) as a search model for ALX4. After the positioning of proteins, the density of DNA was clear and the molecule was built manually using Coot.[110] However, we did not find any density for the BRG1 fragment. The rigid body refinement with REFMAC5 was followed by restrain refinement with REFMAC5,[109] as implemented in CCP4. Resulting statistics of the refinement are presented in Table S6. Structural alignments and figures were generated with PyMOL. The resulting structure was submitted to Protein Data Bank with ID 8OSB.

Human-chimpanzee enhancer divergence analysis

We scanned the set of human and chimp genomic sequences corresponding to 106,331 orthologous regulatory regions using meme suite v5.1.1 FIMO, with either the original Coordinator PWM or altered PWMs with duplicated or removed weak A positions in the linker region. Since altered linker length PWM matches can in some cases still match to the original Coordinator sequence, to avoid confounding with original Coordinator sequence, altered linker matches that directly overlap known Coordinator motif were removed from further analysis. Next, we performed outer join of the scan results, filling missing data with values of the scan p-value threshold. Changes in motif strength (between human and chimp) were calculated as the log p-value ratio and compared with changes with $\log_2$ fold changes of the H3K27ac signal (from ref Prescott et al.[19]) using Pearson correlation. Similar results were obtained using PWM with linkers of variable lengths with no base preference at all.

EMSA quantification

Images were quantified using Fiji "measure" tool and the fraction of bound DNA was calculated by dividing the background-subtracted signal of the bound DNA band by the sum of bound and unbound signal. Data were fit to Hill equations using nls in R.

LocusZoom plots

LocusZoom plots were constructed from summary statistics of the facial shape GWAS by White et al. (available from GWAS Catalog: GCST90007181– GCST90007306). Since SNP-phenotype associations were tested across 63 facial modules and meta-analyzed using two independent cohorts, the set of p-values used for plotting was determined for each lead SNP separately based on the module-cohort combination where it yielded the lowest p-value. Linkage disequilibrium (LD) with the lead SNP was calculated with PLINK 1.9[129] based on the EUR samples from the 1000 Genomes Project Phase 3 v5 dataset (available at: http://ftp.1000genomes.ebi.ac.uk/vol1/ftp/release/20130502/) and protein coding genes including their exons were annotated using NCBI RefSeq annotations (available at: http://hgdownload.soe.ucsc.edu/goldenPath/hg19/bigZips/genes/hg19.ncbiRefSeq.gtf.gz).

Facial Morphs

Following White et al.,[57] the lead SNPs at loci encoding each of the Coordinator-binding TFs (*PRRX1*, *MSX1*, *TWIST1*, *ALX1*, and *ALX4*) were tested for association with facial shape in a European cohort from the US comprising 4,680 individuals. Specifically, for each facial module and each SNP, canonical correlation (CCA) analysis was performed on the pre-residualized principal components (PCs) that describe the facial variation within that module. CCA yielded multivariate effect size estimates for the PCs, which can be interpreted as the axis of shape variation maximally correlated with the SNP under investigation. While a SNP was tested across all 63 facial modules, only the effect in the most significant facial module was visualized. To do so, the average face, M, was first deformed to the positive shape as $M + 3\Sigma$ and to the negative shape as $M - 3\Sigma$, with Σ being the difference in 3D shape for one standard deviation along the shape axis. Normal distances were then calculated for each vertex on the negative shape to their corresponding vertex on the positive shape. The normal distances were then visualized with a heatmap on an average face whereby blue represents an inward depression and red represents an outward protrusion.

Brain Morphs

Similar to the facial segmentation by White et al.,[57] Naqvi et al.[58] segmented the cortical surface into 285 hierarchical modules. For each lead SNP at a locus encoding one of the Coordinator-binding TFs (*TWIST1*, *ALX1*, and *ALX4*), p-values corresponding to the modules of hierarchical level 5 were visualized on an average brain after normalizing the $-\log_{10}$(p-values) with respect to the maximum value at each locus.

S-LDSC analysis

GWAS summary statistics for facial shape (full face, segment 1) and brain shape (full brain, segment 1) were obtained from Figshare (https://doi.org/10.6084/m9.figshare.c.5089841.v1).[58] Height GWAS summary statistics were downloaded from the Price laboratory website (https://console.cloud.google.com/storage/browser/broad-alkesgroup-public-requster-pays). LD scores were created for each annotation (corresponding to a set of differential or control distal ATAC-seq peaks) using the 1000G Phase 3 population reference. Each annotation's heritability enrichment for a given trait was computed by adding the annotation to the baselineLD model and

regressing against trait chi-squared statistics using HapMap3 SNPs with the stratified LD score regression package v.1.0.1.[113] We note that the TWIST1-dependent peak sets span 0.67% and 0.73% of SNPs for acute depletion and long-term loss, respectively (based on 1000 Genomes SNP annotation in individuals of European ancestry, which encompass our GWAS populations), above the 0.5% defined as a large annotation.[130] Accessibility-matched distal peaks were selected from peaks with a $\log_2$ fold change between -0.5 and 0.5 and adjusted p-value > 0.1 using the Matching package for R v4.10-8 with distance.tolerance = 0.01 and ties = F.[114]

CellPress
OPEN ACCESS

Supplemental figures

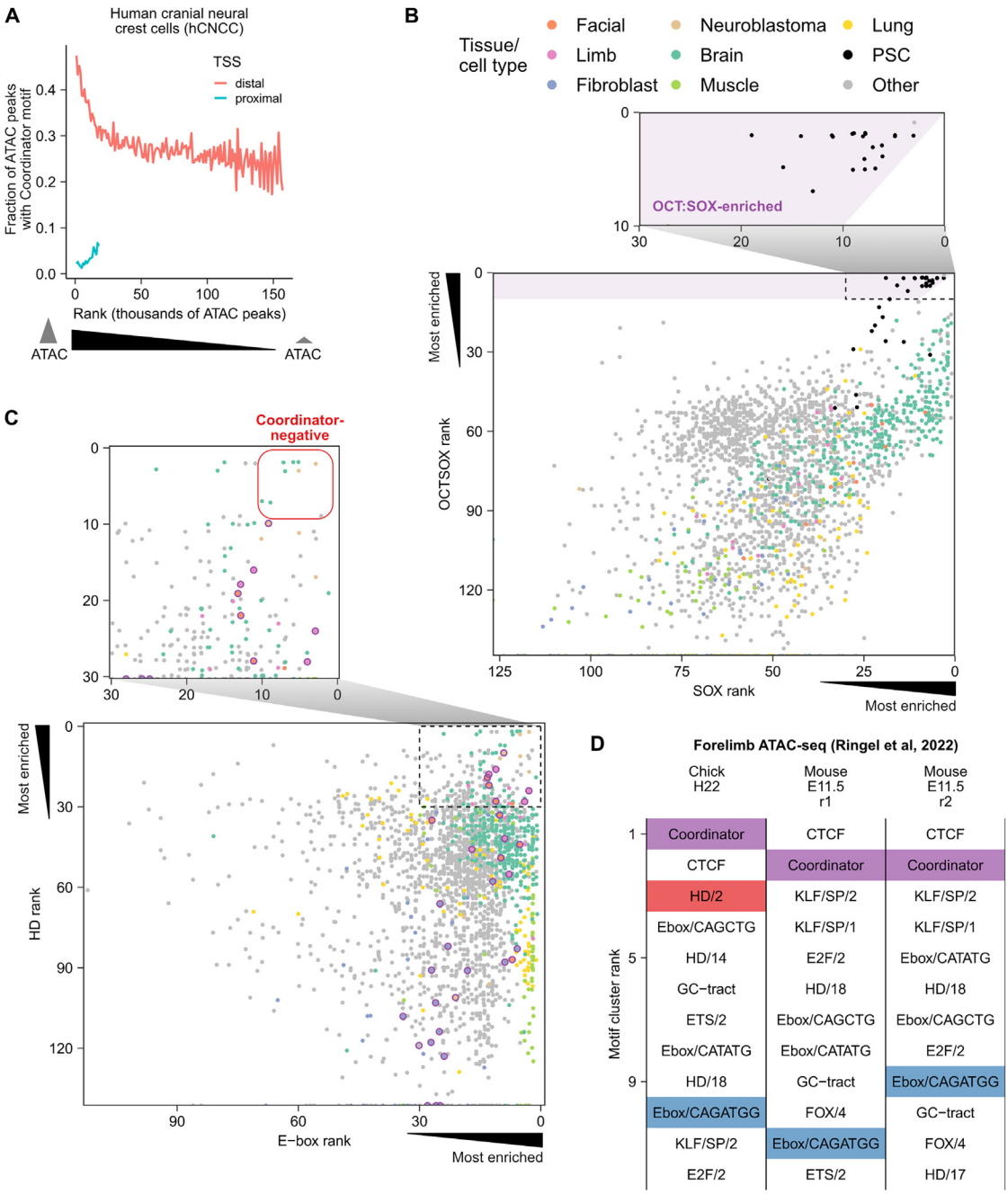

Figure S1. Coordinator and OCT:SOX motif enrichment in open chromatin regions, related to Figure 1

(A) Coordinator motif frequency in ranked ATAC peaks ordered left to right from the strongest to weakest, split by whether they overlap a TSS, and grouped into bins of 1,000 peaks.

(B) Rankings of OCT:SOX and its constituent SOX/1 motif in enrichment in the top 10,000 distal accessible regions for all DNase-seq and ATAC-seq datasets on ENCODE. Points are jittered to avoid overplotting. Zoomed-in portion highlights the pluripotent stem cell samples among those with OCT:SOX motif enrichment.

(legend continued on next page)

(C) Rankings of the E-box/CAGATGG and HD/2 motif clusters in enrichment in the top 10,000 distal accessible regions for all DNase-seq and ATAC-seq datasets on ENCODE. Points are jittered to avoid overplotting. Purple circles indicate samples with Coordinator motif enrichment (Coordinator rank < 10 and Coordinator rank < E-box and HD ranks). Zoomed-in portion highlights samples lacking Coordinator enrichment despite enrichment of both E-box and HD motifs.
(D) Top motif clusters enriched in distal ATAC-seq peaks of chick and mouse forelimbs.[60] Coordinator is highlighted in purple, the best E-box motif match to Coordinator (E-box/CAGATGG) is in blue, and the best homeodomain motif match to Coordinator (HD/2) is in red.

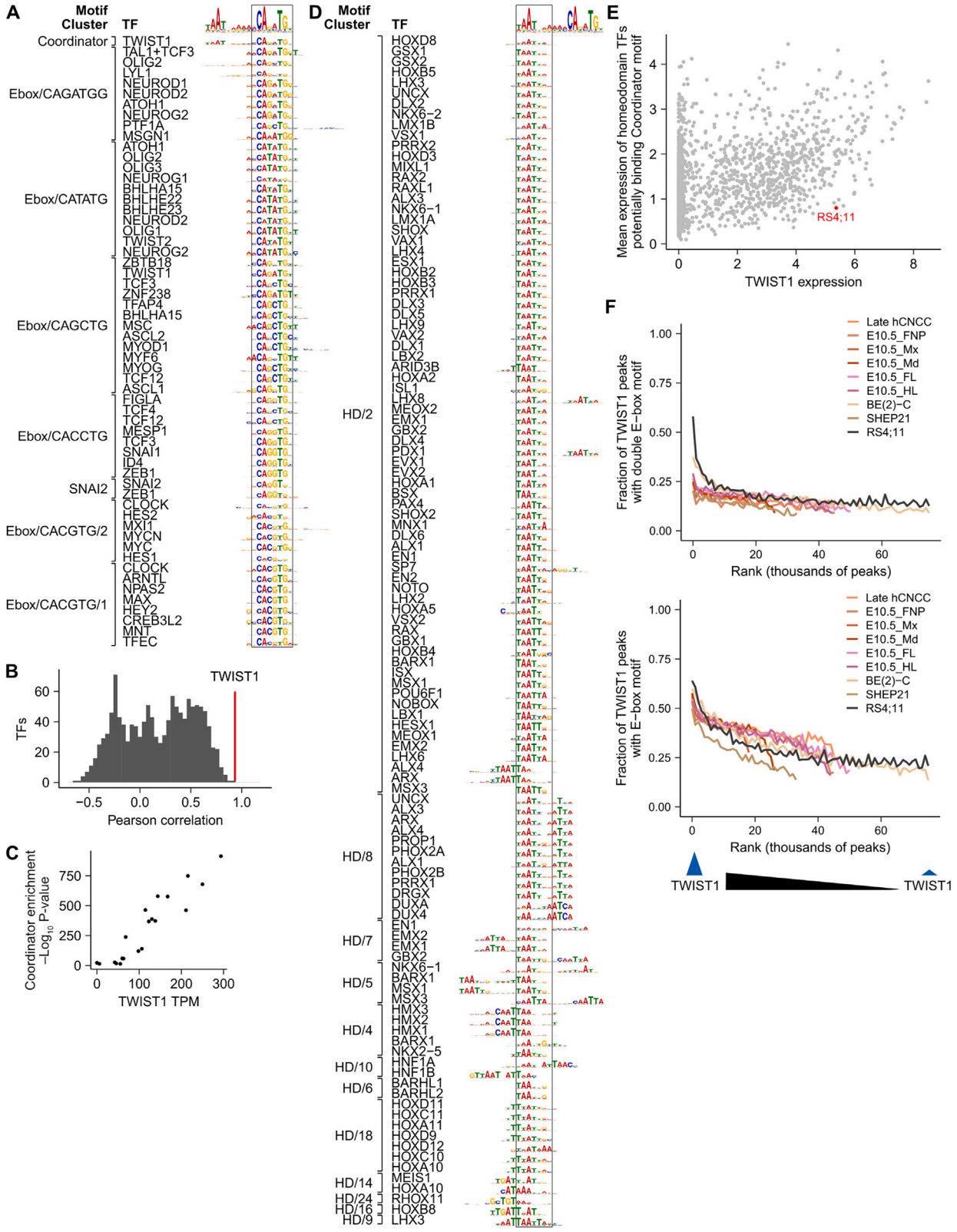

(legend on next page)

Figure S2. Candidate Coordinator-binding factors and a cell line without Coordinator activity, related to Figure 2

(A) All bHLH and SNAI TFs with known motifs aligned to the E-box portion of Coordinator (highlighted by bounding box).

(B) TWIST1 is the TF with the highest correlation between TF RNA levels and Coordinator enrichment.

(C) TWIST1 RNA level is correlated with Coordinator motif enrichment p value (same samples as in Figures 1D and 1E).

(D) All HD TFs with known motifs aligned to the HD portion of Coordinator (highlighted by bounding box).

(E) Scatterplot of TWIST1 vs. average of all candidate Coordinator-binding HD TF expression in all CCLE cell lines. Both axes show $\log_2$(TPM + 1) values. RS4;11 cells are highlighted in red.

(F) Frequencies of double E-box and single E-box motifs in ranked TWIST1 ChIP-seq peaks in bins of 1,000 peaks (as in Figure 2B).

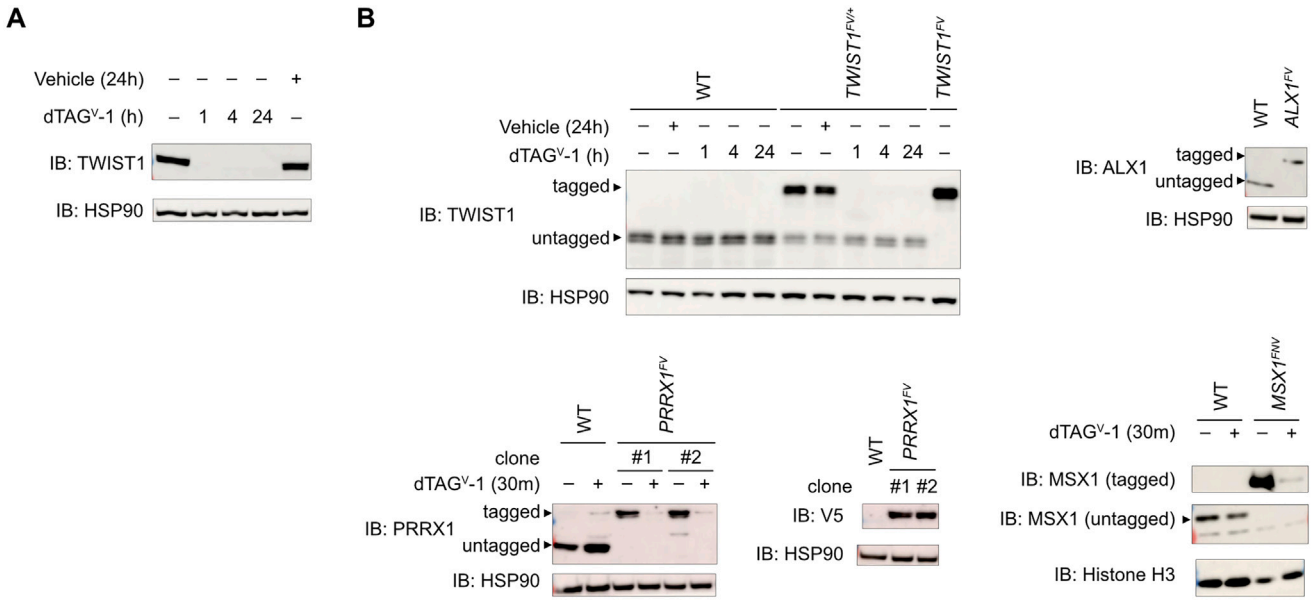

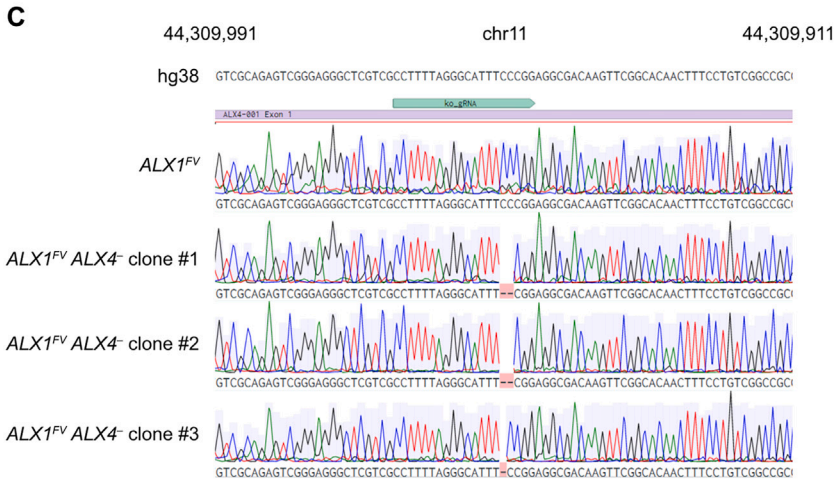

Figure S3. Validation of degron-tagging and ALX4 knockout, related to Figure 3

(A) Western blot of TWIST1 depletion time course in *TWIST1*^{FV} hCNCCs, with HSP90 as a loading control. IB, immunoblot.

(B) Western blot comparisons of tagged and untagged TF protein levels using endogenous antibodies, with HSP90 or histone H3 as loading controls.

(C) Sanger sequencing genotyping of *ALX1*^{FV} *ALX4*$^{-}$ lines. The guide RNA used to generate the edits is shown above traces in teal.

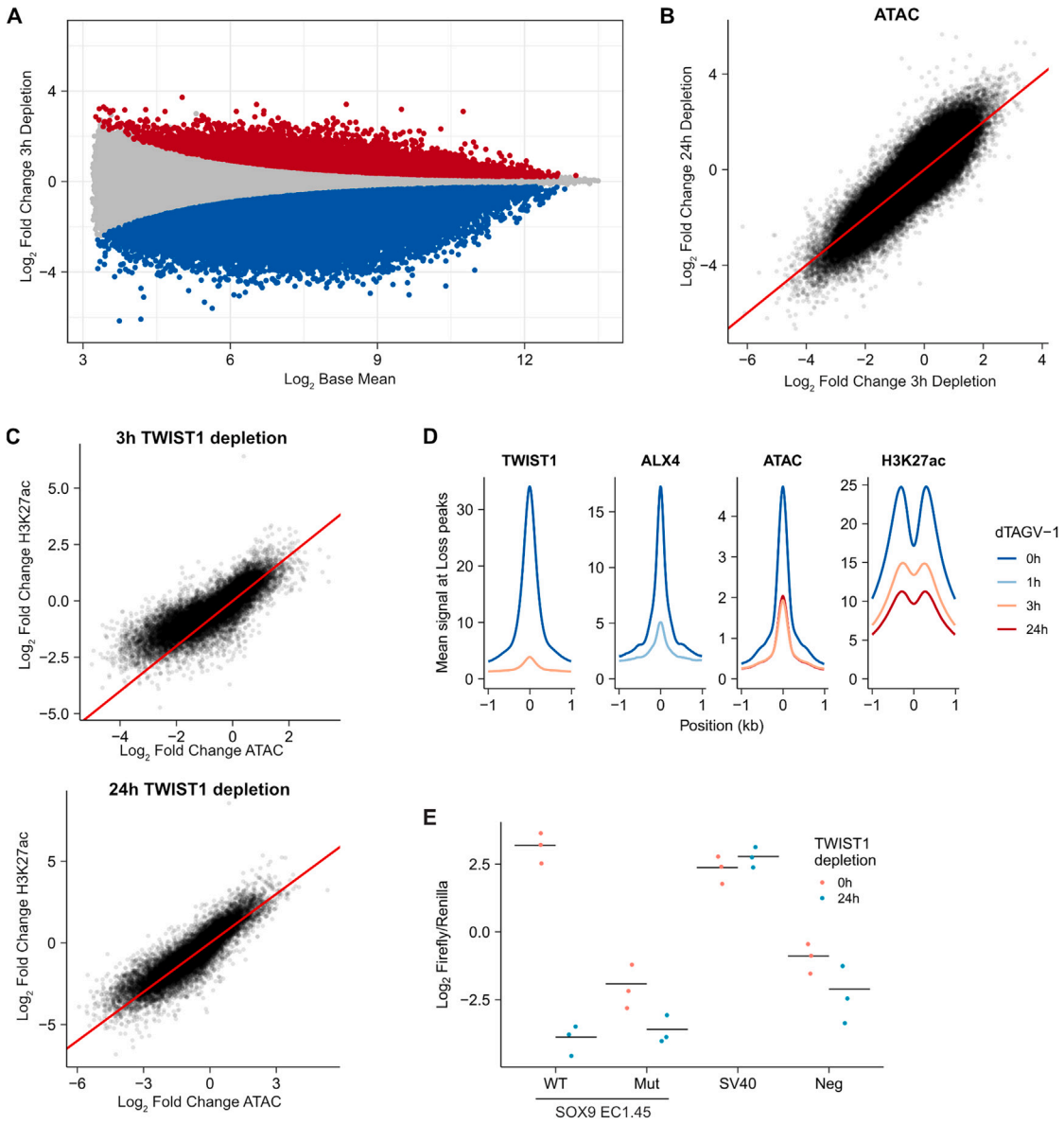

Figure S4. Effects of TWIST1 depletion on accessibility, H3K27ac, and enhancer activity, related to Figure 4

(A) MA plot of TWIST1 3 h depletion. Significant (adjusted p value < 0.05) upregulated and downregulated peaks are colored in red and blue, respectively.

(B) Scatterplot of 3 vs. 24 h ATAC fold changes. Red line indicates y = x.

(C) Scatterplots of ATAC vs. H3K27ac fold changes upon 3 and 24 h of TWIST1 depletion. Red line indicates y = x.

(D) Mean signal plots of TF binding, ATAC, and H3K27ac across TWIST1 depletion (dTAG^{V}-1) time points (0–24 h) at enhancers with the loss of accessibility upon TWIST1 depletion.

(E) Luciferase enhancer reporter activity with and without TWIST1 depletion. SOX9 EC1.45 indicates the "min1-min2" enhancer from Long et al.,[23] Mut indicates a mutant version of the enhancer with substitutions at all high information content positions within the E-box portions of all four Coordinator motifs, SV40 is the SV40 enhancer, and Neg indicates a control plasmid lacking an enhancer insert. Points are biological replicates transfected independently (n = 3).

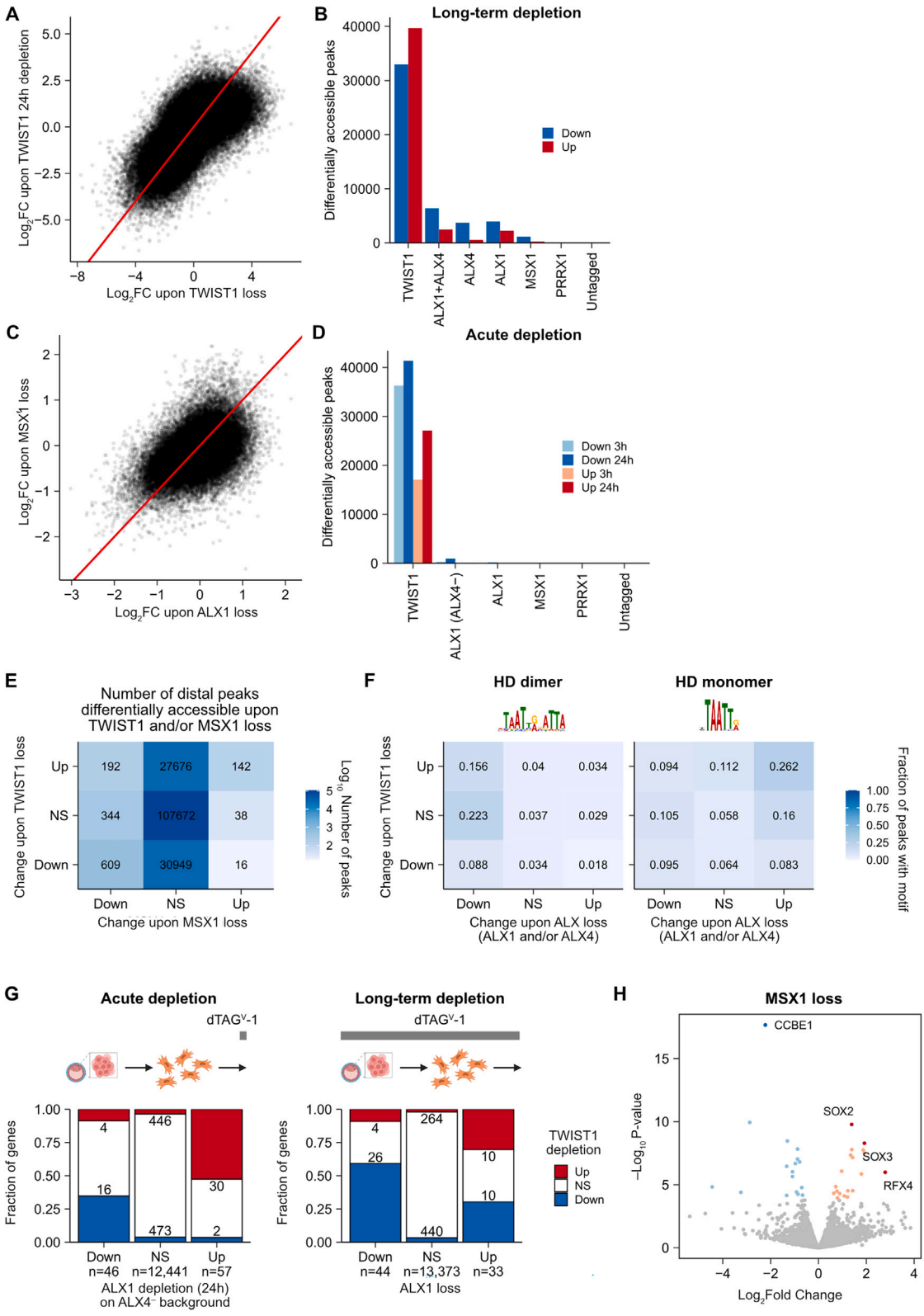

(legend on next page)

Figure S5. Acute and long-term depletions of Coordinator-binding TFs, related to Figure 5

(A) Scatterplot of TWIST1 acute 24 h vs. long-term depletion effects on accessibility at distal open chromatin. Red line indicates y = x.
(B) Bar plot of the number of significant changes (FDR < 0.05) in ATAC-seq upon long-term depletions.
(C) Scatterplot of ALX1 vs. MSX1 long-term depletion effects on accessibility at distal open chromatin. Red line indicates y = x.
(D) Bar plot of the number of significant changes (FDR < 0.05) in ATAC-seq upon acute depletions.
(E) Table of the number of distal regions changing in accessibility upon MSX1 and/or TWIST1 long-term depletion. NS, not significant.
(F) Frequencies of HD motifs in regions responsive to ALX and/or TWIST1 long-term depletions. NS, not significant.
(G) Bar plots of the fraction of genes responsive to ALX1 depletion that are also responsive to TWIST1 depletion, for acute depletion (in ALX4− background) and long-term depletion (in ALX4+ background). NS, not significant.
(H) Volcano plot of MSX1 RNA-seq data. Significantly (FDR < 0.05) upregulated genes are highlighted in red/orange and downregulated genes are in blue. Selected genes are labeled and highlighted in darker colors.

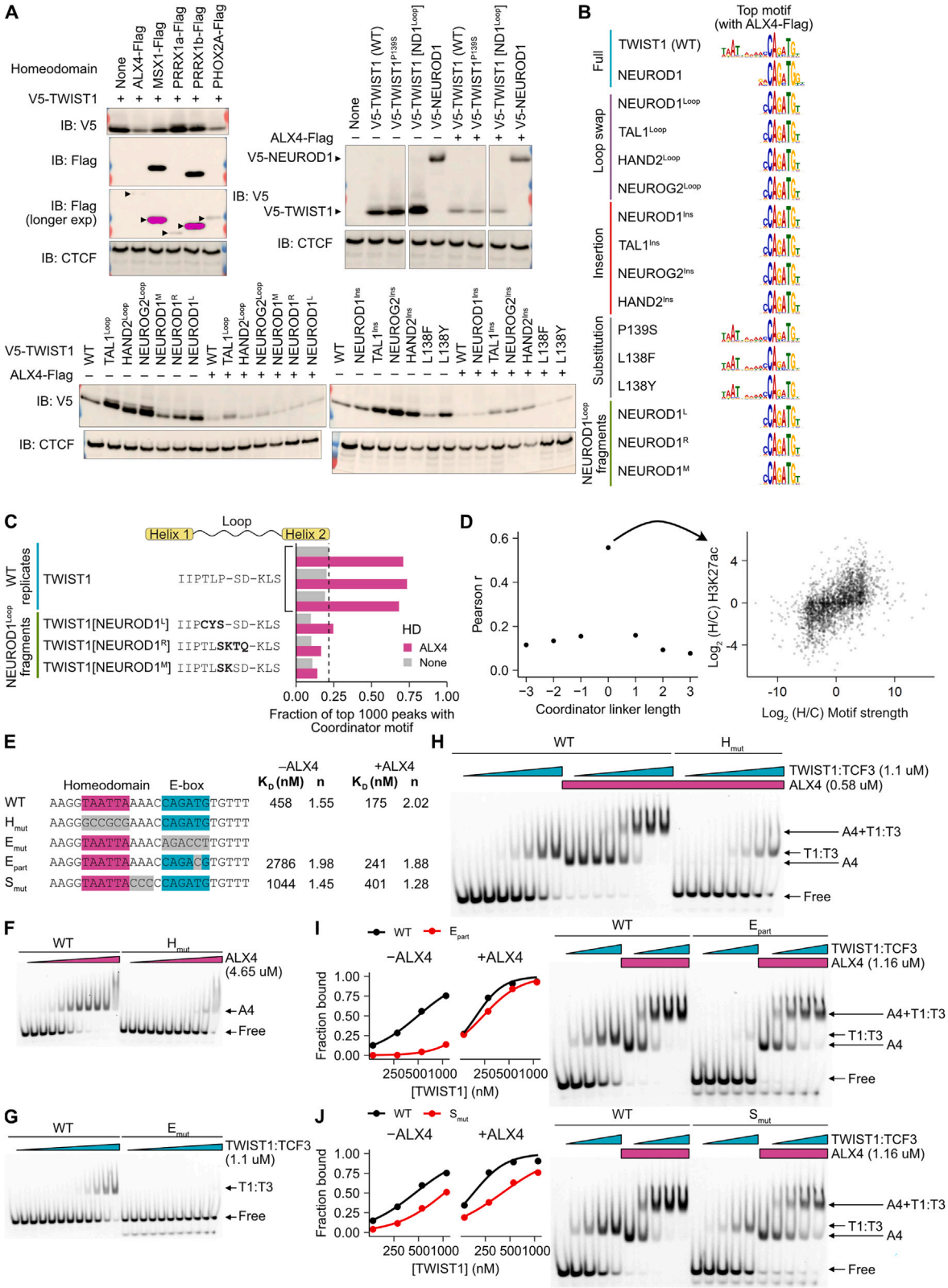

(legend on next page)

Figure S6. DNA guiding of TWIST1-HD interactions and variation among bHLH and HD TFs, related to Figure 6

(A) Western blots of HEK293 cells transfected with plasmids encoding V5-TWIST1 or loop-swap mutants (sequences in Figures 6F or S6C) and various homeodomain TFs, with CTCF as a loading control. IB, immunoblot. Saturated pixels are colored magenta. Cropped images are from the same enhanced chemiluminescence (ECL) reaction and exposure.

(B) Most enriched known motif in the top 1,000 ChIP-seq peaks for each of the six transfections shown in Figures 6F and S6C.

(C) Extent of Coordinator-motif-binding preference of V5-tagged TWIST1 and various loop mutants derived from NEUROD1 expressed in HEK293 cells (see Figure S6A for protein levels) with (magenta) or without ALX4 (gray).

(D) Left, Pearson correlation between the strength of wild-type Coordinator motif or variants with modified spacer lengths and the human-chimp divergence in H3K27ac. Right, example of data used for correlation calculation for the wild-type Coordinator motif.

(E) Electrophoretic mobility shift assay (EMSA) probe sequences (upper left) and estimated K_D and Hill coefficients (n) for (F)–(J).

(F–J) EMSA gels and Hill curve fits (for I and J) for WT vs. homeodomain motif mutant sequence (F), WT vs. E-box motif mutant sequence (G), WT with vs. without ALX4 and WT vs. homeodomain motif mutant sequence (H), WT vs. partial E-box sequence (I), and WT vs. spacer mutant (J).

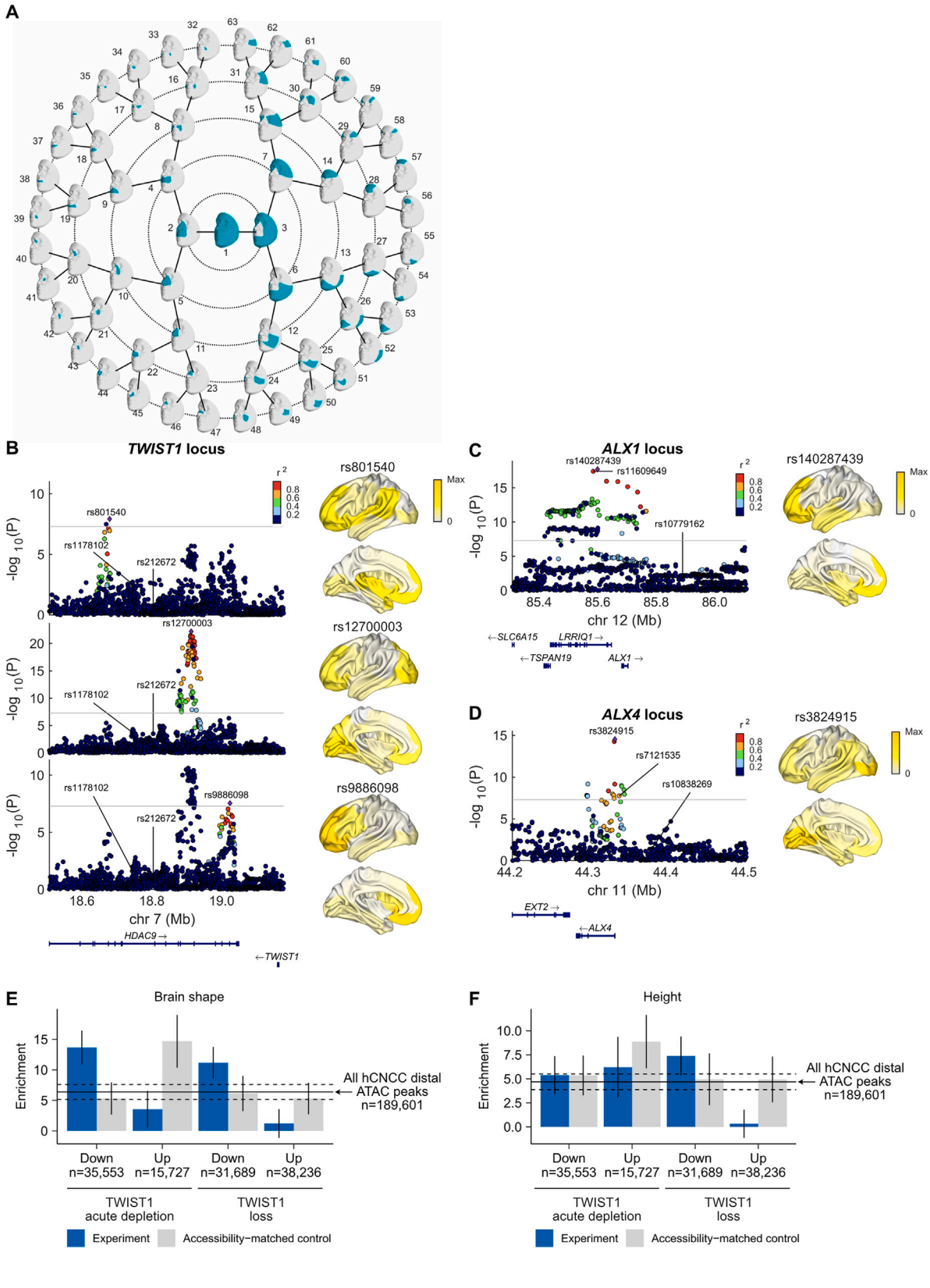

(legend on next page)

Figure S7. Face, brain shape, and height heritability in Coordinator-binding TF loci and genomic targets, related to Figure 7

(A) The 63 hierarchical facial segments used to define facial shape phenotypes associated with each SNP.

(B–D) LocusZoom plots (left) show SNPs in each locus (B, *TWIST1*; C, *ALX1*; and D, *ALX4*) plotted by the p value of association with brain shape and colored by linkage disequilibrium (r^2) to the lead SNP from each peak (purple diamond). The horizontal line indicates genome-wide significance threshold. Morphs (right) show the regions in the brain with the highest significance of association with each lead SNP, with the top image of each pair showing an external view of the left hemisphere and the bottom image showing an internal view.

(E and F) Fold enrichment of SNPs associated with brain shape (E) or height (F) in distal ATAC peaks differentially accessible upon TF depletion or loss, with accessibility-matched control sets. The horizontal line indicates the enrichment in all hCNCC distal ATAC peaks, with flanking dashed lines indicating error bars. Error bars represent SEM.